UNIVERSITATEA VALAHIA DIN TÂRGOVIȘTE
1992

DE GRUYTER OPEN

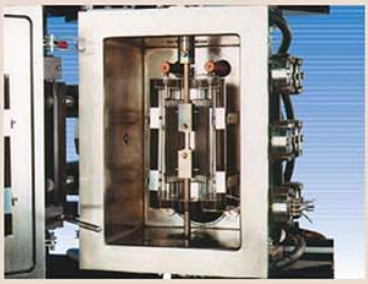

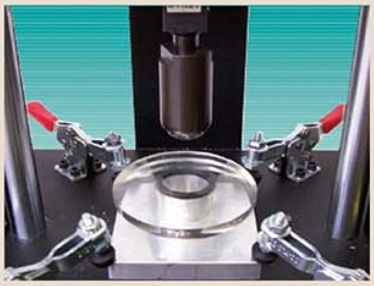

The Scientific Bulletin of Valahia University MATERIALS and MECHANICS

2018

Vol. 16 No. 14

DE GRUYTER OPEN

The Scientific Bulletin of VALAHIA University
MATERIALS and MECHANICS –Vol. 16, No. 14

DOI 10.1515/bsmm-2018-0001

DENSIFICATION MECHANISM, ELASTIC-PLASTIC DEFORMATIONS AND STRESS-STRAIN RELATIONS OF COMPACTED METAL-CERAMIC POWDER MIXTURES (REVIEW)

Ileana Nicoleta POPESCU [1], Ruxandra VIDU [2,*]

[1]Valahia University of Targoviste, Faculty of Materials Engineering and Mechanics, Str. Aleea Sinaia, No. 13, Targoviste, Romania
[2]California Solar Energy Collaborative, University of California, Davis, 1, Shields Ave, Davis, USA

E-mail: pinicoleta24@yahoo.com, *rvidu@ucdavis.edu

Abstract: *The basic purpose of compaction is to obtain a green compact with sufficient strength to withstand further handling operations. The strength of green compact is influenced by the characteristics of the powders (apparent density, particle size and shape, internal pores etc.), the processing parameters (applied force, pressing type, and temperature) and testing conditions (strain rate etc.) Successful powder cold compaction is determined by the densification and structural transformations of powders (metallic powders, ceramic powders and metal-ceramic powder mixtures) during the compaction stages. In this paper, for understanding the factors that determine a required strength of compacted metal-ceramic powder mixtures, we present the densification mechanisms of different mixtures according to densification theories of compaction, the elastic-plastic deformations of mixture powders, the stress-strain relations and the relaxation behavior of compacted metal-ceramic composite parts and the particularities of each of them.*

Keywords: *Densification mechanism, Compressibility, Elastic-Plastic deformations, Metal-ceramic powders, Composites.*

1. INTRODUCTION

The compressing of powder mixtures to obtain metal-ceramic composite parts can be done in different ways (with isostatic press, by rolling, extrusion) but compaction in dies using conventional hydraulic presses is the easiest method to obtain a green compact. The strength of green compact is influenced by the characteristics of the powders (the chemical composition, particle microstructure, form, size and distribution of the average particle size, apparent density, true density, specific surface, porosity, compressibility and fluidity), the processing parameters (applied force, pressing type, and temperature) and testing conditions (strain rate etc.) [1-8].

For understanding the factors that determine a required strength, is necessary to investigate the densification mechanisms of mixture powders.

2. DENSIFICATION MECHANISM. ELASTIC - PLASTIC DEFORMATIONS OF POWDERS

According to the densification theories of the compaction powders proposed by Gethin [9], Sheppard [10], McShane, Fischmeister & Artz [11], generally accepted, structural transformations at compaction operations are carried out in the following three stages, presented schematically in Figure 1a and b .

Stage I: Reorientation/ rearrangement and packing particulate powders;

Stage II: The increase of the contact surface areas between the particles by elastic-plastic deformation of the metallic particles and the fragmentation of the brittle ceramic particles,

Stage III: Massive plastic deformation, porosity reduction (less than 5% e.g. at 1 GPa) [12-20].

In the first stage of compaction, it takes place the decreasing the distance between the powder particles at the maximum level (form a closely packed mass) and the larger voids fill by reorienting, sliding, and interpenetrating the particles at very low pressures, according to Jones theory at around 0.05 -1 MPa [15]. The particles retain most of their original properties, although energy is dissipated due to inter-particle and particle to wall friction.

The second stage occurs at an intermediate pressure when the powder mass decreases continuously its volume.

Due to the plastic deformation of the metal particles and the fragmentation of the hard/brittle - ceramic particles, the increase of the contact surfaces between the particles results. The number of contacts increases as particle rearrangement and sliding occur. Cold welding and/or mechanical interlocking of the particles contribute towards the green strength of the compact. For brittle particles, the onset of plastic deformation can lead to fracture, giving way to fragmentation of the original particles and causing densification by repacking of the fragments. With increasing compaction pressure, the green density increases. In this case, the metal powder particles harden by cold plastic deformation (work hardening) and thus require much higher compaction pressures (Fig. 1b). The factors that influence the degree of densification are presented in Fg 1c. As is known, for better densification of materials during compaction, it is adding lubricants to improve powder densification; this process is possible by rearranging the particles due to the decrease in the frictional forces between the particles themselves, respectively the particles and the compacting tools. More lubricant is beneficial at lower compacting pressures, but there is a transition point at which the additional lubricant impedes further densification [4].

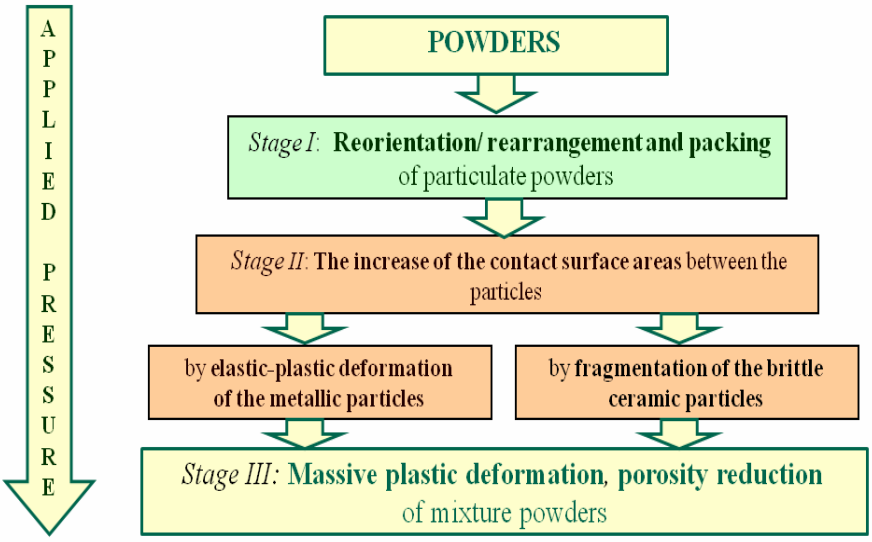

a)

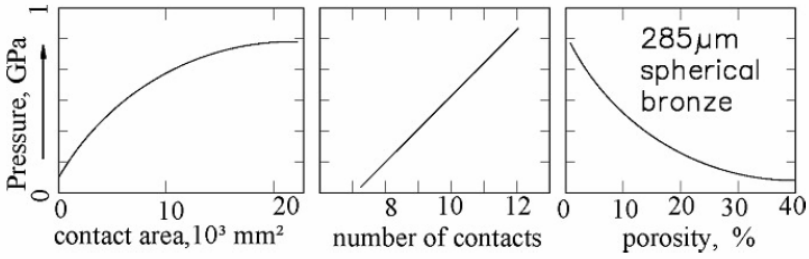

b)

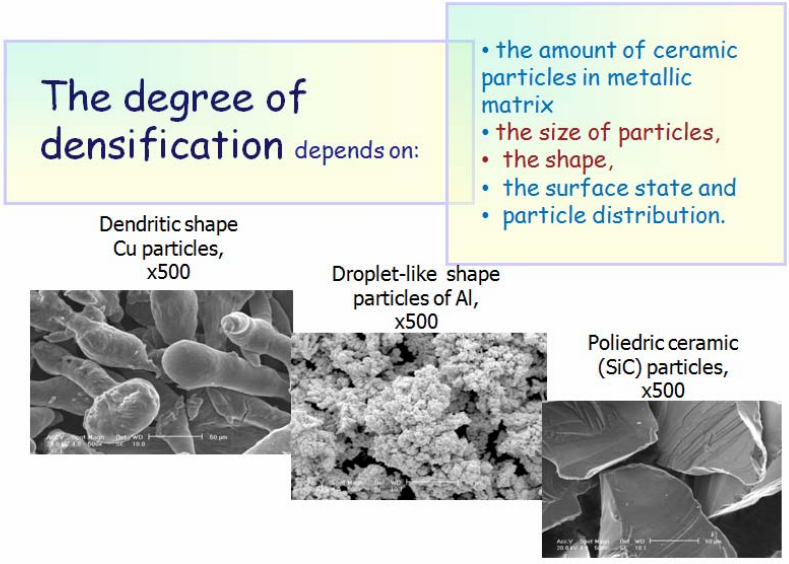

c)

Figure 1. Schematically presentations of densification mechanism: a) Structural transformations in three stages, during compaction operations according with Gethin & Arin [9], Sheppard and McShane [10] , Fischmeister & Artz [[11]; b) Variation of contact area, number of contacts and porosity of spherical bronze particles with applied pressure [21]; c) Factors that influence the degree of densifications, adapted after [12-13]

Quantitatively, the contact surface area S is directly proportional to the applied pressure P to the mass of powders and also depends to the critical stress of plastic deformation or yield strength σ_c of the material powder

The correlation between the above mentioned parameters is:

$$P=\sigma_c S \qquad (1)$$

σ_c is closely related to the hardness of powders.

As the hardness of the metallic powder increases during the compaction (strengthening mechanisms), then the compression force must be chosen to be greater than the value calculated on the basis of Eq. (1).

The contact area variation, the number of contacts and the porosity of the spherical bronze particles is shown in Fig. 1b. According to Fig. 1 (a and b), the number of contacts and the contact surface between the particles increases with

the increase of the applied pressure, without decreasing the porosity [21-22].

a. Stress-Strain relations in densification mechanism

According to the mixture rule, the composite yield strengths is the weighted average of the yield strengths of the components:

$$\sigma_c = \sigma_p V_p + (1-V_p)\ \sigma_m \qquad (2)$$

where σ_c, σ_m, σ_p, represent the yield strengths of the composite, matrix or particles and the V_p represent the volume (fraction) proportion of the particles. Due to the resistance of the material against deformation (external stress), the internal stresses in the particles increases. If the applied load is released before the deformation reaches a specific critical value, the particles will deform elastically.

Thus, when increasing the volume fractions V_c of hard ceramic (e.g. SiC) particles in soft matrix (e.g. Al alloys), the yield strength of the composite increases and the contact surface areas of the mixtures at the same pressure will decrease. The deformation is reversible and the particles return to their original shape. Before this critical value, the stress is linearly proportional to the deformation [19] and is characterized by the elastic or Young's modulus (E, Fig. 2a) [20]..

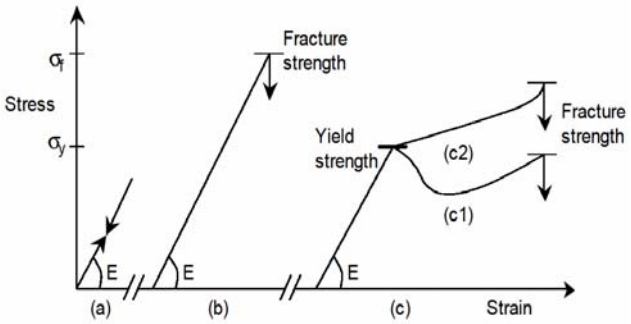

Figure 2. Macroscopic stress-strain relations: a) reversible elastic deformation; b) brittle behaviour; c) ductile behaviour (c1. normal plastic flow; c2. strain-hardening) [20]

The second stage can be divided also into two major mechanisms:

(i) the brittle ceramic particles are fractured at a certain stress value of the σ_f (fracture strength). The brittle particles may fracture under stress, leading to mechanical interlocking (brittle behaviour (Fig. 2b and Fig.3);

(ii) after reaching the critical stress σ_y, the ductile particles begin to deform plastically: (1) ductile behaviour with normal plastic flow (Fig.2 c_1) or (2) they have ductile behaviour with strain-hardening (the material breaking eventually occurs at very high deformations, Fig. 2 c_2.).

The way when powdered materials behave ductile, fragile or ductile-fragile under the action of compressive forces depends on the material and its physical conditions.

In order to model the cold compression behaviour of metal-ceramic powder mixtures (a mixture of hard and soft particles) several simplifications have been made, such as that the mixtures are homogeneous, the contact forces between the particles are equal in the same direction.

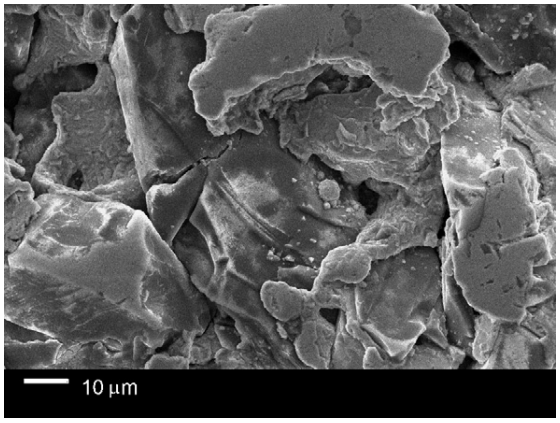

Figure 3. Ceramic fracture in Cu-Al_2O_3 powder mixtures cold compacted at 347 MPa [23]

The particles have a spherical shape of the same or different dimensions [24] or dimensions, or take into account the frictional forces between the particles.

For elucidation of the phenomena that arise in the compaction of metallic and ceramic powders mixtures, Lange et al. [25] have developed a model of hard and soft spheres of different dimensions. The authors suggest *two main mechanisms for* explaining *cold compression behaviour*:

(1) *the densification of each composite mixture* in comparison with densification of exclusively soft powders (the powders for soft, metallic matrix). In this case, the densification can be inhibited by the presence of hard particles, which is confirmed by the fact that the soft particles of metallic material suffer an additional deformation due to the partial filling of the areas around the hard particles;

(2) *the loads are not entirely transmitted to the soft particles* due to the formation of a continuous network of hard particles that take up some of the load.

Martin and Bouvard [22] have also come to the same conclusion by modelling the compression behaviour of hard and soft powder mixtures by DEM method, namely that the hard particles carry a large part of the pressing load as well as a part of the deformation of the soft particles.

Bouvard and Lange [26] proposed an analytical approach combined with a numerical simulation of the infiltration of the hard particles between the soft particles according to the size and fraction of the hard and soft particles and confirmed that according to the experimental investigations densification is much more difficult for mixtures of metallic and ceramic powders over metallic ones [27]

The degree of densification is influenced by the size, shape, surface state and particle distribution[12, 13]. Cazotti and others [17] have shown that the large particles (70 μm) are deformed more easily than thick ones (8 μm), and densification is greater in this case, ie at much lower pressures than fine powders.

C.A. Leon *et. al.* [23] studied the cold compaction behaviour of Cu-Al_2O_3 powder mixtures through two methods: conventional P/M with mixture of Cu and alumina as elemental powders and the other one, P/M with modified powder deposition (copper coated Al_2O_3) as raw materials.

In Fig. 4a we observed the influence of size of Cu on densification behaviour and the comparison of densification of Cu powders with alumina (ceramic) powders. In Fig 4b , the porosity of cold compacted (347 MPa) of Cu-Al_2O_3 mixtures function of ceramic content. The densification of Al_2O_3 powders is with 40% lower than that of the Cu powders.

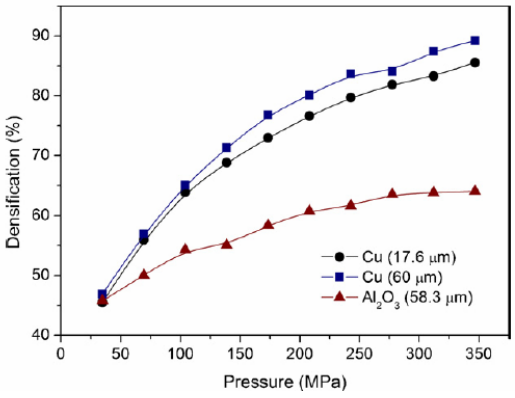

a)

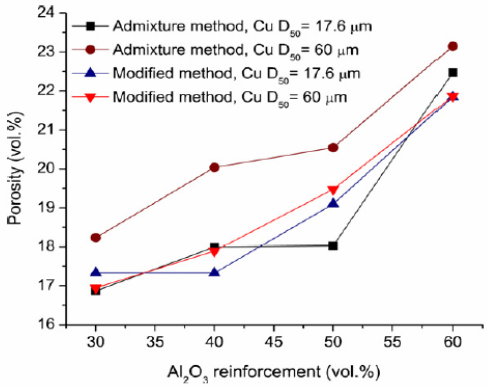

b)

Figure 4. Behaviour of Cu-Al2O3 powder mixtures cold compacted at 347 MPa: a) Compressibility behaviour of as-received Cu and alumina elemental powders and b) Porosity of cold compacted (347 MPa) of Cu-Al2O3 mixtures function of ceramic content [23]

We also observe a better densification of large copper particles (60 μm) than those with fine particles (17.6 μm).

This is explained by the fact that the smaller particle size results in a larger contact surface, and as a result, an increase in friction between the particle , resulting a higher yield stresses.

In addition, fine particles are more sensitive to hardening by plastic deformation (work hardening) and consequently their reduce the compressibility.

C. Ghita and I.N. Popescu [16] respectively S.Sivasankaran et. al. [28] have been demonstrated by them experimental researches that by adding the hard and fragile powders in the soft aluminium alloy powder mixtures, the compressibility decreases, this decreasing is in accordance with the experimental compressibility curves (Fig.5 and 6).

The effect of the nanocrystallite matrix particle size reduction due to incorporation of nano-sized titania considerably reduced the relative density at low compaction pressure (<250 MPa).

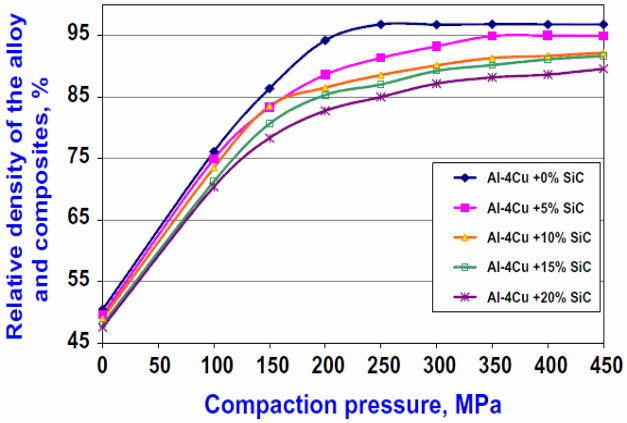

Figure 5. The densification curves for Al4Cu/SiCp composites[6]

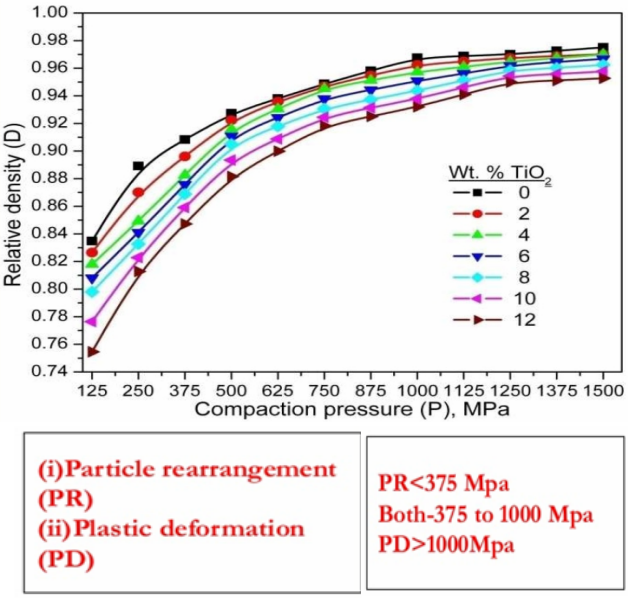

Figure 6. Compressibility curves of AA6061-x wt.% TiO_2(x=0, 2, 4, 6, 8, 10 and 12) nanocomposite powders as a function of compaction pressure at various TiO_2 [28] .

This decreased relative density with the increase of nano-sized titania content in the nanocrystallite matrix in the particle rearrangement mechanism domain was due to work hardening effect.

On the other hand at high compaction pressure the rate of decreased relative density in the plastic deformation domain was lower than particle rearrangement mechanism due to drastic powder morphology reduction. Also, this decreased relative density was also due to increasing of stress shielding effect by titania addition [28].

Also, Cazzoti et.al. [17] confirm that the presence of the Al_2O_3 reinforcing particles with larger size in aluminium matrix composite produces an increase in the compressibility of the powder when 5% and 10% by volume of reinforcement is added.

But the addition of 15% $Al_2O_3$of this reinforcement causes the opposite effect, that is, it decreases the compressibility of the powders [17] (Fig. 7).

Roberts and Rowe [29, 30] demonstrated that materials possess a critical particle diameter at which the

densification mechanism turns from fragile to ductile and the particle size decreases (Fig.8).

The stress necessary to cause particle fracture increases when the particle size decreases, whereas the stress causing plastic deformation of a material is independent of the particle size. When the fracture stress reaches the level of the yield strength, particles with diameters lower than the critical diameter will yield instead of fracturing.

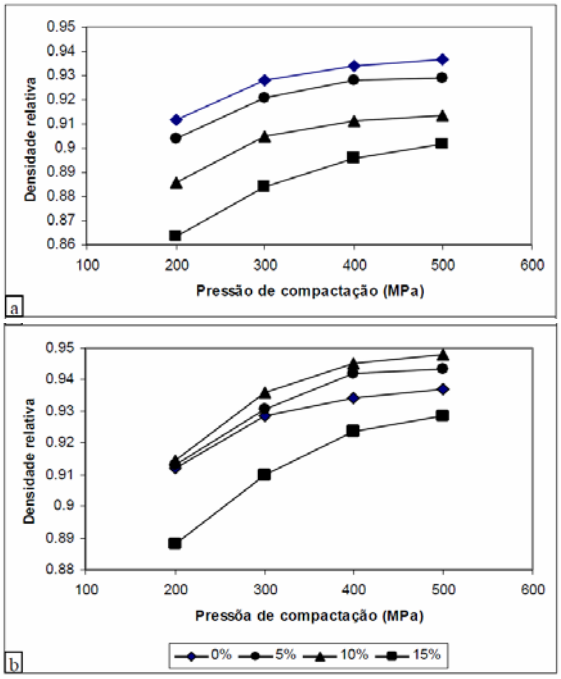

Figure 7. Compressibility curves of ALUMIX 123® aluminum powder (0% reinforcement) and reinforced composites with different amounts of Al_2O_3 powder of smaller size(8 μm) (a) and larger size (70μm) (b) [17]

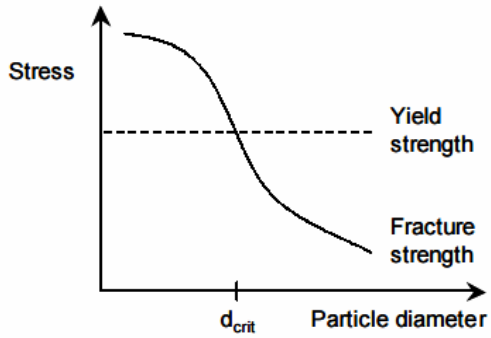

Figure 8. Schematic representation of the particle size effect on yield strength or fracture strength [29, 30]

Achieving a dense packing of particulate powders involves a large particle mobility (powders fluidity) characterized quantitatively by the apparent and relative density of the powders, the porosity of the material and the flow rate of the powder.

Powders with irregularly shaped particles with laced edges and rough surface flow more heavily than spherical shapes due to friction between the particles and thus will have a lower packing degree and a less compaction behaviour.

Instead, particles with spherical particles (in the case of a mixture of un-reinforced aluminium powders or low reinforcement particles with SiC particles [13] and a smooth surface, perform better when pressed, giving more compact powders by a better interlocking of particles, sliding and rotation of them.

Additionally, the packaging is more regular, resulting in a uniformly distributed porosity when powders are compressed. Better packaging has been shown to be in the case of different grains - for example a mixture of two spherical particle fractions, a fraction of 1 mm in diameter and the other one with a diameter of 0.001 mm - when fine particles can hypothetically occupy the largest voids. In this ideal case, the compaction increasing to about 80%.

For this reason, the actual porosity of the experimental powders is higher than that calculated on the basis of systematic packaging models [31] .

Similarly, Zavaliangos and Laptev [32] demonstrated the importance of the relative particle arrangement during compression. These authors have shown that cyclical pressures greatly enhance composite material consolidation, leading to better packaging. Another important factor of the density of the respective densification is the ratio of the particle sizes in the mixture: the high ratio of the particles increases the degree of compaction but in a proportion that does not cause separation of the large particles by the fine particles. If there is a large amount of fine powder in relation to the thick (coarse) ones, the porosity will increase [13]. With further increase of applied pressure, the number of contacts increases and the density of the compacted bulk tending towards to the true densities of the component ingredients, leading to porosity decreasing (*stage III*) [12-22].

This is explained by packaging - repackaging of metallic and ceramic particles at higher pressures. In the course of compaction not only plastic deformation of the particles occurs, but in some particles the deformation is elastic. When removing the green compacts from the die, these elastic deformations (compression) disappear and a sudden expansion of the workpiece volume occurs *(the post-elastic effect* appears) [33].

b. The post-elastic effect

During and after the removal of the applied load, a compressed powder generally shows an elastic recovery of its volume as an effect of stress relaxation. In case of a permanent deformation, the volume expansion will be small, whereas large compact powder relaxations are caused by an important elastic component The compact powder relaxation is commonly expressed by a change in compact height, volume or porosity) [33]..

The green compact expansion expressed as porosity expansion was found to be independent of the applied load. The green compact relaxation is influenced by the compaction speed) [34] and particle size. The post-elastic effect of hard and fragile green compact powder mixtures is higher than that obtained from soft and plastic materials. This is explained by the fact that, at the same compression pressure, the strength of the hard particle compact is lower than the soft particles, thus increasing the role of the elastic deformations compared to the plastic [13-35].

3. CONCLUSIONS

After review the cold compaction of metal (Al and Cu alloys) with ceramic powder (Al_2O_3, SiC, TiO_2) mixtures of different applied pressures and different amount of components, we concluded that the high powder

compression capacity (best densification) is given by: (a) smooth, regular particle surface; (b) different particle size grains, thus choosing the fine particles to fill the voids created by the coarse particles; (c) the most part of the pressing die volume is occupied by coarse particles; the difference in size between the fine particles and the thick ones is very high; (d) the quantity of fine particles is not very large in relation to the thick ones in order not to separate them; (e) lower hardness (high plasticity) of the particles or the existence in the smallest quantities of composites of hard ceramic particles; and (f) particles with as little oxide as possible (the oxygen content of the powder must not exceed 1.5%).

REFERENCES

Journals:

[5] S. Antonyuk, J. Tomas, S. Heinrich, L. Mörl, Micro–macro breakagebehaviour of elastic–plastic granulate by compression, Chemical Engineering and Technology 28 (2005) 623–629.

[6] S. Antonyuk, S. Heinrich, J. Tomas, N.G. Deen, M.S. van Buijtenen, J.A.M. Kuipers, Energy absorption during compression and impact of dry elastic–plastic spherical granules, Granular Matter 12 (2010) 15–47.

[7] Rusanescu C.O , Jinescu C, Rusanescu M., Enescu M. C., Anghelina F. V., Stoian E. V. , Despa V., Mathematical Modelling of the Stress-Strain Curve for 31VMn12 Ecological Steel, Materiale Plastice 54 (3) (2017) 409-413.

[9] D. Gethin, A.K. Arin, D.V. Tran, R.W Lewis, , Compaction and Ejection of Green Powder Compacts, Powder Metallurgy, 37(1) (1994) 42-54.

[10]T. Sheppard, H.B.McShane, Strength of Cold-Pressed Compacts , Powder Metallurgy, 23 (3).(1980) 120-124.

[11] F. Fischmeister, HE. Arzt, Powder Metallurgy, Densifcation of Powders by Particle Deformation, 26(2) (1983) 82-88.

[12] I.N. Popescu, R. Vidu, Compaction of Metal - Ceramic Powder Mixtures. Part. 1, ARA Journal of Sciences, old ISSN 0896-1018, in press.

[13] I.N. Popescu, S. Zamfir, F. V.Anghelina, C.O. Rusănescu, Fabrication through P/M of ecological aluminum based composite materials. Part 1-Characterization and densification of mixture powders Proceedings of the 2nd Int. Conference on MEQAPS, Constantza, Sep 03,-05(2010) 200-205.

[16] C. Ghiță, I.N. Popescu, Experimental research and modelling of compaction behaviour of Al based composite with SiC particles, Comp Mater Sci, 64 (2012) 136-140.

[17] C. Cazotti, J.L.A. Oliveira, J.B. Fogagnolo, Efeito da Adição de Partículas de Al2O3 sobre a Compressibilidade de Pós De Ligas De Alumínio, 17o Proceedings of CBECIMat, 15 -19 de November, Foz do Iguaçu, PR, Brasil (2006) 7452.

[18] R. Panelli, F Ambrózio Filho, Compaction Equation and Its Use to Describe Powder Consolidation Behavior

Powder Metallurgy, 41(2)(1998) 131.

[19] C. Ghiță, N. Pop, I.N. Popescu, Existence result of an effective stress for an isotropic visco-plastic composite, Comp Mater Sci, 64 (2012) 52-56.

[20] van Veen, B., PhD Thesis Compaction of powder blends: effect of pores, particles and percolation on tablet strength, Groningen (2003).

[21] H.F. Fischmeister, E. Arzt, L.R.Olsson, Particle Deformation and Sliding during Compaction of Spherical Powders: A Study by Quantitative Metallography, Powder Metallurgy 21 (4) (1978).179-187.

[22] C.L. Martin, D. Bouvard, Study of the cold compaction of composite powders by the discrete element method, Acta Materialia 51 (2003) 373–386

[23] C.A. Leon, G. Rodriguez-Ortiz, E.A. Aguilar-Reyes, Cold compaction of metal–ceramic powders in the preparation of copper base hybrid materials, Materials Science and Engineering A 526 (2009) 106–112.

[24] E. Arzt, The influence of an increasing particle coordination on the densification of spherical powders Acta metall. mater., 30 (1982).1883-1890. ,

[25] F.F. Lange, L. Atteraas, F. Zok, J.R. Porter. Deformation consolidation of metal powders containing steel inclusions Acta Metall. Mater. 39 (1991).209-219.

[26] D Bouvard, FF. Lange, Relation between percolation and particle coordination in binary powder mixtures, Acta Metall Mater 39(12)(1991). 3083.

[27] C.D. Turner, M.F. Ashby, The cold isostatic pressing of composite powders, Acta Mater. 44 (1996).4521-4530.

[28] S. Sivasankaran, K. Sivaprasad, R. Narayanasamy, Vijay Kumar Iyer, Powder Technology 209 (2011) 124.

[29] R.J.Roberts, R.C . Rowe, The compaction of pharmaceutical and other model materials – a pragmatic approach Chem. Eng. Sci., 42(4) (1987) 903-911.

[30] R.J.Roberts, R.C.Rowe, Brittle/ductile behaviour in pharmaceutical materials used in tabletting , Int. J. Pharm., 36 (1987) 205-209.

[32] A. Zavaliangos, A.Laptev, Acta Mater ;48(10) (2000) 2565.

[33] K .Van der Voort Maarschalk, K. Zuurman, et.al, Porosity expansion of tablets as a result of bonding and deformation of particulate solids Int. J. Pharm., 140 (1996)185-193.

[34] K .Van der Voort Maarschalk , H.Vromans, et.al. , The effect of viscoelasticity and tabletting speed on consolidation and relaxation of a viscoelastic material, Eur. J. Pharm. Biopharm., 42 (1996)49.

[35] I.N. Popescu, Researches on development of new composite materials with Al and Al alloys matrix, Ph.D. Thesis, Bucharest, 2006.

Books:

[1] Randall M. German A-Z of Powder Metallurgy, Elsevier, 2005

[2] Erhard Klar, Prasan K. Sama, Powder Metallurgy Stainless Steels: Processing, Microstructures, and Properties (Chapter 5), ASM International Publisher, ISBN: 978-0-87170-848-9, 2007.

[3] Z. Dragalina Bacinschi, I.N. Popescu, Powder Metallurgy. Production and characterization /Metalurgia Pulberilor. Obținere şi caracterizare, (bilingual edition), Valahia University Press, 2014, ISBN 978-606-603-114-1.

[4] W. Brian James, Introduction to Powder Metallurgy, ASM Handbook, Volume 7, Powder Metallurgy, P. Samal and J. Newkirk, editors, 2015.

[8] I.N. Popescu, Materiale Compozite. Vol. 2-- Obținerea prin Metalurgia Pulberilor a Compozitelor pe bază de aluminiu/ Composite Materials, Volume 2. Powder Metallurgy Processing of AMCs, Reflection Publishing USA, , Editor Ruxandra Vidu , ISBN-13: 97819366292, 2013.

[14] R.M.German, Particle Packing Characteristics, MPIF, Princeton, NJ, 1989.

[15] W.D. Jones, Fundamental Principles of Powder Metallurgy, Edward Arnold Publishers, London, 1960.

[31] S. Joel Hirshborn, Introduction to Powder Metallurgy, 1969.

DE GRUYTER OPEN

The Scientific Bulletin of VALAHIA University
MATERIALS and MECHANICS –Vol. 16, No. 14

DOI 10.1515/bsmm-2018-0002

COMPARATIVE STUDY OF BIOCERAMIC POWDERS SYNTHESIS BASED ON CALCIUM AND PHOSPHATES

Dan Nicolae UNGUREANU[1], Daniela AVRAM[2], Nicolae ANGELESCU[1], Adrian CATANGIU[1], Florina Violeta ANGHELINA[1], Veronica DESPA[1]

[1]Valahia University of Targoviste, Faculty of Materials Engineering and Mechanics
[2] Valahia University of Targoviste, Faculty of Environmental Engineering and Food Science

E-mail: danungureanu2002@yahoo.com

Abstract. *In this paper is presented a comparative study regarding the synthesis of hydroxyapatite powders. The chosen method of synthesis of this biomaterial was chemical co-precipitation. The structure, size and morphology of the obtained powders were analyzed by X-ray diffraction, infrared spectroscopy - FTIR, dynamic light diffusion DLS tehnique and scanning electron microscopy-SEM. The results obtained were compared with those obtained on a commercial hydroxyapatite powder. Investigation methods have confirmed the synthesis of a high purity hydroxyapatite with a optimal degree of crystallization and crystallinity for the reconstruction and regeneration of hard tissue.*

Keywords: *Ceramic biomaterials, Powders ceramics, Hydroxyapatite, Chemical precipitation*

1. INTRODUCTION

Biomaterials are defined as those natural or synthetic substances used to partially or totally replace an organ / tissue or support a function of the body. These materials can be metallic, ceramic, polymeric or composites. The choice of implant material, one of the above mentioned, are related to the characteristics of prosthetic area [1-3].

According to the body's response, these materials were classified into: nearly inert, bioactive and resorbable biomaterials. Nearly inert biomaterials do not give any adverse reaction from the body and are encapsulated by the surrounding tissue, thus achieving morphological fixation. In the case of bioactive materials, they exhibit perfect interaction with the tissue that binds them, forming an interface with the adjacent tissue. The resorbable biomaterials are so designed as to be replaced by a gradual degradation by the host tissue [4].

Depending on the functional role that ceramic biomaterials perform, they are used as implant materials in various prosthetic devices: as a bone filler in rebuilding the structure of hard tissues affected by various traumas or diseases, in the form of coatings on different substrates, or as a secondary phase in the production of composite materials etc [5-7].

Nearly inert bioceramics include alumina, zirconia, carbons as bone plates and screw, components of total hip prosthesis, dental reconstruction, heart valves etc. Corals, calcium sulphates, tricalcium phosphate are a few of the calcium and / or phosphorus compounds known as resorbable bioceramics. The applications of these materials are related bone filler in case of trauma, disease or dental defects, ocular implants etc [4-6].
Bioactive ceramics include glasses, glass ceramics and hydroxyapatite. In the category of bioactive glasses, the most well-known composition is 45S5 or Bioglass. The applications of these materials are related to maxillofacial reconstructions, coatings of inert prothesis, bone filler etc [4, 7, 8].

Biological apatite is the mineral phase of harsh tissues in vertebrates. It is encountered in the bone and tooth mineral structure - in dentine and dental enamel, but also in the case of pathological calcifications such as kidney stones, salivary gland and stones etc. [9]. What distinguishes biological from the synthetic apatites, obtained in the laboratory, refers to chemical composition, stoichiometry, physical and mechanical properties. Typically, biological apathy are deficient in calcium as a result of numerous substitutions in their structure. Regarding chemical composition, biological apatites are described by the following chemical formula:

$$(Ca, M)_{10} (PO_4, CO_3, Y)_6 (OH, F, Cl)_2$$

where M is a monovalent cation (Na^+, K^+) or divalent cation (Mg^{2+}), and Y represents functional groups such as phosphate (HPO_4^{2-}), carbonate (CO_3^{2-}) etc [10].

This paper presents a comparative study on the structural and morphological characteristics of two hydroxyapatite powders. A commercial hydroxyapatite and a hydroxyapatite obtained by the chemical co-precipitation method were analyzed.

2. EXPERIMENTAL PART

2.1 Method of synthesis

The procedure for obtaining the hydroxyapatite used for this paper was presented in detail in other papers [11, 12]. Obtaining hydroxyapatite powder by chemical co-precipitation was achieved by using two calcium and phosphorus reagents (calcium hydroxide and orthophosphoric acid). The addition of calcium and phosphorus ions to the bioceramic material was achieved by the addition of 22.4 g of $Ca(OH)_2$ and 12 ml of H_3PO_4 in 150 ml and respectively 103 ml of deionized water. The reaction medium was stirred vigorously, and the pH was maintained above 10.5 by the addition of NH_4OH. The aging process of hydroxyapatite lasted 2 days at a constant temperature of 60^0C. After washing and filtration, the material obtained was dried in the oven at 110^0C and finally was heat treated at different temperatures. Commercial hydroxyapatite was purchased from Acros Organics Belgium.

2.2 Sample characterization

The obtained hydroxyapatite powders along with the commercial one were analyzed structurally by X-ray diffraction. The crystalline phases present in the hydroxyapatite powder, crystallization degree and crystallite size were highlighted. For this purpose, a Bruker AXS Advance D8 $Cu_{K\alpha}$ (λ = 0,15406 Å), U= 40 kV, I = 30 mA was used. The scanning was set in the range of 20 ° and 60 ° 2θ with a step of 0.04^0 2θ/s.

Molecular groups such as phosphate, carbonate and hydroxyl have been highlighted through the FTIR method. For this investigation, a Bruker Tensor 27 spectrometer was used. The measuring range was between 4000 and 400 cm^{-1} at a resolution of 2 cm^{-1}.

The dimentional analysis was performed by the Dynamic Light Scattering (DLS) technique by using the Plus 90 - Brookhaven Instruments Corporation Zetasizer with a measuring range of 2 nm - 5 µm and a sample volume from 1 to 3 ml.

The morphology of commercial and obtained hydroxyapatite powders was analyzed with the FE-SEM (Field Emission) scanning electron microscope with maximum magnification of 1,000,000x and minimum resolution of 1 nm at 15 kV and 1.9 nm at 1 kV.

3. RESULTS AND DISCUTIONS

3.1 XRD analysis

Commercial hydroxapatite. In the case of commercial hydroxyapatite, the X-ray diffraction spectrum is shown in Figure 1. The analysis of the obtained data revealed the existence of a powder characterized by a low degree of crystallization, (C_R≈21%), according to the calculation presented in other papers [11, 12].

Regarding the composition of the crystalline phases, the diffraction analysis reveals that hydroxyapatite is the only crystalline phase present in the structure of the analyzed powders. This phenomenon has been highlighted by comparing the diffraction lines obtained with those of the PDF2: 00-009-0432 file.
The most important diffraction lines are those found at 25.8 2θ, 31.8 2θ, 32.2 2θ, 32.92 2θ, 46.66 2θ, 49.55 2θ.

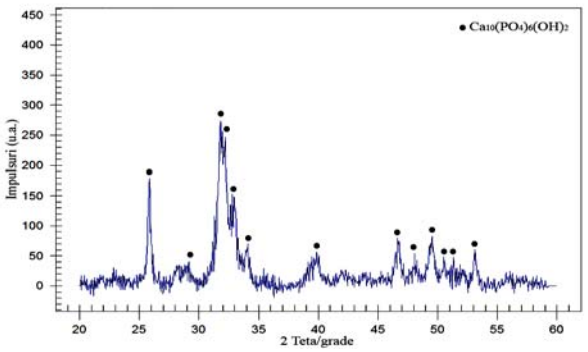

Figure 1. XRD spectra for comercial hydroxyapatite

The crystallites size of commercial hydroxyapatite was calculated at about 28 nm.

Synthesized hydroxyapatite. In this case, are presented information on the heat treated sample at 800^0C. As a result of the increase of the thermal treatment temperature, the degree of crystallinity increased from 23% to 86%. The peaks attributed to hydroxyapatite are located at 25.85 2θ, 31.77 2θ, 32.17 2θ, 32.9 2θ, 35,46 2θ, 39,2 2θ, 39.82 2θ, 46.7 2θ, 50.53 2θ, 52.06 2θ and 53.17 2θ

In such conditions, there is also a very small occurrence of calcium oxide (CaO), revealed by the diffraction line at 37,29 2θ. This phenomenon is explained by incorporation into the hydroxyapatite structure of carbonate CO_3^{2-} groups. It is known that the thermal stability of hydroxyapatite decrease in the presence of calcium.

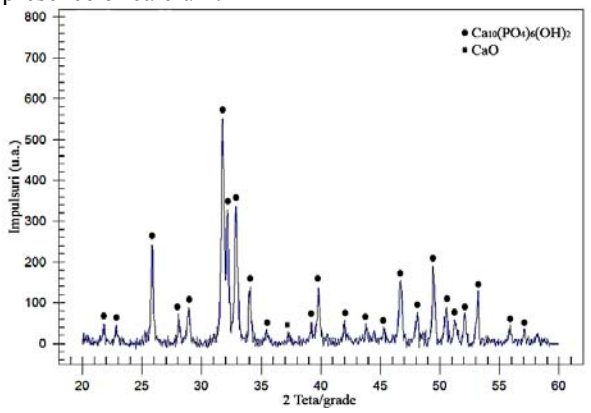

Figure 2. XRD spectra for hydroxyapatite powders heat treated at 800^0C

Regarding the crystallite size of the hydroxyapatite powders, an increase of the mean value from 20 nm to 32 nm after heat treatment at 800^0C has been achieved .

3.2 FTIR analysis

Commercial hydroxapatite. Figure 3 shows the FTIR spectra of commercial hydroxyapatite. The presence of bands at 3571 cm^{-1} and 630 cm^{-1} are characteristic for hydroxyl groups (OH^-) present the hydroxyapatite structure.

The peaks characteristic of phosphate groups (PO_4^{3-}) are located at 566 cm^{-1}, 604 cm^{-1}, 962 cm^{-1}, 1042 cm^{-1} and 1095 cm^{-1}. At the same time, the presence of bands at 3550 cm^{-1} and 1650 cm^{-1} is attributable to the existence of crystallized water in the hydroxyapatite structure.

The presence of carbonate groups (CO_3^{2-}) in the commercial hydroxyapatite structure was evidenced by the presence of the band at 1420 cm^{-1}.

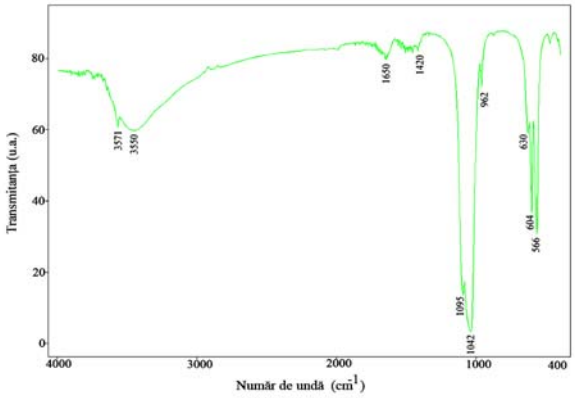

Figure 3. FTIR spectra for comercial hydroxyapatite

Synthesized hydroxyapatite. After the heat treatment at 800^0C, the hydroxyapatite spectrum (Figure 4) highlights the presence of carbonate groups (CO_3^{2-}) in the structure of the analyzed powder by the peaks at 1458 cm^{-1}, 1419 cm^{-1} and 875 cm^{-1}. PO_4^{3-} groups are identified at 567 cm^{-1}, 602 cm^{-1}, 962 cm^{-1}, 1042 cm^{-1} and 1095 cm^{-1}.

The two peaks at 3570 cm-1 and 633 cm-1 are attributed to hydroxyl groups (OH^-) in hydroxyapatite structure.

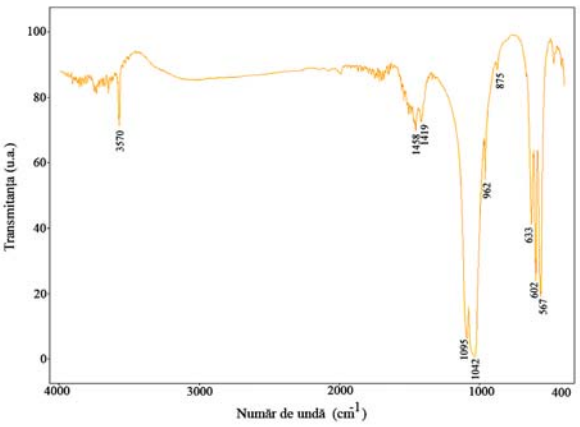

Figure 4. FTIR spectra for hydroxyapatite powders heat treated at 800^0C

3.3 DLS analysis

Commercial hydroxapatite. Particle size analysis on the commercial hydroxyapatite sample reveals a bimodal distribution of the powders. Two granulometric classes was identified : 95.8 - 156.9 nm and 257 - 420.8 nm. Hydrogenapatite particles with a hydrodynamic diameter of 95.8 nm, 108.4 nm, 122.6 nm, 290.7 nm or 420 nm were identified (Figure 5). This demonstrates a non-uniform distribution of the particles in the comercial hydroxyapatite powder. In this case, the average particle size of the hydroxyapatite was 139.2 nm.

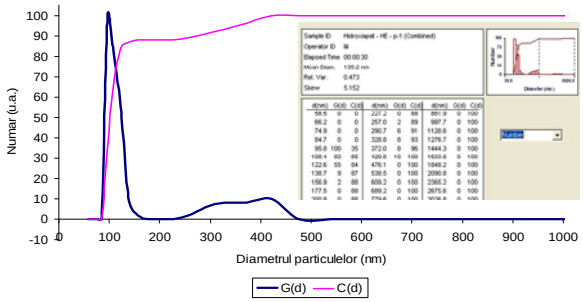

Figure 5. Particle size analysis for comercial hydroxyapatite: G(d) – general distribution; C(d) – cumulative distribution

Synthesized hydroxyapatite. Figure 6 shows the particle size analysis for the synthesized hydroxyapatite according to the presented process and heat treated at 800^0C. There is a unimodal distribution, with a mean particle size diameter of 247.7 nm [12].

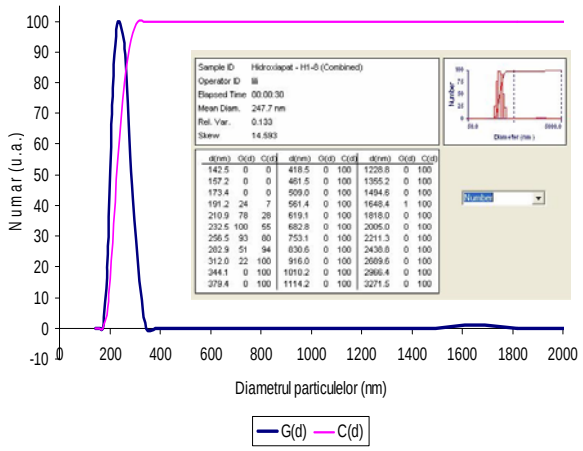

Figure 6. Particle size analysis for synthesized hydroxyapatite: G(d) – general distribution; C(d) – cumulative distribution

3.4 SEM analysis

Commercial hydroxyapatite. Figures 7 and 8 shows SEM micrographs at 1000X and 5000X magnifications of commercial hydroxyapatite powder. From the two images one can observe the appearance of a fine grain powder with homogeneous distribution and well defined distribution. It is also noted the presence of numerous particle agglomerates with sizes that can reach the order of the micrometers.

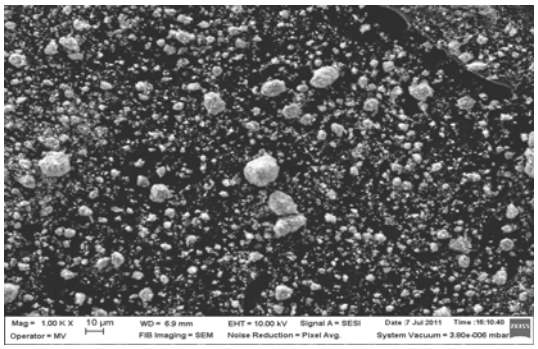

Figure 7. SEM analysis for commercial hydroxyapatite (Magnification: 1.000X)

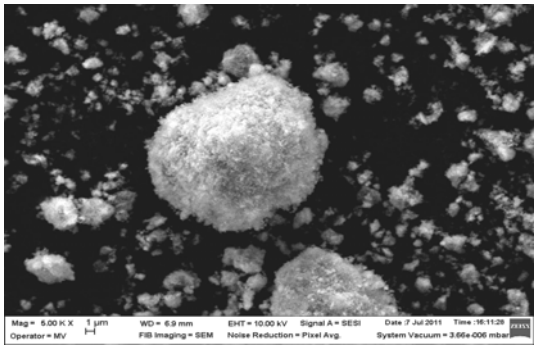

Figure 8. SEM analysis for commercial hydroxyapatite (Magnification: 5.000X)

Synthesized hydroxyapatite. As a result of heat treatment at 800^0C there is a complete elimination of chemically bound water from the structure of hydroxyapatite, a phenomenon that could result, on the one hand, in the fragmentation of the hydroxyapatite particles and on the other hand the giving of a more irregular aspect of their surface . This is highlighted in the SEM micrograph shown in Figure 9.

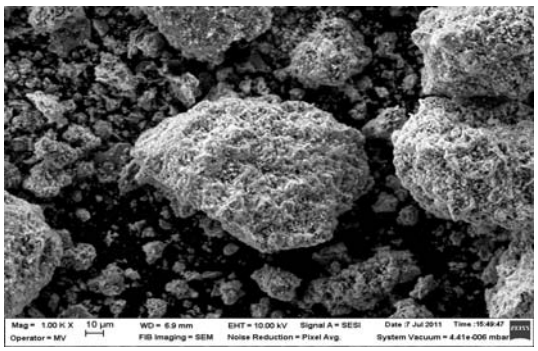

Figure 9. SEM analysis for synthesized hydroxyapatite (Magnification: 1.000X)

4. CONCLUSIONS

In this paper has been presented the comparative results for two bioceramic powders used in regeneration and reconstruction of hard tissues.

X-ray diffraction analysis confirmed the presence of hydroxyapatite for the two samples (commercial hydroxyapatite and synthesized hydroxyapatite), the small amount of CaO being the result of impurities during heat treatment. In the case of crude synthesized HAp sample, the presence of CaO was not identified.

The FTIR analysis revealed the presence of the PO_4^{3-}, CO_3^{2-}, OH^- molecular groups for the two analyzed HAp samples, confirming the results obtained in the X-ray diffraction analysis.

For both samples, nanoparticles has been found after DLS analysis. The results of particle size analysis could be better after the improvement of the synthesis technology.

SEM analysis highlights hydroxyapatite particles whose morphology makes them ideal for subsequent implantation applications.

REFERENCES

[1] D. F. William – The William Dictionary of Biomaterials, Liverpool, 1999.

[2] L. L. Hench – Ceramics, Glasses, and Glass–Ceramics în Biomaterials Science, An Introduction to Materials in Medicine; Ed. Academic Press, p. 73–84, 2004.

[3] L. L. Hench, J. Wilson - Bioceramics, Materials Research Society Bulletin p. 62-74, 1991.

[4] J. B. Park, R. S. Lakes - Biomaterials - An Introduction, Second Edition, Plenum Press, New York, 1992.

[5] L. L. Hench – Bioactive Ceramics, in Bioceramics: Material Characteristics vs In Vivo Behaviour, Vol.523, p. 54, Ed. P. Ducheyne and J. Lemons, 1998.

[6] M. J. Freeman, D. E. McCullum, P. K. Bajpai - Use of ALCAP ceramics for rebuilding maxillo-facial defects, Trans. Soc. Biomat, 4, p.109, 1981.

[7] P. K. Bajpai, C. M. Fuchs, M. Strnat - Development of alumino-calcium phosphorous oxide (ALCAP) ceramic cements în: Biomedical Engineering IV - Recent Developments. Proceedings of the Fourth Southern Biomedical Engineering Conference, Jackson, MS, Ed. B Sauer, Pergamon Press, New York p. 22–25, 1985.

[8] W. Höland, W. Vogel, K. Naumann, J. Gummel - Interface reactions between machinable bioactive glass-ceramics and bone, Journal of Biomedical Materials Research,19, p. 303–312, 1985.

[9] R. Z. Le Geros - Apatites in Biological Systems, Progress in Crystal Growth and Characterization of Materials, 4, p.1-45, 1981.

[10] R. Z. Le Geros - Calcium Phosphate in Oral Biology and Medicine, Monographs in Oral Science, 15, Ed. HM Myers, S. Karger, Basel, 1991

[11] N Angelescu., D.N., Ungureanu F.V. Anghelina , Synthesis and characterization of hydroxyapatite obtained in different experimental conditions, The Scientific Bulletin of VALAHIA University – MATERIALS and MECHANICS, 6(9), 15-18, 2011

[12] D.N. Ungureanu N. Angelescu, V. Tsakiris, V. Marinescu, Investigations regarding chemical synthesis of calcium hydroxyapatite, Romanian Journal of Materials, 42(1), 52 – 60, 2012.

DE GRUYTER OPEN

The Scientific Bulletin of VALAHIA University
MATERIALS and MECHANICS –Vol. 16, No. 14

DOI 10.1515/bsmm-2018-0003

STRUCTURAL AND MORPHOLOGICAL INVESTIGATIONS ON CORE-SHELL HYBRID MICROPARTICLES

Dragoş Viorel BREZOI

Valahia University, Targoviste, Romania

E-mail: dragosh_brezoi@yahoo.com

Abstract. *The paper presents a micro encapsulation method of α-Fe_2O_3 nanoparticles in PEG4000. A suspension of α-Fe_2O_3 nanoparticles and dissolved PEG is sprayed through a nozzle at atmospheric pressure. After rapid expansion, core-shell composite microparticles that don´t tend to agglomerate are obtained. Structure and morphology were investigated by electronic microscopy (TEM and SEM), X-ray diffraction (XRD), and spectral technique (UV-Vis and FTIR).*

Keywords: *α-Fe_2O_3 nanoparticles, Hybrid core-shell composite, PEG4000 microparticles*

1. INTRODUCTION

One of the main objectives in composite engineering is the development of design and obtaining methods of organic-inorganic composites structured in the nanometric and micrometric range. A nanocomposite (the term was proposed in 1970) is a mixture of two phases, one of which has nanometric dimensions (1-20 nm) in at least one direction.

Most important, both in research and in the nanotechnology-based industry is the morphological and dimensional control of nanoparticles, given the large number of applications based on devices created from oxide nanomaterials such as: color-sensitive solar cells [1], hybrid thin films for photovoltaic applications [10], gas and biosensors [2, 8], polymeric membranes with metal oxides [9] or lithium-based batteries [3].

Optimization of such devices can be accomplished on the basis of a better understanding of the physical properties in which quantum mechanics predominates, as well as a better correlation of the design of the material with the application needs, in accordance with the accelerated miniaturization trend. In all applications of nanomaterials, switching from laboratory to industrial scale is an important challenge. In this regard, engineers have developed synthesis techniques, simulation, and modeling methods to facilitate the production of relatively cheap, reliable materials with controlled properties.

In this paper is presented the obtaining of nanocrystalline α-Fe_2O_3 fabricated from colloid. The aim is to develop a method of incorporating iron oxide nanoparticles into polyethyleneglycol (PEG) microparticles in which the particle's size can be controlled without use of toxic solvents or surfactants. Methods of obtaining based on the same principle have been reported but for polymer based composite materials with TiO_2 [4], γ- Fe_2O_3 [5] or SiO_2 [6]. Obtained microparticles may be applied as the cosmetic, printing and electronic materials. The nanoparticles of α-Fe_2O_3 absorb the UV light. To use the α-Fe_2O_3 nanoparticles for cosmetic materials, α-Fe_2O_3 nanoparticles have to microencapsulate into PEG (polyethyleneglycol) shell.

2. EXPERIMENTAL PROCEDURE

2.1. Preparation of α-Fe_2O_3 colloid

The α-Fe_2O_3 colloid was obtained by a hydrolysis reaction of a solution with $FeCl_3$ in slightly acidified water. The obtaining process took place in two stages: the instantaneous amounts of aqueous solution containing $FeCl_3$ (110 ml, 2 mol/l) with HCl (210 ml, 3 mol/l) was successively dropped into a flask, and then diluted with a certain volume of boiling water. This process produced a red-brown transparent sol. Then, the sol was heated into refluxing state and aged at 90 ^oC for 40 hours.

The α-Fe_2O_3 colloid obtained was washed with deionized water several times until the unreacted components (Cl^- ions and Fe_3Cl) were eliminated.

With the help of the electronic transmission microscope JEM 2000 EX (TEM) and scanning electronic microscope JEOL JSM 840 (SEM), the morphology of particles was performed and analyzed. X-ray powder diffraction (XRD) measurement was made on X-ray diffractometer (Kα line of cobalt radiation). The absorption spectrum was recorded using a SPECORD M400 UV–Vis spectrophotometer. FTIR analysis was performed on a Jasco FTIR 4200 spectrophotometer using α-Fe_2O_3 powder pellets pressed together with KBr powder.

2.1. Preparation of core-shell microparticles PEG4000/α-Fe_2O_3

Polyethylene glycol (M.W. PEG4000 = 4000) as shell and α-Fe_2O_3 nanoparticles as core material were used for preparation the composite microparticles. Encapsulation of the iron oxide nanoparticles was realized in a 500 cm high pressure cell provided with a 10 mm round sapphire window. In the first phase, the pre-expansion pressure was raised to the working pressure. The PEG with α-Fe_2O_3 nanoparticles and the co-solvent in well-determined amounts were introduced into the high pressure cell under stirring at 600 rpm for 1 hour. The mixed polymer/oxide solution was sprayed rapidly (under 3 seconds) onto a 1 mm thick target aluminum plate through a capillary nozzle by opening a valve located before the nozzles. The expansion produced polymeric-based composite microparticles. These microparticles were collected after the sedimentation process.

After obtaining process, the microparticles were placed on a small glass plate, covered with a two-sided carbon-like conductive band. For use as the SEM sample, it was metalized by sputtering with a layer of silver–palladium alloy with a thickness of approximately 200 Å.

3. RESULTS AND DISCUSSION

3.1. α-Fe_2O_3 nanoparticles analyzes

Figure 1 shows the TEM image of α-Fe_2O_3 nanoparticles where it is observed that the particles formed are polyhedral with an average side in the range of 18-25 nm which is in agreement with the XRD results.

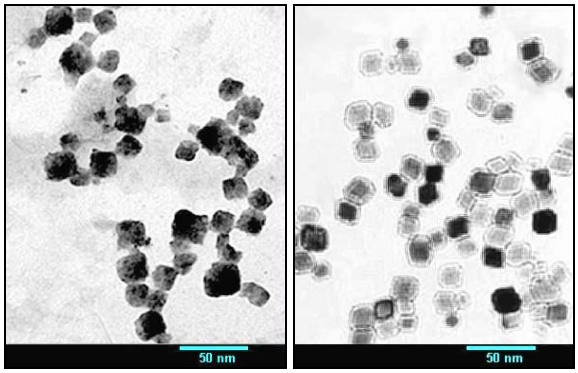

Figure 1. TEM image of α-Fe_2O_3 nanoparticles (2 samples)

The XRD pattern (figure 2) shows that the analyzed particles are nanocrystalline with the size of approximately 20 nm, and the characteristic peaks are specific only to the α phase of Fe_2O_3.

UV-Vis spectral analysis (figure 3) on the α-Fe_2O_3 sample shows maximum absorption in the UV region at 206 nm and 233 nm due to tetrahedral coordinated Fe^{3+} ions and 258 nm, 278 nm due to octahedral coordinated Fe^{3+} ions [7].

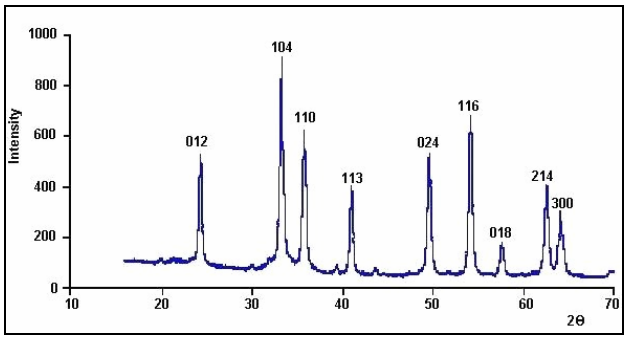

Figure 2. XRD for α-Fe_2O_3

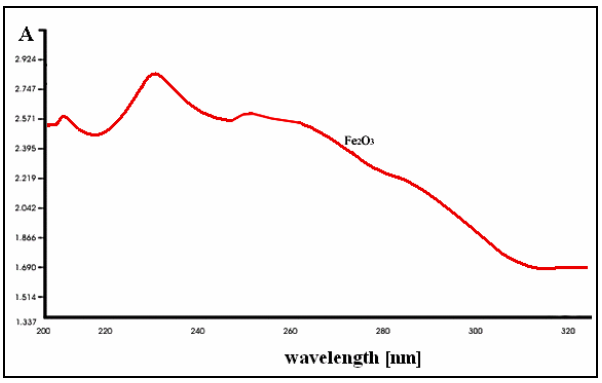

Figure 3. The UV-Vis spectrum of α-Fe_2O_3

FTIR analysis determines the chemical composition of the colloid obtained. Figure 4 represents the FTIR spectrum of powder obtained by drying the colloidal iron oxide.

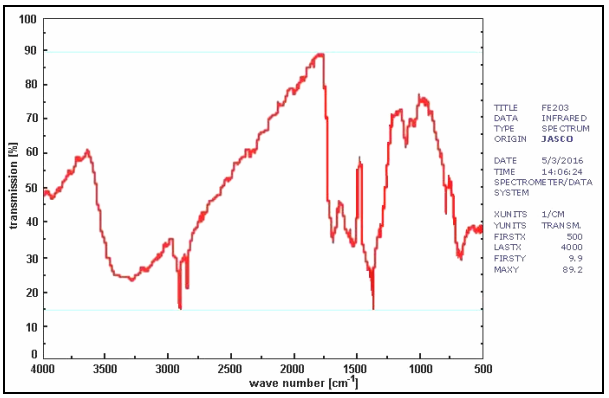

Figure 4. The FTIR spectra of α-Fe_2O_3

The peaks observed in the spectrum can be assigned as follows:

Table1. Assign the peak values of the FTIR spectrum

peak value [cm^{-1}]	*Assigned to…*
692; 788	deformation vibration of Fe–OH groups
3285	O–H stretching vibration of the above groups
1042; 1108	O–H bending vibration
1355	–CH3 bending vibration
2835 and 2904	C–H stretching vibration

The details from the table 1 show that the prepared powder contains PEG and residual FeOOH.

3.2. Morphology of PEG microparticles with α-Fe_2O_3 nanoparticle as core

SEM image of PEG4000/α-Fe_2O_3 core-shell microparticles is shown in figure 5. Ethanol was used as a co-solvent and the pre-expansion pressure was 20 MPa and the temperature was 300 K. The particle sizes are in the range of 15-20 μm and are not agglomerated because ethanol is volatile and a solvent for the polymer. Polymeric microparticles were spherical and did not depend on the nature and dimensions of the oxide nanoparticles that constituted the core.

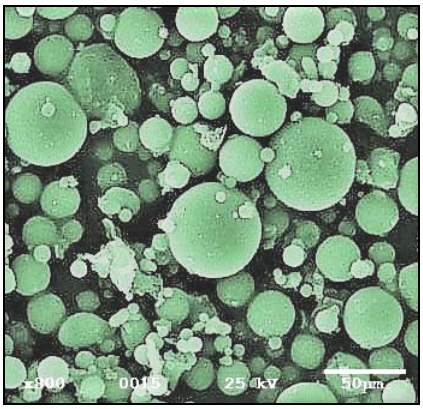

Figure 5. SEM image of the PEG4000 microparticles with α-Fe_2O_3 nanoparticles as core

The suspended α-Fe_2O_3 nanoparticles played the role of nucleation agent in the expanding jet, helping to encapsulate. As a result of precipitation of the PEG, composite spherical microparticles were produced.
Also, the SEM image (figure 5) shows that dimensional distribution is not uniform: very large spherical particles with a diameter of 50 μm, but also very small of a few μm appear. Most of the particles have a diameter of about 20 μm.
It may be considered that the obtained particles are PEG microparticles with core consist of α-Fe_2O_3 nanoparticles, because the agglomerated α-Fe_2O_3 nanoparticles are not observed on the surface of PEG particles by SEM analysis.

4. CONCLUSIONS

To obtain core-shell microparticles with α-Fe_2O_3 nanoparticles core and PEG 4000 shell, the atmospheric pressure spray technique was used. After rapid expansion, microparticles that do not tend to agglomerate are obtained.

Structure and morphology of microparticles were investigated by SEM, TEM, XRD, UV-Vis and FTIR. Ferric oxide nanoparticles have polyhedric shapes and average sizes in the range of 18-25 nm and by encapsulation they do not tend to agglomerate. The obtained microparticles have spherical shape and average diameters about 20 μm.

REFERENCES

[1] Hideo Otaka, Michie Kira, Kentaro Yano, Shunichiro Ito, Hirofumi Mitekura, Toshio Kawata, Fumio Matsui, Multi-colored dye-sensitized solar cells, Chemistry, Volume 164, Issues 1–3, pp. 67-73, 2004;

[2] Dragoş-Viorel Brezoi, Rodica-Mariana Ion, Phase Evolution Induced by Polypyrrole in Iron Oxide – Polypyrrole Nanocomposite, Sensors and Actuators B: Chemicals, Vol. 109, Issue 1, 0925 – 4005, pg. 171-175, 2005;

[3] Lorenzo Zolin, Lithium-Based Batteries, chapter in Large-scale Production of Paper-based Li-ion Cells, pp 13-38, Ed. Springer, 2016;

[4] Matsuyama K, Formation of TiO_2–polymer composite microparticles by rapid expansion of CO_2 saturated polymer suspensions with high shear mixing, Journal of Supercritical Fluids, 40(1), pp117-124, 2007;

[5] Deb, P.; Basumallick, A., Kinetics of γ-Fe2O3 nanoparticle evolution from an organic precursor, Journal of Nanoparticle Research, Volume 6, Issue 5, pp.527-531, 2004;

[6] Matsuyama, Kiyoshi; Kenji Mishima; Kenichiro Hayashi; Ryugen Ohdate, Preparation of Composite Polymer-SiO2 Particles by Rapid Expansion of Supercritical Solution with a Nonsolvent, International Journal of Advanced Research in Electrical Electronics and Instrumentation Engineering, 2003;

[7] Lever, A.B.P., Inorganic electronic spectroscopy, Amsterdam: Elsevier, pp. 862, 1984;

[8] Hua Bai, Gaoquan Shi, Gas sensors based on conducting polymers, Sensors 7(3), pp. 267-307; 2007;

[9] Law Yong Ng, Abdul Wahab Mohammad, Choe Peng Leo, Nidal Hilal, Polymeric membranes incorporated with metal/metal oxide nanoparticles: A comprehensive review, Volume 308, 2 January 2013, Pages 15-33, 2010;

[10] J. Bouclé, P. Ravirajan, J. Nelson, Hybrid polymer–metal oxide thin films for photovoltaic applications, Journal of Materials Chemistry, issue 30, pp. 3141-3153, 2007.

DE GRUYTER OPEN

The Scientific Bulletin of VALAHIA University
MATERIALS and MECHANICS –Vol. 16, No. 14

DOI 10.1515/bsmm-2018-0004

STUDY ON EFFECTIVE ELASTIC PROPERTIES OF $CaMnO_3$

Prapawan THONGSRI

Faculty of Education, Sakon Nakhon Rajabhat University,
680 Nittayo Road, Mueang District, Sakon Nakhon 47000, Thailand

E-mail: pt087245@gmail.com

Abstract. *Calcium manganese oxide ($CaMnO_3$) polycrystalline was synthesized by solid state reaction (SSR) and hot-press (HP) methods. The powder of $CaCO_3$ and MnO_2 were mixed by ball milling then calcined at 850°C for 10 h and hotpressing at 850 °C for 1 h to obtain the $CaMnO_3$ samples. The crystallography of the samples was analyzed by the X-ray diffraction (XRD). The microstructures of the samples were observed by scanning electron microscope (SEM). It was found that, the sintering process influence the crystalline perfection and have a direct impact on the mechanical properties of $CaMnO_3$ and their aging behavior. The values of the effective elastic modulus was 6 GPa and Flexural strength was 0.417 MPa of $CaMnO_3$ were found to be in the range of corresponding values for high performance and possibility fabricated n-type thermoelectric leg.*

Keywords: Mechanical properties, $CaMnO_3$, Elastic modulus, Flexural strength

1. INTRODUCTION

Calcium manganese oxide with perovskite type crystal structure has received much interest in the past decade due to its structural , physical ,magnetical and thermoelectric properties [1]. Ceramic systems with high crystalline content have good fracture resistance but are highly opaque. [2, 3].

Usually at room temperature, most ceramic materials exhibit brittle fracture. Fracture is very difficult to control in the case of materials with cracks and another type of defects. In the case of compression, the rate of crack propagation is lower than in the case of traction. For this reason, the ceramic material has a high hardness. Resistance of the ceramic material is measured by a bending test until break.

The manganese oxide $CaMnO_3$ with perovskite type crystal structure is obtained starting from manganese oxides (stoichiometric mixture powders of $CaCO_3$ and MnO_2) which are mixed by ball milling. Control of microstructure and crystallographic properties are key factors in technology of functional calcium manganese oxide based materials [4].

The perovskite structure $CaMnO_3$ is that in which the Mn is surrounded by six oxygen atoms and the Ca is surrounded by twelve anions. [5]. The values of the effective elastic modulus and flexural strength of calcium manganese oxide were found to be in the range of corresponding values for high performance and possibility fabricated n-type thermoelectric leg.

2. MATERIALS AND METHODS

The compounds from powder of $CaCO_3$, 99.99 % (SIGMAALORICH) and MnO_2, 90.00 % (SIGMAALORICH) are mixed by ball milling technique to obtain $CaMnO_3$ compound.

CaMnO3 compound polycrystalline was synthesized by solid state reaction (SSR) and hot-press (HP) methods. The powder of $CaCO_3$ and MnO_2 were mixed by ball milling then calcined at 850°C for 10 hours and hotpressing at 850 °C for 1 hour to obtain the $CaMnO_3$ samples.

X-ray diffraction (XRD) is a rapid analytical technique primarily used for the identification of crystalline phase of the $CaMnO_3$.

Microstructure of the samples has observed by a scanning electron microscope by using secondary electron detector. The Vicker hardness, density, Young modulus and flexural strength of the $CaMnO_3$ were analyzed.

3. RESULTS AND DISCUSSION

In order to study the structure of sintered $CaMnO_3$ sample with the dimensions of 10.05 mm × 10.25 mm × 1.31 mm have been obtained.

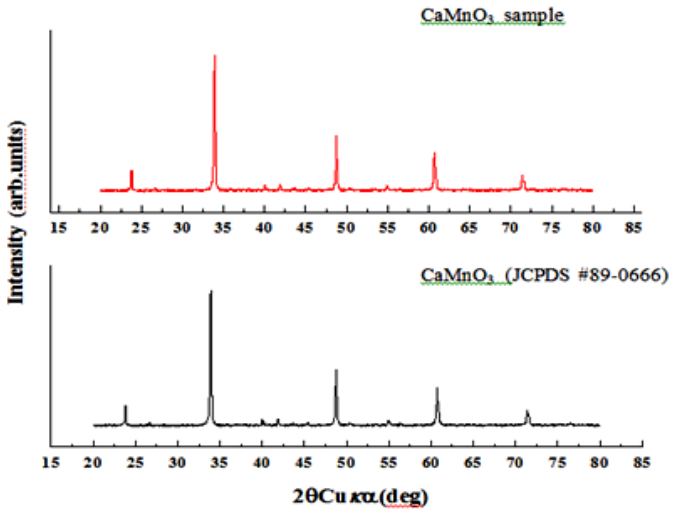

Figure 1. X-ray diffraction of $CaMnO_3$

The result of the X-ray diffraction analysis of $CaMnO_3$ is shown in Figure 1. Many researchers have reported the X -ray diffraction analysis data of $CaMnO_3$.

Crystaline phase of $CaMnO_3$ has been identified by XRD tehnique, in accordance with JCPDS #89-0666 file. The $CaMnO_3$ has orthorhombic perovskite structure.

Table 1. Lattice paprameters, densities of $CaMnO_3$.

Sample	*a*(A°) nm	*b*(A°) nm	*c*(A°) nm	Unit cell Volume (A°³)	Theoretical density (g/cm³)	Experimental density (g/cm³)	Relative density (%)
$CaMnO_3$	0.74142	0.74245	0.73581	0.40504	1.23	1.21	98.1

The elastic modulus or Young's modulus (E) evaluation, sample of dimensions 4 mm in diameter and 2.8 ± 0.1 mm in length was prepared for material. Results is mean value for the core material was 6 GPa. The Young's shear and bulk using a technique modulus of these materials were evaluated using an ultrasonic method. The formula used to calculate the bend strength is given below:

$$E = \frac{FL^3}{\delta 4bd^3} \text{ (rectangular cross section)} \quad (1)$$

where E = elastic modulus (GPa), F = fracture load (N), L = distance between the two supports (mm), δ = midpoint deflection (mm), b = width of the rectangular bar (mm), d = thickness of the rectangular bar (mm).

In case of flexural strength evaluation, sample has a rectangular cross section (4 x 4 mm) and 3-point loading over a span of 12.0 mm. Testing was carried out in air using a servo hydraulic testing machine (Instron) at a crosshead speed of 0.5 mm/min. Results is mean value for the core material was 0.417 MPa. The formula used to calculate the bend strength is given below:

$$\sigma_{fs} = \frac{3F_f L}{2bd^2} \text{ (rectangular cross section)} \quad (2)$$

Where σ_{fs}= flexural strength (MPa), F_f= fracture load (N), L = distance between the two supports (mm), b = width of the rectangular bar (mm), d = thickness of the rectangular bar (mm).

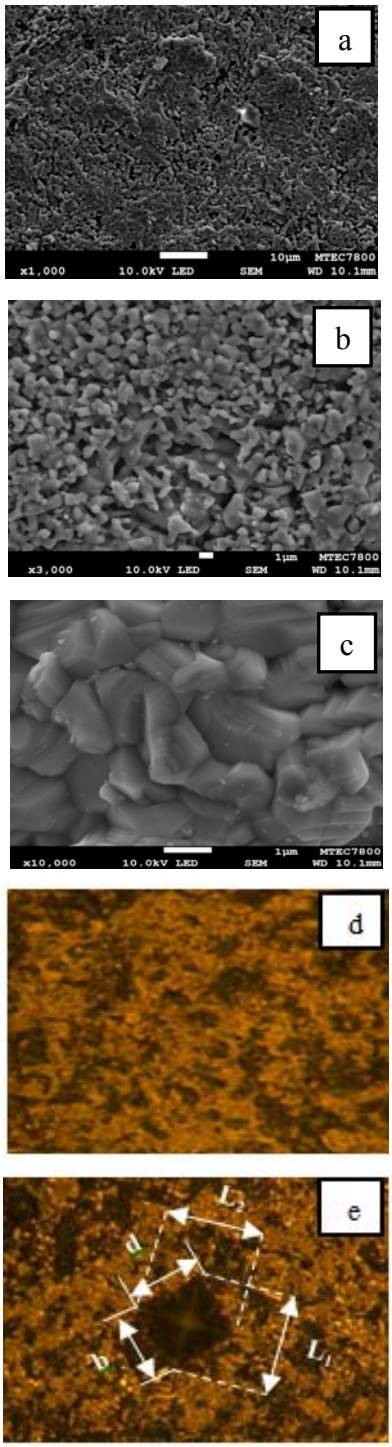

Figure 2. Representative SEM image of the fracture surface of $CaMnO_3$ sample (a), (b), (c) and HMV micro-hardness tester image (d), (e)

The result of the Scanning Electron Microscope (SEM) analysis of $CaMnO_3$ at different magnifications is shown in Figure 2. From the three figures (Figure 2a, 2b and 2c) we can see the crystalline grains of $CaMnO_3$ having the polyhedral shape and the relatively equal size. The indentation shape of micro hardness HV test is shown in figure 2e.

The density value of the $CaMnO_3$ was 1.211 g/cm^3 for MS Semi-Micro Balance Toledo. The hardness value of the $CaMnO_3$ was 115.8 HV were using a Shimatzu HMV Micro Hardness (load: 0.1 HV; dwell time: 10 s).

The microstructures of the $CaMnO_3$ sample was observed with a scanning electron microscope FE-SEM JEOL JSM-6301F. The elemental analysis of the $CaMnO_3$ sample is shown in Fig. 3. For this test energy-dispersive X-ray spectroscopy analytical technique has been used.

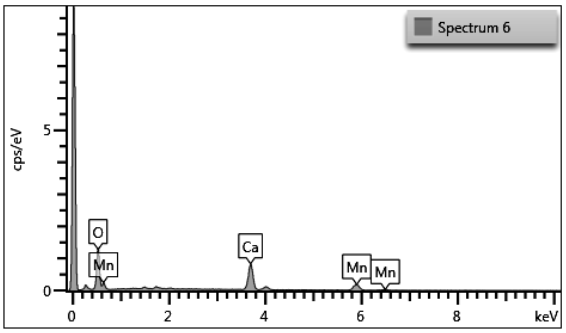

Element	Line Type	Apparent Concentration	k Ratio	Wt%	Wt% Sigma	Standard Label	Factory Standard	Standard Calibration Date
O	K series	0.94	0.00316	1.25	0.02	SiO2	Yes	
Ca	K series	0.79	0.00704	0.78	0.01	Wollastonite	Yes	
Mn	K series	0.80	0.00801	0.99	0.03	Mn	Yes	
Total:				3.02				

Figure 3. Representative EDX analysis of $CaMnO_3$

EDX analysis confirms the presence of calcium, manganese and oxygen in the structure of the ceramic compound obtained.

CONCLUSIONS

Calcium manganese oxide polycrystalline was synthesized by solid state reaction and hot-press methods.

Young's modulus for the $CaMnO_3$ sample was 6 GPa and flexural strength was 0.417 MPa. The density value was 1.211 g/cm^3. The hardness value of the $CaMnO_3$ was 115.8 HV using a HMV (load: 0.1 HV; dwell time: 10 s).

Many values of the effective elastic modulus and flexural strength of $CaMnO_3$ were found to be in the range of corresponding values for high performance and possibility fabricated n-type thermoelectric leg.

ACKNOWLEDGEMENTS

Center of Excellence on Alternative Energy, Research and Development Institution, Sakon Nakhon Rajabhat University for support budget and equipment for analysis sample.

REFERENCES

[1] Prapawan Thongsri and Tosawat Seetawan. Advanced Materials Research (2013);770: 327-330.

[2] Della Bona A, Kelly JR. The clinical success of all-ceramic restorations.2008; 139.

[3] Della Bona A.Bonding to ceramics: scientific evidences for clinical dentistry. 1. São Paulo: ArtesMédicas.2009.

[4] W. Paszkowicz, J. Piętosa, S. M. Woodley, P. A. Dłużewski, M. Kozłowski, C. Martin.Powder Diffraction 2010; 25:46-59.

[5] E.O.Wollan,W.C.Koehler.Phys.Rev,1955;100: 545.

[6] Kong, W. J. Lu, L. Zhu, H. W. Wei, B. Q. Wu, D. H. J. Phys. Condens Matter2005;17:1923.

DE GRUYTER OPEN

The Scientific Bulletin of VALAHIA University
MATERIALS and MECHANICS –Vol. 16 , No. 14

DOI 10.1515/bsmm-2018-0005

ANALYSIS OF INTERNAL DEFECTS APPEARED IN THE CONTINUOUS CASTING

Elena Valentina STOIAN[1], Vasile BRATU[1], Cristiana Maria ENESCU[1], Carmen Otilia RUSANESCU[2]

[1]Valahia University of Targoviste, Faculty of Materials Engineering and Mechanics,
Department of Materials Engineering, Mechatronics and Robotics
13 Aleea Sinaia Steet, Targoviste, Romania
[2]University Polytechnic, Faculty of Biotechnical Systems Engineering Bucharest, Romania

E-mail: cristiana_enescu@yahoo.com

Abstract. *The paper presents the study of internal defects resulting from the continuous casting of steels. The 50 samples were taken from a total of 20 continuously cast bits of different steel grades. The investigation of the causes of internal defects, shown on the analyzed samples, started from the assumption that the secondary metallurgy was performed correctly. The following internal defects have been evident: internal cracks (axial cracks, section cracks), central porosity and marginal punctuation impurities.*

Key words: *internal cracks, central porosity, marginal punctures, continuous casting*

1. INTRODUCTION

The economic importance of the hot sectors results from the use of processed products, represented by laminates, forged, molded, cast, sintered parts, etc. in almost all areas of social life, but especially in machine building, civil and industrial construction (bridges, dams, halls, dwellings) [1,2,3]. World trade in steels and products made in warm sectors is a barometer of the overall world economic development, as goods in this category have a wide use. In 2017, Romania's steel production increased by about 50% compared to the same period in 2010, due to the investment policy of representatives of the large steel groups that are present in Romania and have invested in the acquisition of technologies in order to obtain quality steel such as: ARCELORMITTAL, MECHEL, TMK and TENARIS.

Over the past 21 years, world steel production has almost doubled, growth is boosted by emerging and not developed countries (France, the UK now produces less than in 1989, the US, Japan and Germany stagnated, and India's production and China rose 4.5 times, 10 times).

According to the World Steel Association data, 1.4 billion tons of steel were produced worldwide in 2010, and Romania ranks 34th among producer countries (China, with 44% in world production, followed by Japan with 7.8%, the United States with 5.7% and Russia with 4.7.Continuous casting of metals, especially steel, is a process increasingly used nationally and globally due to the major advantages it has compared to conventional casting. Thus, the modernization and optimization of the continuous casting process and equipment, including the extraction facilities for semi-finished products, is an intense concern of the field research .[3,4,5,6,7]. So the development of all industrial branches has led to a growing demand for steel, which has led the steel industry to develop a lot and to seek solutions for modernization, as well as for the production of high quality and precision products.

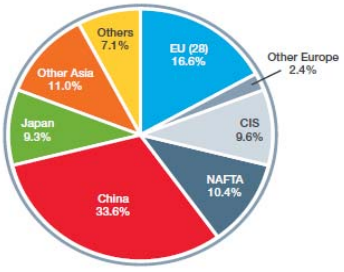

Figure 1. Continuous cast steel production in 2006

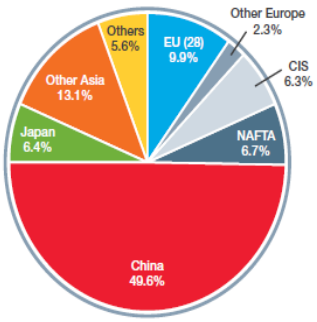

Figure 2. Continuous cast steel production in 2016

Following the continuous cast steel production from 2006 to 2016, worldwide we find that the largest quantity of continuous cast steel is provided by China, as

shown in figures 1 and 2. China's share of the world's production is about 50%, and the quantity of steadily cast steel in the EU countries drops from 16.6% to 9.9%.

The upgrading action of the global steel industry is aimed at introducing or expanding more efficient, environmentally-friendly or low-emission technologies, such as the continuous casting process [7,8, 9,10].

The main factors that accelerated the expansion of modern continuous casting technology can be synthesized as follows:

1. Making products that meet the demands of top techniques (cosmonaut, electronics, military, nuclear, etc.).
2. Environmental protection and disruption of biological cycles.
3. Increasing labor productivity.
4. Reduce material expenses.
5. Adaptation of the quality criteria to the increased demands of the users of the products.

In the fully integrated modern steel manufacturing processes, the continuous casting of steel semifinished steel is gaining ground in classical ingot molding due to dimensional precision, surface quality, superior energy recovery, precision of chemical composition control, and the amount of inclusions non-metallic, which results in a material purity of only a few ppm. Through continuous casting process carbon and alloy steels are cast, electrotechnical steels, corrosion-resistant steels etc.

There are still problems, without which it is not possible to achieve the efficient casting of different grades of steel through this process [1, 8, 10]. One of these problems is to ensure the superior quality of continuously molded semifinished products, related to axial segregation, porosity and so-called V-shaped segregation [10-13].

Other problems are related to the appearance of surface defects, internal defects, predominantly determined by suf-fers and non-metallic inclusions. Compared to classical cast ingots, for continuous casting of the same steel brand, the total amount of non-metallic inclusions in continuous castings is usually higher.

2. DEFECTS APPEARING ON CONTINUOUS TURNING

Internal cracks occur in areas with low mechanical strength of the material, under the individual or combined action of mechanical, thermal and phase transformations. The greatest likelihood of internal cracks is in the liquidus solidus transition area. These are generated by exceeding the limit values of plating or elongation, during metal stress due to the fluorescence pressure of the column of liquids, as well as the drive and straightening forces in the extraction-straightening unit.

In the free spaces created thus penetrates the liquid metal enriched in segregation elements, forming interdentritic zones of composition different from the rest of the metallic mass.

The crack susceptibility increases with the increase in the content of the elements: C, Mn, Sn, P, S. Increasing the carbon content of the steel, especially over 0.7% increases also the risk of cracking, increasing the difficulty of casting. In the carbon content of 0.17-0.25% the decrease of the elongation causes a tendency of cracking [1, 7, 8, 10].

Particularities of elaboration: insufficient boiling or decarburization beyond the indicated limits as well as molding characteristics such as: the degree of turbulence of the steel jet in the crystallizer, influence the formation of the cracks [1, 4, 10, 14].

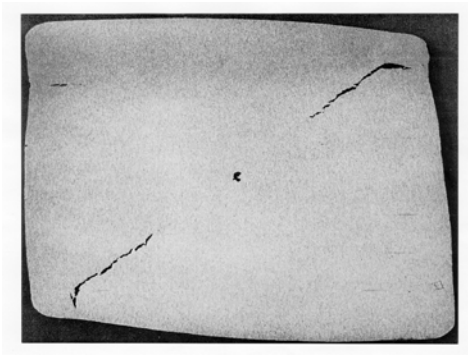

Figure 3. Cracks on diagonal

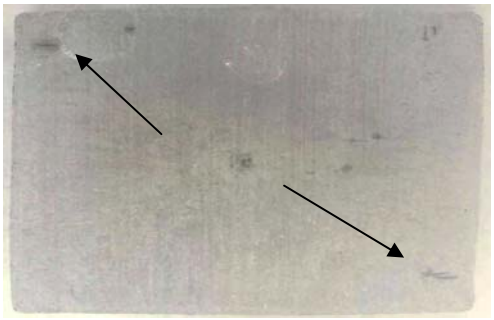

Figure 4. Surface cracks

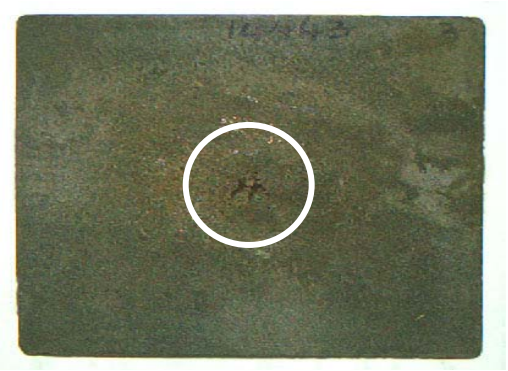

Figure 5. Central cracks

The origin of retardation and porosity is in the solidification process. Their occurrence is caused by a too sharp angle of the solidification cone due to excessive casting speed and too intense cooling. By reducing the casting speed the porosity is reduced and

dispersed.[10] Retaining and porosity depend on: steel composition, casting speed, overheating of steel and the size of the blank [1, 10].

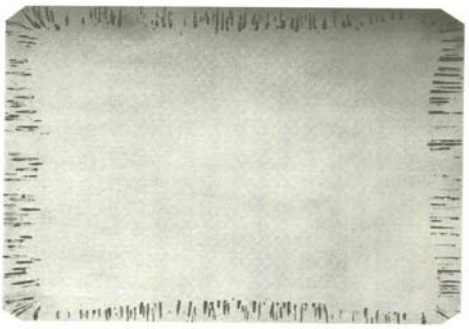

Figure 6. Retaining

3. EXPERIMENTAL PART

Sampling was done from continuous casting billets under normal conditions, ie excluding the bits from the beginning and end of the batch. Samples of 20 continuously shielded castings were sampled over a calendar month of the following steel grades listed in Table 1:

Table 1. Steel brands analyzed

Brands	No. sample	No. charge
AH36	11	4
BST500S	9	3
S235J2	3	1
S355J2	6	2
C40E	2	2
C45E	2	1
45	2	2
20MNV6	3	1
18HGT	3	1
40H	6	2
40CR10	3	1

The investigation of the causes of internal defects, shown on the analyzed samples, started from the assumption that the secondary metallurgy was performed correctly.

After analyzing the 50 samples, the following internal defects were highlighted: internal cracks (axial cracks, cracks per section), central porosities and marginal punctual impurities.
The central porosity can form if there is insufficient liquid to feed the contraction that occurs during solidification. Chances of occurrence are increased by high casting velocity and intense secondary cooling which can generate equiaxial grain crystals at the center of the billet before the column crystal growth front.

For the ease of highlighting internal defects in figures and graphics, the 20 batches were denoted in letters from A to U as shown in Figure 7.

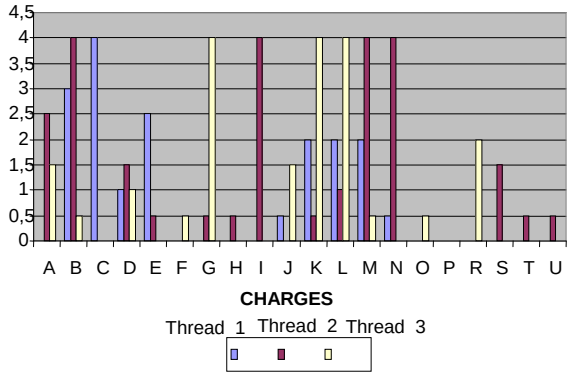

Figure 7. How to allocate central porosity for the 20 charges

It is noted, according to figure 7, that after continuous casting, thread 2 and yarn 3 have maximum points.

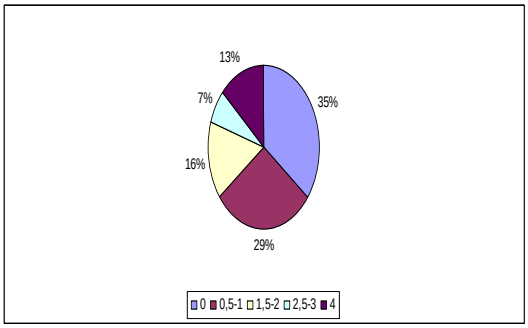

Figure 8. The central porosity score for the 50 analyzed samples

According to figure 8, it is found that for 35% of the analitic balls the score is zero and for the remaining 65% the central porosity score was between 0.5 and 4. The main cause of IPM (Marginal Punctuation Impurities) is reoxidation. Anywhere in the system there is the possibility of reoxidation, there will be a macroinclusion.

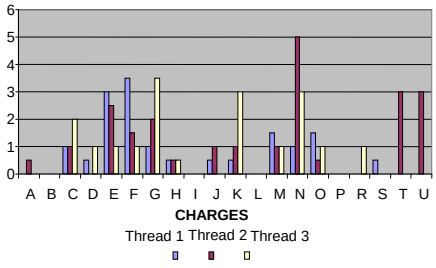

Figure 9. PM analysis for the 20 charges

Figure 9 shows how marginal point impurities are distributed over the 20 batches analyzed where it is found that the largest share of these defects is at thread 2.

From Chart 10 it is found that 28% of the analyzed samples have no impurities and the remaining up to 100% have this type of defect with scores ranging from 0.5 to 4.

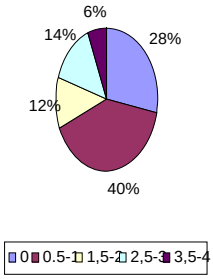

Figure 10. IPM score for the 50 samples analyzed

Between the casting pot and the distributor, the steel protection is made with a submerged tube. There are cases where the opening of the casting pot requires the use of oxygen when the tube is removed and there is a risk of reoxidation.

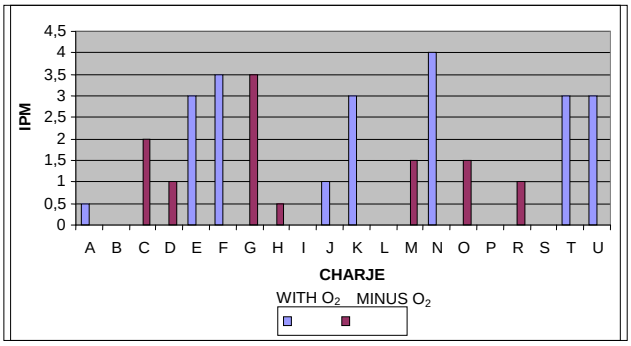

Figure 11. How to open the pouring chamber

Figure 11 shows that the emergence of IPMs is most common in oxygen-exposed charges.

The steel protection between the distributor and the crystallizer is achieved by means of immersion tubes and crystalliser dusts.

The immersion tubes are made of graphite-based composite materials with a protective insert.

This insert contains ZrO, which has a melting temperature of 2700° C and is not wetted by slag.
During casting, erosion of refractory materials in the distributor, including protective tubes that cause the production of inclusions in steel, occurs.

The durability of these tubes is relatively short of a maximum of 10 castings.
Another cause for the emergence of IPMs is the entrainment of coating dusts from the distributor and the crystalliser dusts into the liquid steel due to their incorrect immersion and due to the eddy currents.

4. CONCLUSIONS

After the research of the causes of the internal defects encountered in the analyzed samples, some actions are required to diminish the quantity of these defects and increase the productivity.

Internal cracks and central porosity do not pose any problems because the hot plastic deformation process disappears, but non-metallic inclusions cause great damage to finished products.

The injection of casting powder into liquid steel when it is cast at high speed is a problem with respect to the number of non-metallic inclusions in the continuous casting, electromagnetic stirrers, and the electromagnetic braking process as a solution to reduce the number of inclusions.

The use of primary electromagnetic agitators reduces the content of non-metallic inclusions, and the use of final electromagnetic stirrers (located below the secondary cooling zone) reduces the occurrence of central porosity.

The implementation of electromagnetic braking technology would lead to some advantages such as:

- favoring the exit of the meniscus surface of the Ar bubbles and non-metallic inclusions, which can be captured in the casting powders,
- preventing the casting of the casting powder in the liquid steel by stabilizing the fluctuating level of the steel in the crystallizer.
- stabilizing the meniscus of the liquid steel in the crystallizer,
- increasing the temperature of the steel under the meniscus,
-controlling the flow of molten metal through the immersed tube by reducing the flow rate,
- uniformization of the melt slag thickness as a result of the reduction of the meniscus movement speed.

REFERENCES:

[1] O. Florea s.a., Teoria Proceselor Metalurgice, Ediția a-2-a, Editura Didactică şi Pedagogică Bucureşti, 1984.

[2] C.O. Rusănescu, M. Rusănescu, F.V. Anghelina, V Bratu, The influence of the micro-alloying elements on physical and structural characteristics of the some steel destined for manufacturing the oil pipes, Romanian Reports in Physics, Vol.68,no.1, 278-293, 2016

[3] J. H. Chesters, Refractories for iron & steelmaking, The Metals Society, London 1974, pp. 406-407.

[4] V. Bratu, Metode experimentale şi procedee privind îmbunătățirea calității semifabricatelor turnate continuu, Editura Ştiințifică F.M.R., Bucureşti, 2003.

[5] C.O. Rusănescu, M.Rusănescu, Traian Iordanescu, V. Anghelina, Mathematical relation ships between alloying elements and technological deformability indexes, Journal of optoelectronics and advanced materials, Vol.15, No.7-8, 718-723, 2013.

[6] E. Popa, T. Heput, E. Ardelean, A. Socalici, Identifying the main defects appeared in the structure of continuous blanks, International journal of systems applications, engineering & development Issue 1, Volume 6, 2012.

[7] N. Oargă, T. Heput, E. Ardelean, E. Popa, Study on internal defects continuously cast blanks, Annals of Faculty of Engineering from Hunedoara, tom III, fasc.1, 2001.

[8] E. Ardelean, M. Ardelean, A. Socalici, T. Heput, Simulation of continuous cast steel product solidification,Rev. Metal.Madrid 43, 181– 187, 2007.

[9] V. Bratu, I.N. Popescu, The Mathematical Model Applied to Solidify and Segregation of Ledeburite Tool Steel Ingots, Scientific Bulletin of Valahia University-Materials and Mechanics 15 (12), 28-31, 2017.

[10] V.Vrabie, C.Bratu, I.Chira, Tehnologia Elaborării şi Turnării Oţelului, Editura Didactică şi Pedagogică Bucureşti, 1979.

[11] S.Mckay, N.S. Hunter, A.S. Normanton, V.Ludlow, P.N. Hewitt, B.Harris, Powder evaluation for continuous casting , Ironmaking and Steelmaking 2002, vol. 29, Nr. 3, p. 189.

[12] K. Kim, H. N. Han, T. Yeo, Y. Lee, K. H. Oh, D. N. Lee, Analysis of surface and internal cracks in continuously cast beam blank, Ironmaking and Steelmaking 1991 Vol. 24 NO. 3 p.249

[13] Y. Tanizawa, Factors of decarburation in continuous casting of ulc steels and the remedies. Camp Isij, vol. 4, 1991, p. 257.

[14] Ghe. Ioniță, E.V.Stoian, Heat flow in solidification, Buletinul Universității Petrol-Gaze din Ploieşti,ISSN 1224-8495, 87-92, 2006.

[15] K.Koyama, Y.Nagano, K.Nagano, T.Nagano, Physico-chemical properties of powders used for continuous casting, N.S.T.R. nr. 34, July 1987.

[16] Yu, X., Pomfret, R. J., Coley, K. S. Dissolving alumina in the crystalliser powder , Metallurgical and Materials Transaction B , vol. 28, 1997.

DE GRUYTER OPEN

The Scientific Bulletin of VALAHIA University
MATERIALS and MECHANICS –Vol. 16, No. 14

DOI 10.1515/bsmm-2018-0006

COMPACTION BEHAVIOUR MODELLING OF METAL-CERAMIC POWDER MIXTURES. A REVIEW

Ileana Nicoleta POPESCU [1], Ruxandra VIDU [2,*]

[1]Valahia University of Targoviste, Faculty of Materials Engineering and Mechanics, Str. Aleea Sinaia, No. 13, Targoviste, Romania
[2] California Solar Energy Collaborative, University of California, Davis, 1, Shields Ave, Davis, USA

E-mail: pinicoleta24@yahoo.com, *rvidu@ucdavis.edu

Abstract. *Powder mixtures compaction behavior can be quantitatively expressed by densification equations that describe the relationship between densities – applied pressure during the compaction stages, using correction factors. The modelling of one phase (metal/ceramic) powders or two-phase metal-ceramic powder composites was studied by many researchers, using the most commonly compression equations (Balshin, Heckel, Cooper and Eaton, Kawakita and Lüdde) or relative new ones (Panelli - Ambrózio Filho, Castagnet-Falcão- Leal Neto, Ge Rong-de, Parilák and Dudrová, Gerdemann and Jablonski. Also, for a better understanding of the consolidation process by compressing powder blends and for better prediction of compaction behavior, it's necessary the modeling and simulation of the powder pressing process by computer numerical simulation. In this paper are presented the effect of ceramic particles additions in metallic matrix on the compressibility of composites made by P/M route, taking into account (a) the some of above mentioned powder compression equations and also (b) the compaction behavior modeling through finite element method (FEM) and discrete element modeling (DEM) or combined finite/ discrete element (FE/DE) method.*

Keywords: *Powder compression equations, Numerical simulation,Compaction Modeling, Metal-Ceramic Powders, Composites*

1 INTRODUCTION

Powder compaction equations are essentially mathematical descriptions of the compaction process that express the theoretical and experimental relationships between strength - density, density – applied pressure of the consolidated material, their pressing conditions and the different properties of the powders (chemical composition, shape, average size and granulometric distribution, apparent / tap density, porosity, specific surface, compressibility and fluidity) using correction factors [1-17]. The interest in powder compaction equations was initially motivated by a practical problem—the need to be able to predict the compaction pressures to achieve a certain density, in order to provide the optimum required properties to the green compact and implicit to the final product. Nowadays, numerous researchers try to find and /or validate a 'simple but adequate' mathematical description of experimentally observed compaction curves and to determine and explain quantitatively the predominant mechanisms of powders' densification, such as the compaction stages [4-23]. Over time, a number of empirical equations have been proposed to characterize compression behaviours and densification mechanisms of one phase: metal (iron, steel, electrolytic Cu, spherical Al, nickel, Mo, Ti, W, atomized Pb and Sn, Ni–Fe-based alloy etc.) powders, ceramic (graphite, Al_2O_3, spherical glass, WC, TiC, NbC etc.) powders or two-phase metal-ceramic powders: Al and Cu alloys with ceramic (Al_2O_3, SiC, TiO_2) powders, Steel+NbC, Fe-Cu-(SiC-diamnante), TiH_2-SS316L (nano) composite powders [1-23].

2 COMPACTION BEHAVIOUR MODELLING

2.1. Powder Compression Equations

The most common models of powder compaction were developed by Shapiro – Kolthoff and Konopicky (1947-1948) [15, 17], Balshin (1949) [5,15, 19] , Heckel (1961) [5,15,19] Cooper-Eaton (1962). [3,6,12,15,17], Kawakita and Lüdde (1971) [5,15,19].

Later, Ge Rong-de [5,8,10,17] (1991), Panelli and Ambrossinni - Filho (1998) [4,5,7,17], Parilák and Dudrová (2004) [11,14,18], Castagnet & Leal Neto 2008 [8] Gerdemann and Jablonski (2011) [9] have contributed to the old equations (for instance evaluate the validity and applicability of them to the new powder mixture, at wide range of pressure, composition of mixture, average sizes, etc.) or developed new ones**.**
In Table 1 are shown the compression equations that describe the compaction behaviours and densification mechanisms of one phase (metal or ceramic) powders or two-phase metal-ceramic powder composites of all above mentioned researchers.

In most used mathematical equations (Shapiro–Kolthoff and Konopicky, Bal'shin, Heckel) and also in the new equations of Ge Rong-de, Panelli and Ambrossinni-Filho, Parilák and Dudrová, Castagnet & Leal Neto or Gerdemann and Jablonski, the *Ai* (i = 1-3, 6-9) parameter is used to demonstrate the plastic deformation capacity of the powders or powder mixture and corresponds to the inclination angle of the compressibility curve (the higher *Ai*, the greater the deformation).

Table 1. Powder compression equations that describe the compaction behaviours and densification mechanisms of one phase (metal or ceramic) powders or two-phase metal-ceramic powder composites

Authors	*Equation(s)*	*Remarks*
Shapiro – Kolthoff and Konopicky	$\ln\left(\frac{1}{1-D}\right) = kP + \ln\left(\frac{1}{1-D_0}\right)$ (1) For simplification we note: $k = A_1$ and $\ln\left(\frac{1}{1-D_0}\right) = B_1$ Result: $\ln\left(\frac{1}{1-D}\right) = A_1P + B_1$ (2)	*D*- relative density at pressure P; D_0 –relative density at "zero pressure"; A_1 *(k)* and B_1 are constants ; The Shapiro and Kolthoff made the following assumption: the powder mass could be treated as if it were a solid body subject to isostatic compression forces. Konopicky investigated materials: Iron, steel, magnetite, quartz and magnesite powders; Shapiro and Kolthoff investigated materials are: silver bromide powders.
Bal'shin	$\frac{1}{D} = A_2 \ln P + B_2$ (3)	*D*- the relative density of green compact ; *P*- applied pressure; A_2 and B_2 are constants; Balshin investigated materials: metallic (electrolytic copper, spherical aluminum powder) and ceramic powders;
Heckel	$\ln\left(\frac{1}{1-D}\right) = kP + \ln\left(\frac{1}{1-D_0}\right) + B$ (4) Or $\ln\left(\frac{1}{1-D}\right) = A_3P + B_3 + B$ (5) Result: $\ln\left(\frac{1}{1-D}\right) = A_3P + B_3$ at B=0 (6) Where: A_3 or $k = 2.08\times10^{-6} + 0.320\frac{1}{\sigma_0}$ (7) A_3 or $k \cong \frac{1}{3\cdot\sigma_0}$ (8)	*D*- relative density at pressure *P*; D_0 –relative density at "zero pressure", or relative apparent density of the powder; *(1-D)* is the pore fraction. According with Heckel [1], "zero-pressure" densities means the densities measured after the compacts are removed from the die. After experimental observations, Heckel have shown that he constant *k* (or A_3) could be related to the nominal yield strength σ_0 of the powdered metal, represented quantitatively in Eqs. (7) and (8). The constant B_3, which is always somewhat larger than *ln(1/l-Do)* represents the degree of packing *achieved at low pressures* (low limit at linearity) as a result of rearrangement processes before appreciable amounts of interparticle bonding take place [1]. In addition, it was found that the constant *B* from Eq. (6) is a function of the size and shape of the powder particles [1]; *B* decreases as the particle size decreases and as the shape of the particles becomes more spherical. For spherical particles, *B* is approximately zero (Eq.6). Heckel investigated metallic materials as (iron, steel, nickel, tungsten) and ceramic (graphite) powders [5,15,19];
Cooper-Eaton	$\frac{D-D_0}{1-D_0} = B_4\exp\left(\frac{-A_4}{P}\right) + B'_4\left(\frac{-A'_4}{P}\right)$ (9) or $\overset{*}{V} = \frac{V_0-V}{V_0-Vs} = =a_1\exp\left(\frac{-k_1}{P}\right) + a_2\left(\frac{-k_2}{P}\right)$ (10)	*D*- relative density at applied presure *P*; D_0 –relative density at "zero pressure"; $\overset{*}{V}$ - fractional compaction ; *V*- volume of compact at pressure P; V_0 – volume of compact at "zero pressure"; V_s- void-free solid material volume;A_4, B_4, A'_4, B'_4 (a_1, a_2, k_1, k_2) are Cooper-Eaton model constants; B_4 and B'_4 represent dimensionless coefficients indicating the fraction of theoretical compaction that would be achieved at infinite pressure by each mechanism. Cooper-Eaton investigated materials are ceramic (Al_2O_3) powders [3,6,12,15,17].
Kawakita and Lüdde	$\frac{P}{C} = \frac{1}{ab} + \frac{P}{a}$ (11) $C = \frac{V_0-V}{V_0} = 1-\frac{D_0}{D} = \frac{abP}{1+bP}$ (12) $a = C_\infty = \frac{V_0-V_\infty}{V_0}$ (13) $\frac{D}{D-D_o} = \frac{A_5}{P} + B_5$ (14) Where: $A_5 = \frac{1}{ab}$; $B_5 = \frac{1}{a}$ (15)	*C* – the reduction of volume by compression; *P*-applied pressure; V_0- the initial apparent volume; *V*- the volume under the applied pressure *P;* *D*- relative density at presure *P*; D_0 –relative apparent density of the powder; *a, b* - Kawakita-Lüdde model constants related to characteristic of the powder . The constant „a" corresponds to the limit in value of the relative reduction of the volume by compression and is equal to the initial porosity of a powdered mass (Eq. 13), where V_∞ is the net volume of the powder. The „b" constant shoud be equal to the reciprocal of the pressure when the value, C, reaches one-half of the limiting value (C=$C_\infty/2$); A_5, B_5-constants (Eqs. 15 , 12) can be rewritten as (Eq. 14). The Kawakita's equation has been shown to give an excellent fit over the widest range of pressures. The Kawakita and Lüdde Eq. is widely applicable for metallic, cerramic (i.e. spherical glass), composites and medical powders in the fields of powder metallurgy and pharmaceutics [3,5,15].

Table 1 (continued)

Ge Rong-de	$\log\left[\ln\frac{1-D_0}{1-D}\right] = A_6 \log P + B_6$ (16) For $D_0=0$, result the simplified rel.: $\log\left[\ln\frac{1}{1-D}\right] = A_6 \log P + B_6$ (17)	D- relative density at pressure P; D_0 –relative apparent density of the powder; The coefficients A_6 and B_6 are constants and represent, the fractional dominance of a densification mechanism. Ge considered that D_0 approached zero when total pressure reached zero. Ge investigated materials: metallic powders (Atomized Pb and Sn, Electrolytic Cu, Stainless steel), ceramic powders (WC, TiC) [5, 8, 10, 17].
Panelli and Ambrozio-Filho	$\ln\left(\frac{1}{1-D}\right) = A_7\sqrt{P} + B_7$ (18) Where $B_7 = \ln\left(\frac{1}{1-D_0}\right)$	D- relative density at pressure P; D_0 –relative density at "zero pressure"; A_7, B_7-constants; The constant A_7 stands for plastic deformation capacity and B_7 expresses the density in the absence of pressure. Panelli and Ambrozio-Filho are investigated the following materials: metallic (Pb, Sn, Cu, Mo, steel AISI M2 type), ceramic (TiC, NbC , Al_2O_3) and composite (AISI M2+ 10%NbC) powders.
Parilák and Dudrová	$\ln\left(\ln\frac{1-D_0}{1-D}\right) = A_8 \ln P - \ln B_8$ (19)	D- relative density at pressure P; D_0 –apparent density of the powder; A_8, B_8-constants; The constant A_8 is related to the capacity of powder particles to undergo plastic deformation, the constant B_8 is related to the geometry of particles. Parilák and Dudrová investigated metal powder as Ni–Fe-based alloy (permalloy) [11, 14, 18].
Castagnet & Leal Neto	$\ln\left(\frac{1}{1-D}\right) = A_9 P^{0.6} + B_9$ (20)	D- relative density at pressure P; A_9, B_9-constants Castagnet & Leal Neto investigated metal powders: Niobium and aluminium powder mixtures [8].
Gerdemann and Jablonski	$D = D_0 + A_{10}(1-e^{-aP}) + B_{10}(1-e^{-bP})$ (21)	D- relative density at pressure P; D_0 –the initial density, A_{10} and B_{10} - parameters that reflect the relative contribution of powder rearrangement and work hardening mechanisms to densification; a and b – exponents that reflect how much pressure P is required to bring each mechanism to completion. The maximum density achievable by compaction alone, D_∞ is the sum of D_0, A and B. Gerdemann and Jablonski invetigated materials are sponge Ti powders, TiH2 powders, Ti 6 4 alloy powders [9].

And the parameter Bi (i = 1-3, 6-9) can be used to calculate the relative density of the powder at" zero pressure" (Do) or at lowest pressure applied and corresponds to the intersection of the compressibility curve with the ordinate axis.
There is an imprecision inherent in parameter B_i because of rearrangement of the powders inside the matrix at the beginning of compaction.

However, considering that this rearrangement represents only a small part of the total densification, the parameter B_i gives a good approximation of the initial bulk density.
The equation of Bal'shin [5,15,19] in logarithmic form expresses the dependence between relative density and applied pressure (Eq. 3).

Konopicky-Saphiro's equation, as well as the Heckel equation, are mainly used for metallic powders. These are derived from a differential equation expressing the proportionality between the relative density variations with pressure and porosity Eqs. (1), (2), (4)-(6).

The Kawakita equation [5,15,19] is a commonly used expression to linearize compression data, both from continuous compression experiments and from tapping ones. The basis for the Kawakita equation is the assumption that a powder held in a confined space and subjected to an applied force is a system in equilibrium at all stages of compression, so the product of the increased applied pressure and the volume reduction is constant.
The linear relationship (Eq. 11) between P/C and P allows the constants „a" and „b" to be evaluated graphically. Thus, by plotting the curves $P / C = f(P)$, we can get the slope value „*1 /a,*" and we put the condition $P = 0$ we obtain the value of "*1 /ab*" on the P/C axis.
Cooper and Eaton introduced a new concept based upon the idea that the size of the pores relative to the size of the surrounding particles determines the kind of pore closing mechanisms [6].

For the sake of simplicity they considered two broad classes of compaction mechanisms; the filling of large holes by particle sliding (involving only slight particle modification by fracture or plastic deformation) and the filling of small holes by plastic flow or fragmentation [6].

In the equations (16), (17) (18) and (19) Ge Rong –de, Panelli-Fillo and Parilák and Dudrová, for quantification of densification behaviour of the mixture powders, parameters A_6, A_7 and A_8 express the ability of metallic powders to plastic deformation and B_6 B_7 and B_8

coefficients are associated with geometry properties of powder particles.

We observed a particularity of Ge Rong-de and Parilák and Dudrová models that used both a double loghartimic operator for the left part of the equations (16) and (17). These means that it is necessary to choose $D \in (0,1)$ the relative density at pressure *P*. In the paper of Cardei and Gageanu [24] they made a crytical analysis of the Eq. (17) where specify that $D=1$ means that the density of the compacted powders would be equal to the density of the powders. And for $D<1$, make imposible the hypothesis that applied pressure is equal with the "zero pressure" [24].
Castagnet & Leal Neto in Eq. (20) has proposed a version close to that of the Panelli and Ambrozio-Filho model.

The Gerdemann and Jablonski model of the metal (Ti) powders, expressed by the equation (21) they have taken into account that constant coefficients A_{10} and B_{10} reflecting the relative contribution on powder rearrangement and work hardening mechanism to densification. On basis of Gerdemann and Jablonski Eq. (21) Machaka and H. K. Chikwanda [21] studied Ti powders (sponge Ti, CP TiH2, Grade 2 CP Ti) and also TiH_2-SS316L nanocomposite powders.

All these equations from Table (1) expressed empirical formulas that descriebed the compaction phenomenon for the powders. Another approach is that using modeling and simulation assisted by the computer, for a better undestanding and prediction of compaction behavoiur of powder mixtures.

2.2. Computer numerical simulation

Compared to the physical characterization of powders cold pressing, their numerical characterization has the advantage of quantifying the local distribution of density, the stress distribution, and powder flow behavior in the compacted powders, rearrangement and deformation of individual particles, pore filling, during and after compaction [25-34].

The most used techniques in numerical simulation of pressing are: (i) finite element method (FEM), at macro scale [25, 26] , when the compact is considered to be a continuous body (mechanical continuum [27, 28, 29]); (ii) the discrete element method (DEM) [26,29-33], at the micro scale of the particles (iii) macro multi-particle FEM (MPFEM) [29, 33, 34], or (iv) combined finite/ discrete element (FE/DE) method [35, 36, 37].

In *the FEM simulations*, powders can be seen as a mechanical continuum, wher the size of powder particles is several orders smaller than compacted powders or compaction die[26]. The FEM analysis solve the balance laws (conservation of mass, momentum and energy) and constitutive laws (stress-strain and friction laws, which describe the deformation of powders under applied pressure)[26]. In FEM analysis of powder compaction, it is necessary to know, besides constitutive equations, the initial conditions of the powders, the friction interaction between powder and die/punches, the geometry of the tooling, the pressing process parameters and the particularity of them [26].

Based on the experimental data of compaction of mixed—soft and hard—metal powders under cold compaction Kim *et al.* [38] proposed corresponding numerical simulations. The proposed model is useful for theoretical prediction of densification of composite powders at initial stage of cold isostatic pressing. Also, by implementing the constitutive equations in finite element programs (eg ABAQUS, PLAXIS etc.), it is possible to compare the experimental data and / or experimental results of other authors to densification of the powder mixture [39, 40].

The constitutive models developed in the field of rock and soil mechanics, such as CAM-CLAY , Drucker-Prager and other model, have been also adapted for modelling of powder compaction[26, 27] . In these models, the yield surface is described by a shear failure line and a compaction surface (Fig. 1).

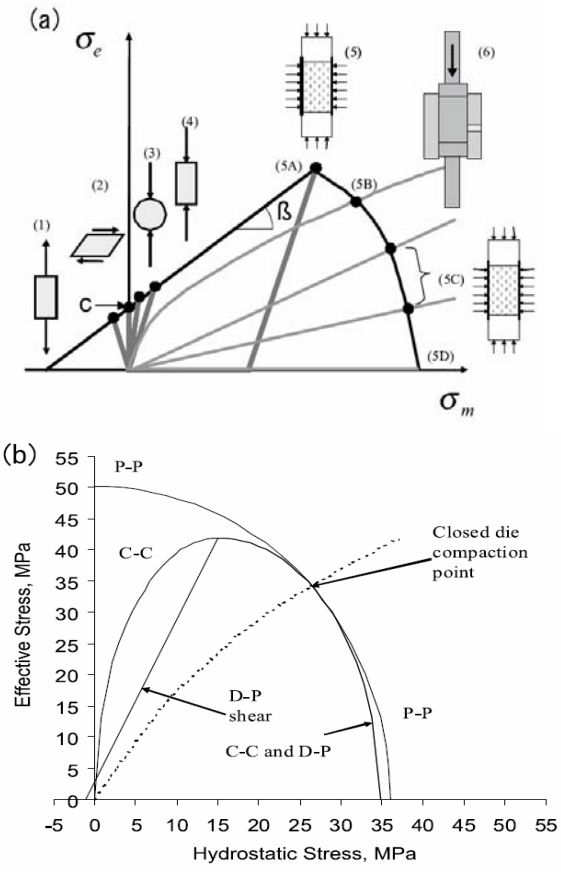

Figure 1. Constitutive models for powder compaction : a) experimental procedures for determining Drucker –Prager cap model parameters, and b) Yield surfaces for microcrystalline cellulose using various models calibrated on a closed-die compaction experiment[26]

In **Fig. 1 a)** was noted with (1) uniaxial tension, (2) simple shear, (3) diametrical compression, (4) uniaxial

compression, and in **Fig. 1b)** C-C is the abravion for Cam-Clay model, D-P from Drucker –Prager cap, and P-P from Porous plasticity.

The Discrete Element Method (DEM) provide a more physical description than a macroscopic model, in particular, a micromechanical modeling of the compaction and final components. In DEM model, each powder particle is modeled as a single object and the contact forces acting on each particle determine its motion by Newton's second law [41].

The DEM solves the equation of particles motion taking into account the simplified interactions between particles in contact. The particles are assumed to be rigid-plastic spheres, the contact between the particles is witout friction and the contact strength in tension and compression is considered equal [26].

Similar to the DEM simulations, *the multi-particle finit element model (MPFEM)* was used to investigate the effect of friction between particles on the macroscopic yeld response of materials, for the large deformation of particles during compaction [26, 29, 33, 34].

At *combined finite/ discrete element (FE/DE)* method [35, 36, 37], each particle is mapped with finite elements and the interaction between particles is solved using a discrete element technique [37].

We can investigate through this combined method the powders or granules with different yield stress and initial porosity and the relationship between the single-particle properties and the global compression behaviour of the granule bed [35]. It is demonstrated that the FE/DE method may shed light on the deformation and densification behaviour of individual particles , since the size and shape of each particle (granule) are continually determined as an integral part of the solution procedure, and that the method thus gives us an overview of the processes occurring during compression of granular materials [35].

3. APPLICATIONS OF COMPACTION MODELS ON DIFFERENT METAL-CERAMIC POWDER MIXTURES

3.1. Applications of Empirical Powder Compression Equations on Mixture (Composite) Powders

A literature survey on the applicability of the densification models indicates that different researchers have used different models to verify their experimental data. There are those who have fitted experimental data to a single model to capture the densification of their powders.

For example, Cazzoti et. al [4] for a better understanding of the effect of the Al_2O_3 particulate addition on the compressibility of aluminium powder alloys they applied the Panelli Ambrosio equation to linearize the compressibility curves (Fig. 2), while Alizadeh et al. used a modified Heckel equation [17].

Cazzoti observed that the compressibility depends on the powder characteristics and can be altered by hard particles addition, as in the Al MMC particulate reinforced.

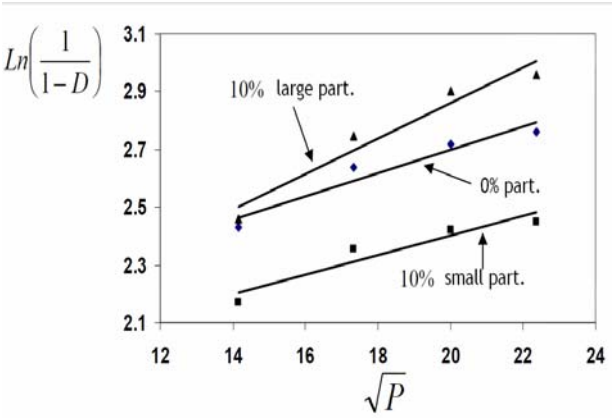

Figure 2. Compressibility curves linearized with Eq. (18) for the unreinforced Al alloys powders and the Al- 10% vol. Al_2O_3 mixture powders, for both particle sizes

Smaller particles cause a decrease in compressibility (downward movement of the curve), while larger particles cause inverse effect, at the same proportion (10%) of Al_2O_3 particles. Fig. 3 shows that larger sized alumina particles increase the A parameter when added Al_2O_3 to the metal powder alloy, and this increase is quite significant.

Already the smaller alumina particles cause a decrease of the parameter A, and this decrease is more significant for the amount of 10% Al2O3**.**

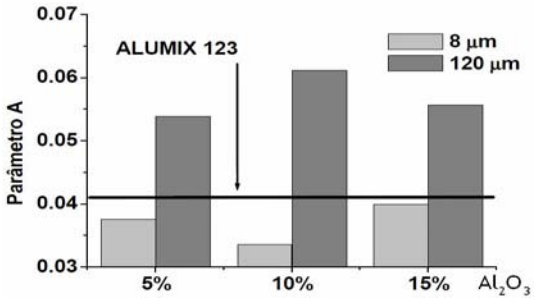

Figure 3. Parameter A for reinforced ALUMIX 123 powder of different sizes and amounts of Al2O3 [4]

But the other researchers studied metal-ceramic mixtures /composites and they compared more densification equations.

According to the densification theories of the compaction powders [22] structural transformations at compaction operations are carried out in three stages: I- Reorientation/ rearrangement and packing particulate powders; II- the elastic-plastic deformation of the metallic (soft) particles and the fragmentation of the hard particles; III - massive plastic deformation. For instance, Oliveira [7] has obtained and characaterized the Fe-Cu-Diamond system according with Bal'shin, Panelli &

Ambrosio Filho, Rong-De and Heckel densification equations and observed that (Fig. 4) a visible difference was reached between the curves of stages I and II.

The two-stage variation occurs at a pressure of 250 MPa - necessary plastic deformation of the particles and fracture at the points of contact, showing precisely the limits of each compaction stage.

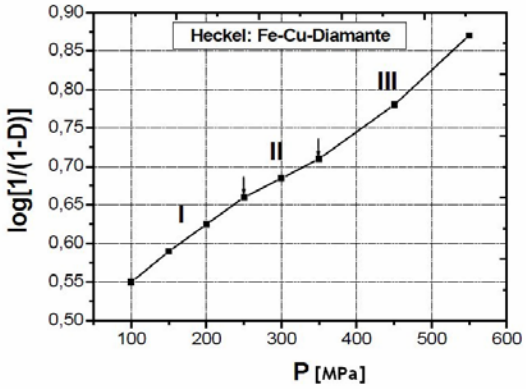

Figure 4. The densification curves of the Fe-Cu/ diamond composite according to the Heckel equation [7]

In this sense, the Heckel equation is the best alternative for the study of composite consolidation Fe-Cu / Diamnond powder mixture.

Castagnet [8], after compressibility evaluation of mechanically activated Nb-Al powders mixtures with the same above metioned compaction equations , including , Kawakita and Lüdde one, they proposed a new densifiation equation Eq. (20) that fit very well on the Nb-Al compressed, with a regerssion coefficient better than 0.9953.

Hafizpour et al. [12] compared the Heckel, Panelli-Filho, Cooper- Eaton, and Ge models and found that the highest regression coefficient was achieved by the Paneli- Filho equation, while Sivasankaran et al. [15, 20] compared, among others, the Heckel, Ge, Panelli and Ambrosio Filho, Kawakita, etc. compaction models (linear Eqs. (3), (6), (14), (17) and (18) and nonlinear ones (9) presented in Table 1) on nanocrystalline AA6061 alloy reinforced with TiO_2 composite and determined that experimental data was best fitted by the Panelli-Filho model (Fig.5). The different line types show the fitting of experimental data with different compaction equations.

Moreno and Oliver (2011) [16] working on Al-based powders reinforced with short Saffil fibres showed that the Kawakita and Konopicky equations best fitted the densification behaviour while the Panelli-Filho equation was applicable only over a limited compaction pressure range.

Also, Ghita and Popescu [19] studied the compressibility of Al–Cu/SiCp mixture powders and verify on the obtained experimental mixtures the Balshin, Heckel and Kawakita and Lüdde equations, and concuded that that Kawakita models best describe (in proportion of 99%) the compaction behaviour of Al–Cu/SiC composites, used in this experiments, the regression coefficient are better than 0.993.

Thus, using linear regression equation presented in Fig. 6 they [19] could predict (Fig. 7) the compaction behaviour for pressure higher than 500 MPa (used on their experiments) and to determine the optimum pressure for obtaining maximum densification especially for composites with larger amount of ceramic particles.

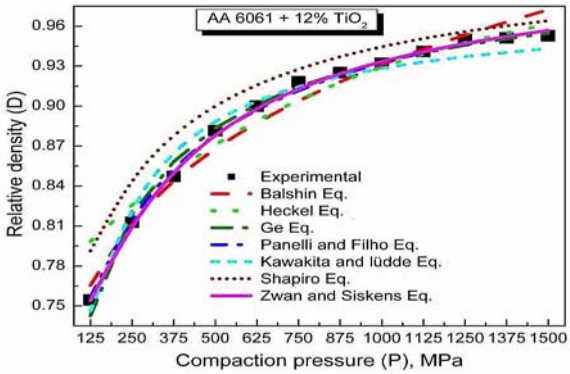

Figure 5. Compresibility of AA6061–12 wt.% TiO2 nanocomposite powder [20]

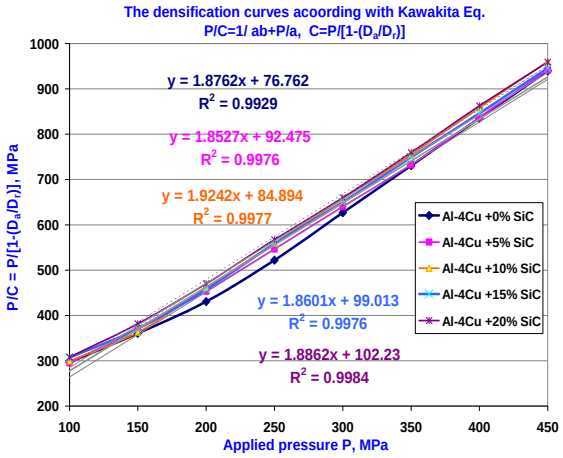

Figure 6. The obtained densification curves according with Kawakita and Lude equation (Eq. (11)[19]

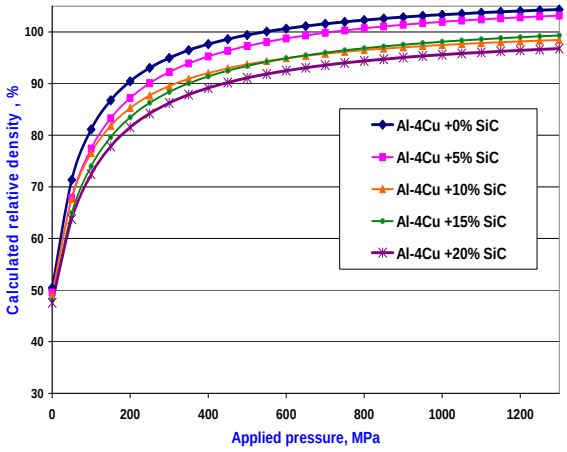

Figure 7. Densification curves according to Kawakita model, and prediction of densification, by extrapolation of Al-Cu/SiC compressibility curves on P ≥500MPa [19]

3.1. Applications of Computer Numerical Simulations on Composite Powders Compaction

In the paper of Han *et al*. [25] during compaction, the modified Shima model [42, 43] was used. The work hardening of the composite powders was incorporated as given by the Eq. (22), relation that represent the relation between uniaxial yield stress (σ_y), deviatoric stress tensor(σ_d) , hydrostatic stress (σ_m) , and materials parameters (γ, β)[25]:

$$F = \frac{1}{\gamma}\left(\frac{3}{2}\sigma^d\sigma^d + \frac{\sigma_m^2}{\beta^2}\right)^{0.5} - \sigma_y \quad (22)$$

The materials parameters are functions of relative packing density [25]:

The equivalent Young's modulus of the composite (E_c) and the yield strength of Fe - Al composite compact dense body (σ_c) was calculated by means of mixture rule [22], based on the Voigt equivalent strain assumption and Reuss equivalent stress assumption [25, 44].

During compaction, the Young's modulus and yield strength are functions of relative density. The relationship between the overall relative density ρ of the compact and the compaction pressure P is modelled and given in Fig. 8.

As can be observed in the Figure 8, the first stage the increasing of density is not when P is smaller than 20MPa, at stage II packing density fast increase, and finaly at stage III we reach the maximum density (densification) of compacted powders. Fig.8 have similar trends with those results obtained from physical experiments [45] and numerical simulations [46]

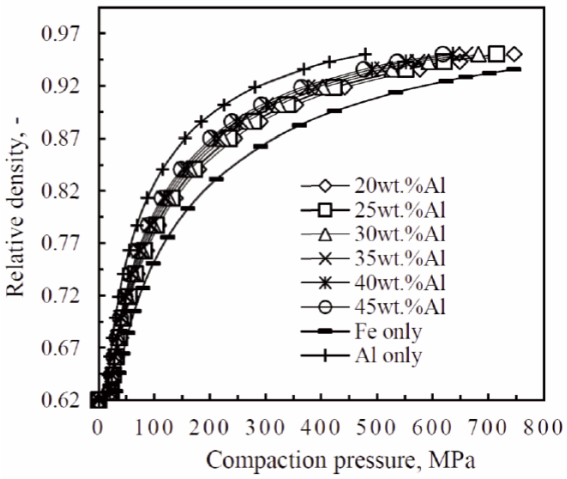

Figure 8. Fe-Al compresibility at different composition of aluminium [25]

Were also analysed by FEM method [25], the initial packing in the die, densification and ejection of compacted powders, tacking into account the uniaxial yield stress, deviatoric stress tensor and hydrostatic stress of composite powder compact.

In Fig. 9 and 10 are presented the local relative density distributions in compacted powders with different aluminium composition (X_{Al}) when P = 200 MPa , respectively local relative density under different compaction pressures.

We can obseve that the the largest or smallest local relative depending on friction area of the powders with the die and upper and lowerr punches.

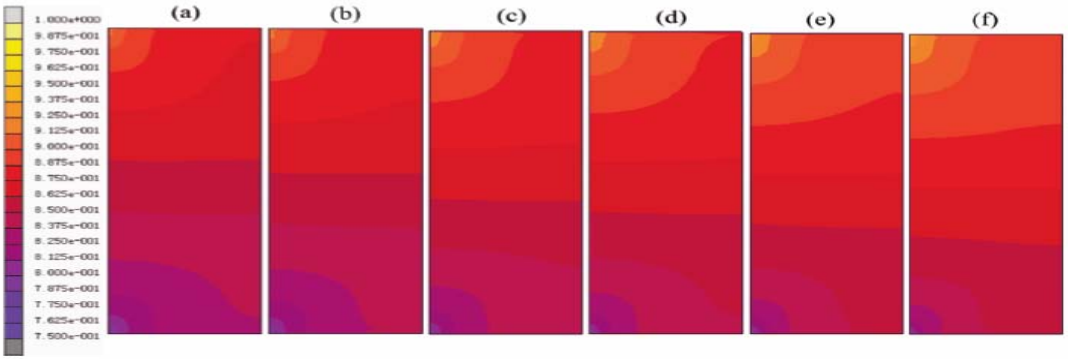

Figure 9. Distributions of local relative densities for compacted powders with various XAl when P=200MPa, where (a)-(f) for X_{Al}=20wt.%, 25wt.%, 30wt.%, 35wt.%, 40wt.%, 45wt.%, respectively [25]

Huang *et al*. [34] studyed by multi-particle finite element method (MPFEM), the 2D compaction of binary Al/SiC composite powders, by combination the characteristics of traditional FEM and DEM [35, 36, 37].

They analysed the influences of compaction pressure, the size ratio of binary particles (R_{Al}/R_{SiC}), the volume of hard particles (SiC%), the friction coefficient between particle, and initial packing structures on the densification processes of Al/SiC binary random structures [34].

For this purpose, was chosen a random binary packing structures with different proportion of SiC particles as the target to analyze their compaction processes when $R_{Al}/R_{SiC} = 2$.

They have shown that not only the processing parameters (increasing pressing) determines the increasing of densification, but also determines the diminishing size of the SiC particles, in the aluminium powder.

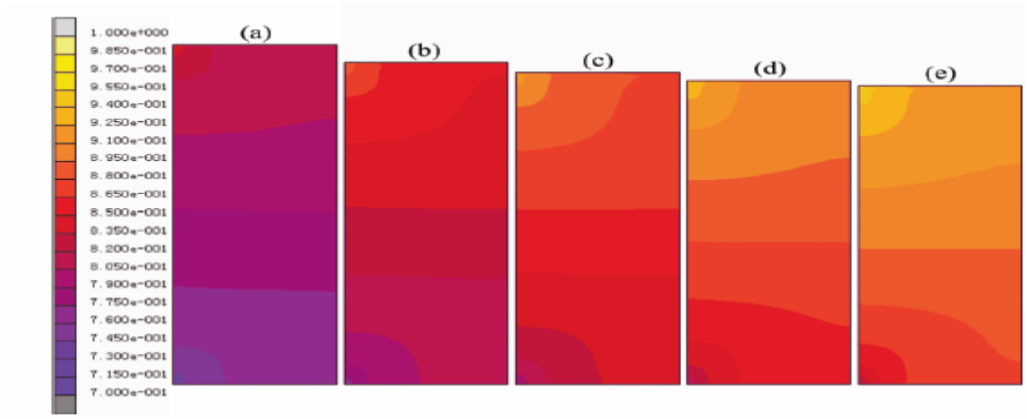

Figure 10. Relative density distributions at different applied pressures when XAl=25wt.%, where (a)-(e) correspond to P=100MPa, 150MPa, 200MPa, 250MPa, and 300MPa, respectively [25]

The results show that the densification process and the properties of the compacts are determined by initial powder. In addition the evolution of microstructure and stress in the compacted powders during pressing on random binary initial packing structure of Al% = 70% and $R_{Al}/R_{SiC} = 2$ is presented in Fig. 11.

In accordance with the specific stages at compacting densification, [22,46-50] in Fig. 11 is observed that with the increase of the applied pressure, large plastic deformation of the soft Al particles begins to occur, therefore, the densification of the compact is mainly due to the mass transfer of Al particles to their adjacent interstitial positions. At the final stage of the pressing, there are enclosed isolated pore formed from the SiC hard particles from the pressed powdery material. It is also noted that the higher the applied pressure, the lesser residual enclosed pores are.

Fig. 12 shows the evolution of total strain energy and local strain energy along with the densification curve, when composing binary composite powder "RAl / RSiC = 2andAl% = 90%.

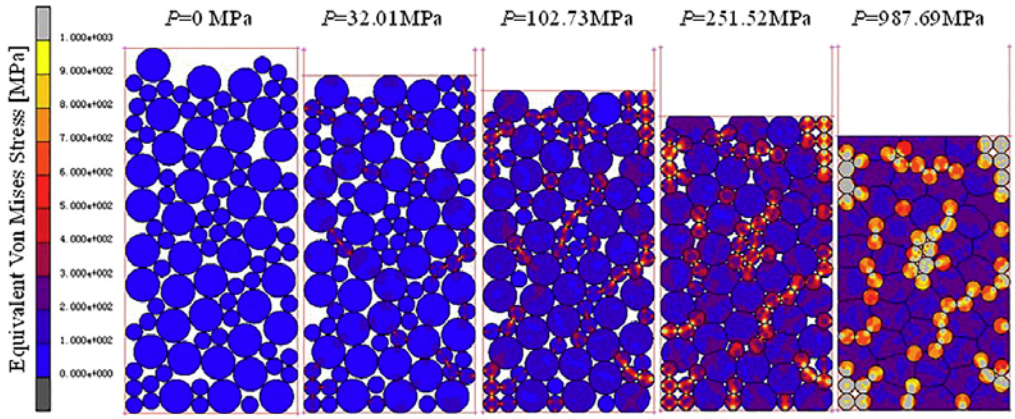

Figure 11. Compact morphology evolution at various compaction stages corresponding to internal equivalent VonMises stress distribution during compaction on randompacking of binary composite powders at70% Aland R_{Al}/R_{SiC}= 2 [34]

It is noteworthy that in the early moments of compacting there is an increased increase in density relative to a low compaction pressure in accordance with the first stage of compaction when sliding and rearranging of the particles occurs.

In this case, they didn't observe deformation but the packing structure reaches a relatively stable stage.
As a result, the total strain energy is very low (tends to zero value), as can be seen in detail in zone A of Fig 12. It can also be observed that with the increase in pressure applied, the relative density increases almost linearly with the pressure indicated in the region B.

The region B, specific to the second stage of densification of pressed materials, is the area where the elastic deformation is predominant and the total energy of the tension is low. With the increase of applied pressure, there is a large deformation of the Al particles, which results in a sudden increase in total stretching energy (region C in figure 12). At the final stage of compaction (region D in Fig. 11), specific to the third stage of pressing, the plastic deformation of Al particles reaches the maximum, which leads to a lower increase in relative density.

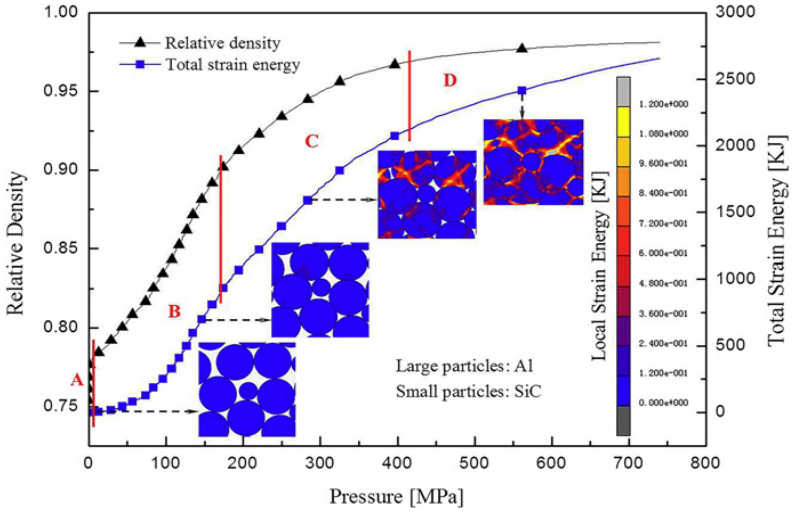

Figure 12. Evolution of relative density, total strain energy and local strain energy of Al-SiC at compression of them, when RAl/RSiC = 2 and Al%=90%[34]

4. CONCLUSIONS

In this paper we reviwed the most commonly and the new compression equations (compaction models) of one phase (metal or ceramic) powders or two-phase metal-ceramic powders (composites) based on relative density -pressure relationship during the stages of compaction.

Were presented the effect of ceramic particles additions in metal powders (in matrix) on the compressibility of composites made by P/M route, taking into account (a) the empirical powder compression equations, (b) the compaction behavior modeling through finite element method (FEM) and discrete element modeling (DEM), macro multi-particle FEM (MPFEM) or combined finite/ discrete element (FE/DE) method and advantages/disadvantage of them.

We studied also the applicability of compaction models on different metal-ceramic powder mixtures (composite powders) for better understanding the possibilities and limitations of metal-ceramic powder compaction.

REFERENCES

Journals:

[1] R. W. Heckel, A normalized density-pressure Curve for Powder Compaction Trans. Metall. Soc. AIME, 224 (1962). 1074.

[2]. I. H. Moon ,K. H. Kim, , Relationship between compacting pressure, green density, and green strength of copper powder compacts Powder Met., 27(2) (1984). 80-84.

[3] T. Çomoğlu, An Overview of Compaction Equations J. Fac. Pharm, Ankara, 36 (2) (2007)123-133.

[4] C. Cazotti, J.L.A. Oliveira, J.B. Fogagnolo, , Efeito da Adição de Partículas de Al_2O_3 sobre a Compressibilidade de Pós De Ligas De Alumínio, 17o Proceedings of CBECIMat, 15 -19 de November, Foz do Iguaçu, PR, Brasil (2006) 7452.

[5] R. Panelli, Thesis, Coordinator Prof. Dr. Ambrosio Fillo, Production of AISI M2 + 10%Vol. NbC by Mechanical Alloying, Sao Paulo, 1999.

[6] S. Mani, L.G. Tabil and S. Sokhansanj, Evaluation of compaction equations applied to four biomass species**,** Canadian Biosystems Engineering/Le génie des biosystèmes au Canada, 46(2004) 3.55-3.61.

[7]Luciano José De Oliveira, Thesis, Processing and Characterization of the Fe-Cu-Diamond System for Diamond Wire Pearls Use (in Portugues), Univ. de Estadual do Norte Fluminense, 2005.

[8] M. Castagnet, R. B. Falcão, R. M. Leal Neto, Compressibility Evaluation Of Mechanically Activated Niobium And Aluminum Powders Mixtures ,18º CBECiMat -, 24 a 28 de Novembro de 2008, Porto de Galinhas, PE, Brasil, 6785.

[9] S.J. Gerdemann and P.D. Jablonski, Compaction of Titanium Powders, . Metall. Mater. Trans. A, 42A (2011).1325-1333.

[10] Ge Rong-de, A New Powder Compaction Equation**,** The International Journal of Powder Metallurgy, 27 (3) (1991).211-214.

[11] L. Parilák, E. Dudrová, R. Bidulský, M. Kabátová, Quantification of Metal Powder Compressibility in Uniaxial Compaction, Metallurgy World Congress and Exhibition. Euro PM 2004. Vol. 1., Vienna, 17.-21.10.2004. Ed. H. Danninger, R. Ratzi, EPMA 2004, p. 593-598

[12] H. Hafizpour, A. Simchi, S. Parvizi, Analysis of the compaction behavior of Al–SiC nanocomposites using linear and non-linear compaction equations, Advanced Powder Technology 21(3) (2010) 273.

[13] A. Miskova, E. Dudrova, H. Brunckova, M. Faberova, R. Bures, Compressibility of Fe/SiO_2 Coated Composite Powders ,PM2010 World Congress - Fundamentals of Pressing, p. 39

[14] R. Bureš, M.Fáberová, Evaluation of Compressibility of Micro-Composite Systems , PM2010 World Congress – Compaction Equipment, p.81

[15]S. Sivasankaran, K. Sivaprasad, R. Narayanasamy, V. K. Iyer, Evaluation of compaction equations and prediction using adaptive neuro-fuzzy inference system on compressibility

behavior of AA 6061 100− x–x wt.% TiO 2 nanocomposites prepared by mechanical alloying, Powder Technol. 209 (1) (2011).124.

[16]. M. Moreno, C. G. Oliver, Densification of al powder and Al–Cu matrix composite (reinforced with 15% saffil short

fibres) during axial cold compaction , Powder Technol. 206(3) (2011).297.
[17] C. Machio, R. Machaka, T. Shabalala, H. K. Chikwanda, Analysis of the Cold Compaction Behaviour of TiH2-316L Nanocomposite Powder Blend Using Compaction Models, Materials Science Forum, 828-829 (2015).121.
[18] C.A. Leon, G. Rodriguez-Ortiz, E.A. Aguilar-Reyes, Cold compaction of metal–ceramic powders in the preparation of copper base hybrid materials, Materials Science and Engineering A 526 (2009).106.-
[19] C. Ghiță, I.N. Popescu, Experimental research and modelling of compaction behaviour of Al based composite with SiC particles, Comp Mater Sci, 64 (2012) 136-140.
[20] S.Sivasankaran, PhD Thesis, Coordinator Prof. Dr. R.Narayanasamy Study on Synthesis, Characterization and Workability behavior of nanocrystalline AA6061 alloy reinforced with TiO2 Composite prepared by Mechanical alloying, NIT,Tiruchirappalli.
[21] R. Machaka and H. K. Chikwanda, An Experimental Evaluation of The Gerdemann–Jablonski Compaction Equation, Metall Mater Trans A, 46 (5) (2015).2194
[22] I.N. Popescu, R. Vidu, Compaction of Metal - Ceramic Powder Mixtures. Part. 1, ARA Journal of Sciences, old ISSN 0896-1018, in press.
[23] I.N. Popescu, R. Vidu, Compaction of Metal - Ceramic Powder Mixtures. Part. 2, ARA Journal of Sciences, old ISSN 0896-1018, in press.
[24] Cardei Petru , Gageanu Iuliana, A Critical Analysis of Empirical Formulas Describing The Phenomenon of Compaction of the Powders, J. Modern Technology & Engineering, 2(1) (2017).1-20
[25] P. Han, X. Z. An, Y. X. Zhang, Z. S. Zou, FEM Modeling on the Compaction oF Fe and Al Composite Powders, J. Min. Metall. Sect. B-Metall. 51 (2) B (2015) 163 – 171
[26] Sinka, I.C. Modelling Powder Compaction, Kona-Powder and Particle 25 (2007) 4-22.
[27] D. Poquillon, J. Lemaitre, et.al. , Cold compaction of iron powders—relations between powder morphology and mechanical properties Part I: Powder preparation and compaction, Powder Technology 126 (2002) 65– 74.
[28] Rusanescu C.O , Jinescu C, Rusanescu M., Enescu M. C., Anghelina F. V., Stoian E. V. , Despa V., Mathematical Modelling of the Stress-Strain Curve for 31VMn12 Ecological Steel, Materiale Plastice 54 (3) (2017) 409-413.

[29] Faruk Güner Ömer Necati Cora Hasan Sofuoğlu, Numerical modeling of cold powder compaction using multi particle and continuum media approaches, Powder Technology
271 (2015) 238-247.
[30] C.L. Martin, D. Bouvard, Study of the cold compaction of composite powders by the discrete element method, Acta Materialia 51 (2003) 373–386
[31] Harthong, Barthelemy; Jerier, Jean-Francois; Richefeu, Vincent; et al. Contact impingement in packings of elastic-plastic spheres, application to powder compaction, International Journal of Mechanical Sciences, 61 (1) (2012) 32-43
[32] Harthong, Barthelemy; Imbault, Didier; Doremus, Pierre, The study of relations between loading history and yield surfaces in powder materials using discrete finite element simulations Journal of the Mechanics and Physics of Solids, 60 (4) 2012, 784-801
[33] Jerier, J-F; Hathong, B.; Richefeu, V.; et al., Study of cold powder compaction by using the discrete element method, Conference: Symposium STPMF 2009, Montpellier, FRANCE, MAY 25-27, 2009, Powder Technology, 208 (2) SI, 537-541.
[34] Fen Huang, Xizhong An; Yuxi Zhang et al., Multi-particle FEM simulation of 2D compaction on binary Al/SiC composite powders, 1st International Workshop on Computational Particle Technology Suzhou, Peoples R China, Powder Technology, 314 SI (2016) 39-48.
[35] Goran Frenning, Compression mechanics of granule beds: A combined finite/discrete element study,
Chemical Engineering, Science, 65 (8) (2010) 2464-2471.
[36]Goran Frenning, An efficient finite/discrete element procedure for simulating compression of 3D particle assemblies, Computer Methods In Applied Mechanics And Engineering, 197 (49-50) (2008). 4266-4272.
[37] DT Gethin, RS Ransing, RW Lewis, et al., Numerical comparison of a deformable discrete element model and an equivalent continuum analysis for the compaction of ductile porous material, COMPUTERS & STRUCTURES 79 (13) (2001). 1287-1294.
[38] K. T. Kim, J. H. Cho, Cold Compaction of Composite Powders, J. Eng. Mater-T. Asme., 122 (2000) 119-128.
[39] K. T. Kim, J. H. Cho, A densification model for mixed metal powder under cold compaction, Int. J. Mech. Sci., 43 (2001)2929-2946
[40] A. Kadir Eksi et.al, Experimental and numerical studies of metallic powders subjected to cold isostatic pressing, International Journal of Materials Research 102 (5) (2011) 572.
[41] Erik Olsson, PhD Thesis, Micromechanics of Powder Compaction, Royal Institute of Technology, Stockholm, 2015.
[42] S. Shima, M. Oyane, Plasticity theory for porous metals, Int. J. Mech. Sci., 18 (1976) 285- 291
[43] A. L. Gurson, Continuum Theory of Ductile Rupture by Void Nucleation and Growth: Part I—Yield Criteria and Flow Rules for Porous Ductile Media, ASME J. Eng. Mater. Technol., 99 (1977) 2–15.
[44] M. F. Moreno, C. J. R. González Oliver, Densification of Al powder and Al–Cu matrix composite (reinforced with 15% Saffil short fibres) during axial cold compaction, Powder.
Technol., 206 (2011) 297-305.
[44] A. K. Eksi, A. H. Yuzbasioglu, Effect of sintering and pressing parameters on the densification of cold isostatically pressed Al and Fe powders,.Mater. Design, 28(4) (2007) 1364..
[45]W. Wu, G. t. al., Experimental and numerical investigation of idealized consolidation: Part 1:Static compaction, Acta Mater., 48 (2000) 4323-4330.
[46] D. Gethin, A.K. Arin, D.V. Tran, R.W Lewis, , Compaction and Ejection of Green Powder Compacts, Powder Metallurgy, 37(1) (1994) 42-54.
[47] T. Sheppard, H.B.McShane, Strength of Cold-Pressed Compacts , Powder Metallurgy, 23 (3).(1980) 120-124.
[48] F. Fischmeister, HE. Arzt, Powder Metallurgy, Densifcation of Powders by Particle Deformation, 26(2) (1983) 82-88.
[49] I.N. Popescu, S. Zamfir, F. V.Anghelina, C.O. Rusănescu, Fabrication through P/M of ecological aluminum based composite materials. Part 1-Characterization and densification of mixture powders, Proceedings of the 2nd Int. Conference on MEQAPS, Constantza, Sep 03,-05(2010) 200-205.

Books:

[50] Amir R. Khoei, Computational Plasticity in Powder Forming Processes, Elsevier Publisher, 2005.

DE GRUYTER OPEN

The Scientific Bulletin of VALAHIA University
MATERIALS and MECHANICS –Vol. 16, No. 14

DOI 10.1515/bsmm-2018-0007

EXPERIMENTAL RESULTS OF VIBROACOUSTIC DIAGNOSIS PERFORMED WITH VIBRO-EXPERT SYSTEM

Ionel RUSA[1], Cornel MARIN[1], Marius BAIDOC[2]

[1]VALAHIA University of Târgovişte, Str. ALEEA SINAIA Nr.13, Targoviste
[2]S.C. VIBRO SYSTEM S.R.L,

Email: marin_cor@yahoo.com, ionelrusa@gmail.com, info@vibrosystem.ro

Abstract. *The implementation of proactive maintenance is a necessity required by the development of modern technologies for the monitoring and exploitation of energy facilities and equipment. An important advantage of* ***proactive maintenance*** *is to permanently monitor the technical condition of the plant and equipment by* ***vibration measurements*** *and in the correct diagnosis in order to reasonably plan the required repairs. Turbo-aggregates are autonomous complex installations for producing electricity in refineries that operate in high power and high-speed modes. To monitor and control turbine vibrations, vibration sensors (uniaxial, biaxial and triaxial accelerometers) and proximity sensors (for relative displacements and lasers) are columned on bearing housings that transmit signals to data acquisition and processing systems as well is the* ***Vibro-Expret diagnosis system*** *presented in this paper.*

Keywords: *Proactive maintenance, Vibration measurement, Vibro Expert diagnosis system*

1. INTRODUCTION

The diagnosis system used in the LUKOIL Turbo aggregate TA4 (*Figure 1*) is intended for the measurement, monitoring, diagnosis, prediction and analysis of the parameters of the turbo aggregate for the purpose of its safe operation. Vibration measurement was performed with the machine in normal operating regime. To diagnose the LUKOIL Turbo aggregate TA4, the following types of measurements were performed:
-absolute speed vibrations of the machine bearings with uniaxial accelerometers;
-relative displacements vibrations of the proximity sensor spindle at the generator bearings.
The technical characteristics of the LUKOIL Turbo aggregate TA4 are:
Power: 32 MW; Speed: 3000 rpm;
Stator 11 kV, 2100 A, Rotor 532 A;
Water flow: 150 mc / h

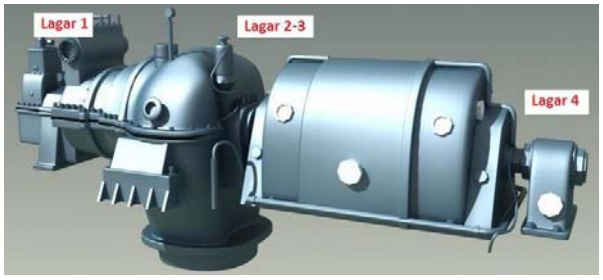

Figure 1. The 3D view of Turbo aggregate TA4

Vibration measurements and experimental data processing were made in accordance with international standards: ISO 7919-1: 1996 [9]; ISO 7919-3: 1996 [10]; ISO 10817-1: 1998[11]; ISO 10816-1: 1995 [12]; ISO 10816-3: 2009 [13]; SR ISO 5348 –1: 1998[14].

2. VIBRO EXPERT DATA ACQUISITION AND PROCESSING SYSTEM

2.1. The professional **VIBRO EXPERT data acquisition and processing system** is manufactured by **Delphin Technology Germany LTD** (*Figure 2*)**.** This professional system consists of two acquisition modules with 8 channels each: 8 sensors for vibration measurement of the **relative proximity** and 8 accelerometer transducers **VIBRASENS** for **speed vibration** measuring.

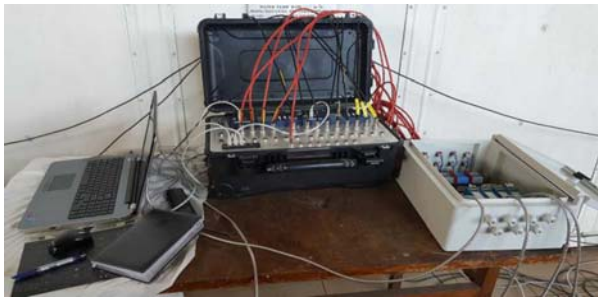

Figure 2. Vibro Expert Purchasing and Diagnosis System

The block diagram of the Vibro Expert Diagnostic System and Module Integration is shown in Figure 3
The diagram of the location of the vibration measurement points on the bearings 1,2, 3 and 6 is shown in Figure 4. Figure 5 shows a lateral view of the TA4 turbo aggregate with two pairs of vibration

absorbing masses (two bayonets and two electric motors with very large masses).

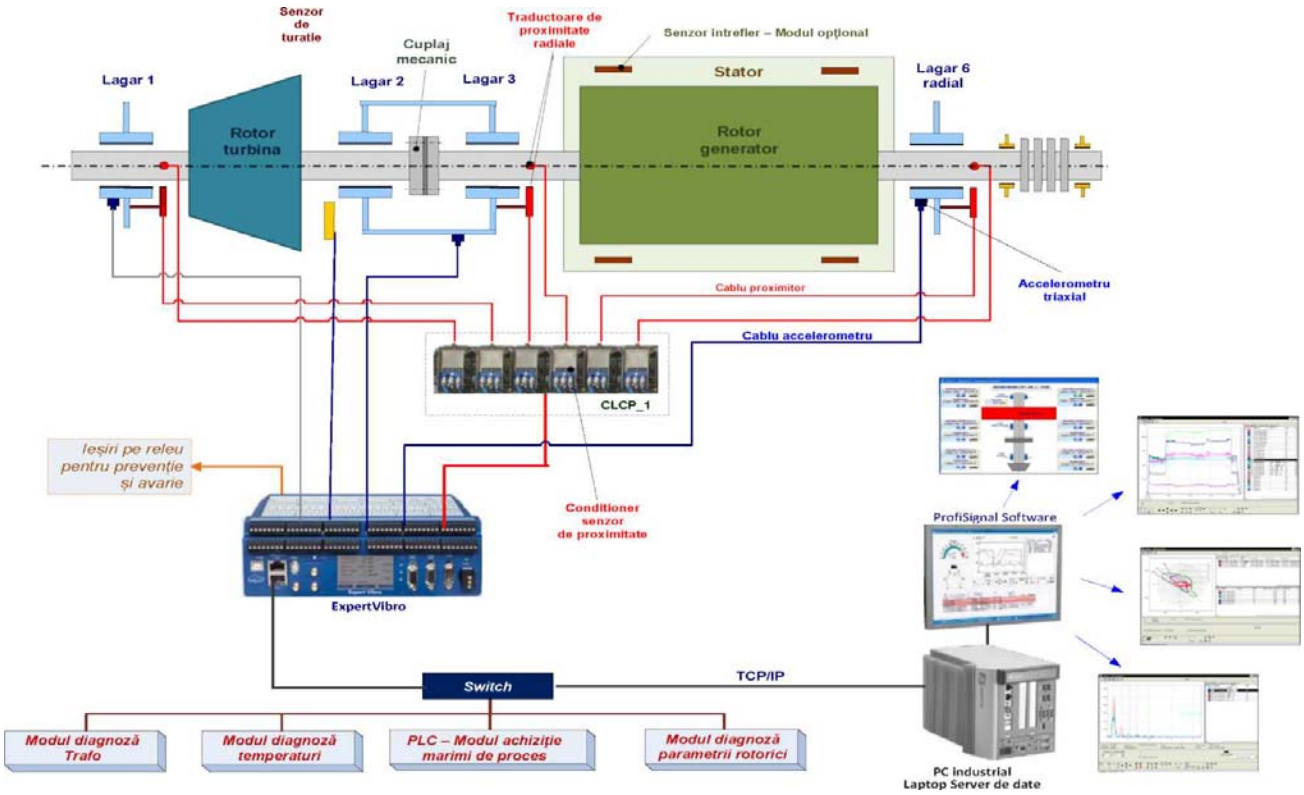

Figure 3. Modular integration block of the Vibro Expert Diagnostic System

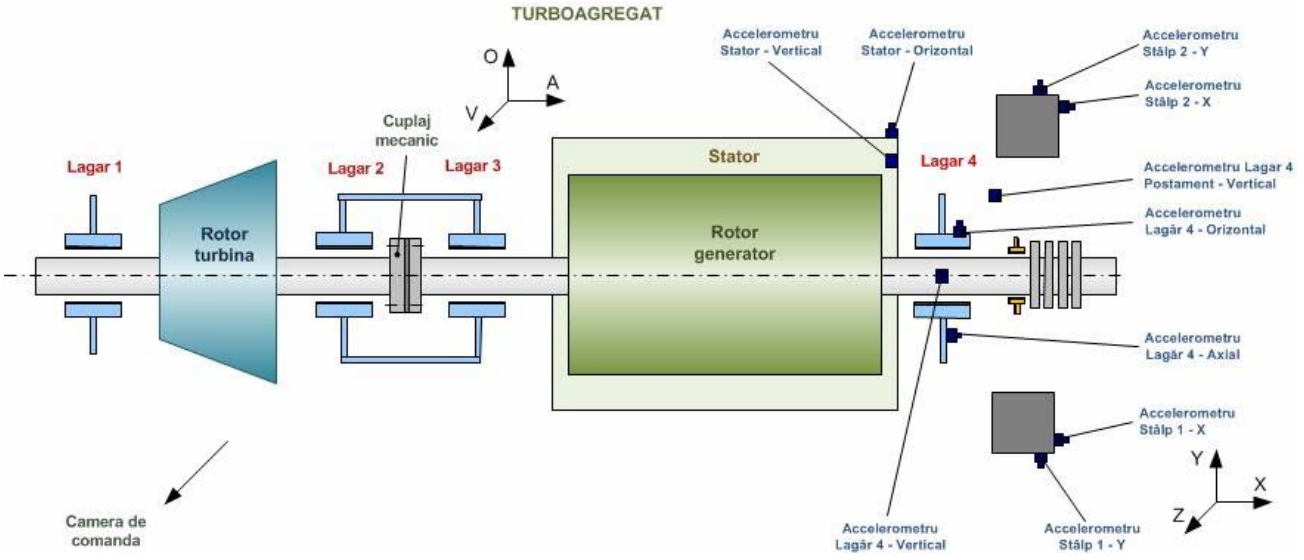

Figure 4. Schemes of location of vibration measurement points on bearings 1,2, 3 and 4

Figure 5. The lateral view of the TA4 turbo aggregate

2.2. The accelerometer and proximity transducers used in measurements are VIBRASENS 101.51-9, piezo-ceramic sensor (*Figure 6*) and ROLS-W Monarch Instruments laser sensor Technical specifications of the synchronization, speed and phase transducer **ROLS-W - Monarch Instruments** (*Figure 7*): have the technical specification presented in published papers [1], [4] , [5]

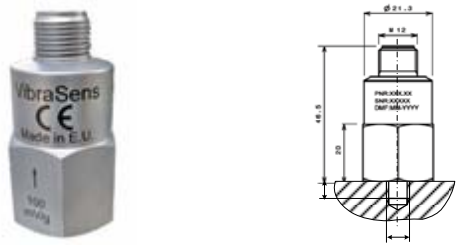

Figure 6. The accelerometer VIBRASENS 101.51-9

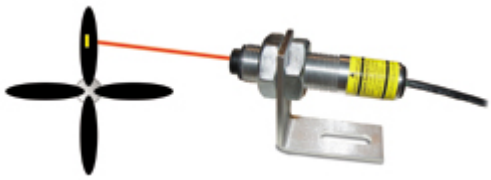

Figure 7. The laser sensor ROLS-W Monarch Instruments

3. TECHNICAL CONDITIONS AND TYPES OF MEASUREMENTS

Figures 8, 9, 10 show the specific position of sensors - accelerometers and proximity sensors - after the three directions V (vertical), O (horizontal) and A (axial) respectively X, Y and Z directions for the turbo-aggregate bearings, according to the Technical Report [8] .

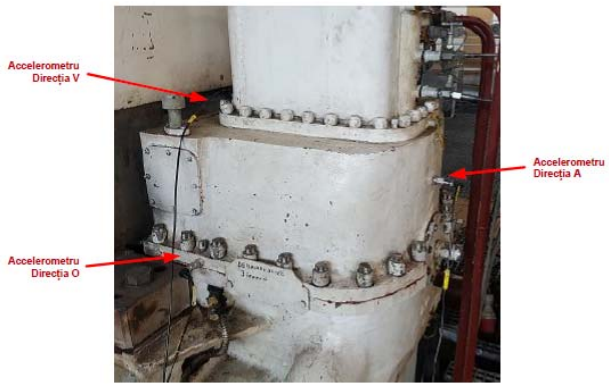

Figure 8.

Vibration measurements were accomplish on the turbo aggregate in the several operating modes:

a. At nominal speed 3000 rpm and 20 MW power load of turbo aggregate, with 8 metal plates columned on bearing 4 (*Figure 9*)

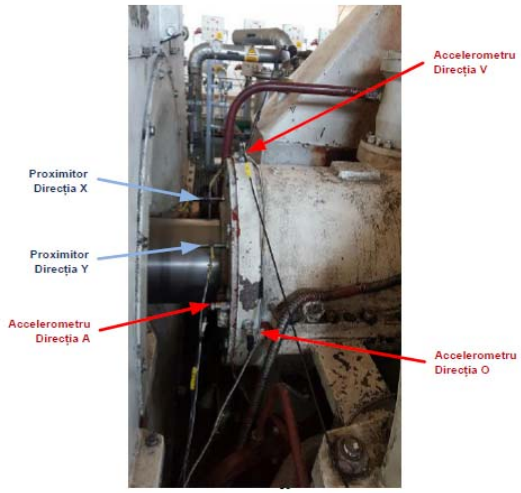

Figure 9.

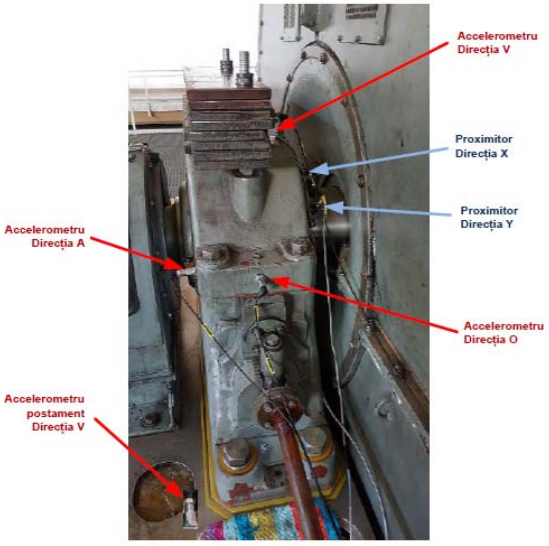

Figure 10.

b. At the nominal speed 3000 rpm and 14 MW power load of turbo aggregate with different plate numbers columned on bearing 4: 8 /7 /6 /5 /4 /3 /1 /0.

Using the VibroExpert diagnosis System, the following technical parameters and types of measurements of global vibration values and technical parameters were monitored:
- Relative vibration of the turbo aggregate shaft according to ISO 7919-3
- Absolute vibration according to ISO 10816-3: absolute speed vibration and absolute vibration of movement
- Absolute displacements of base - component 1x - 50 Hz, 2x - 100 Hz, 3x - 150 Hz recorded also on Bearing 4 and its column in vertical direction.
- Waveforms and Frequency Spectra for acceleration, velocity and displacement
- Orbit bearings and vibrations absolute and relative, etc.

ISO 7919-3: 1996 and ISO 10816-3: 2009 standards present the performance ratings of the turbo aggregate when it is energy-conscious, having four operating ratings:
Rating A - Good
Rating B – Usable
Qualification C - Admitted under supervision
Qualification D - Not allowed

The performance ratings in the frequency range 10 ÷ 1000 Hz and power 32 MW according to ISO 7919-3:1996 respectively ISO 10816-3: 2009 are specified in the *Table 1*and *Table 2*.

Table 1

ISO7919-3:1996		
Machine		Turboagregate 3000 rpm, P =32 [MW]
Measurement parameter		Displacement Pick- pick [µm]
Performance ratings	Good – A	under 85
	Usable – B	85-160
	Admitted under supervision – C	160 - 240
	Not allowed – D	over 240

Table 2

ISO 10816-3:2009			
Machine		Turboagregate 3000 rpm, P =32 [MW]	
Measurement parameter		Speed RMS [mm/s]	Displacement Pick- pick [µm]
Performance ratings	Good – A	under 2,3	under 29
	Usable – B	2,3-4,5	29-57
	Admitted under supervision – C	4,5-7,1	57-90
	Not allowed – D	over 7,1	over 90

4. MEASUREMENT DIAGNOSIS OF TURBO AGGREGATE OPERATION STATUS

Diagnosis of turbo aggregate operation was performed in all operating modes of the machine described in paragraph 3 by analyzing the relative displacement vibration (Pick- Pick) and absolute vibration (RMS velocity and displacement Pick- Pick).

The measurement values obtained for these characteristics for bearing 4 are shown in Table 3.

Table 3

No. plates on Bearing 4	Measurement direction							
	Vertical – Bearing 4				Vertical – Bearing 4 Basis			
	10 - 1000 Hz	50 Hz - 1x	100 Hz - 2 x	150 Hz - 3x	10 - 1000 Hz	50 Hz - 1x	100 Hz - 2 x	150 Hz - 3x
	mm/s - RMS	mm/s	mm/s	mm/s	mm/s - RMS	mm/s	mm/s	mm/s
8 plates	3,89	3,69	0,95	0,02	4,11	3,95	0,70	0,04
7 plates	3,83	3,64	1,08	0,02	4,02	3,93	0,73	0,04
6 plates	3,76	3,58	1,09	0,04	3,84	3,75	0,74	0,05
5 plates	3,53	3,34	0,97	0,04	3,59	3,48	0,64	0,03
4 plates	3,55	3,33	1,18	0,04	3,62	3,47	0,71	0,03
3 plates	3,56	3,22	0,95	0,02	3,68	3,56	0,69	0,03
2 plates	3,50	3,25	1,01	0,02	3,65	3,49	0,68	0,02
1 plates	3,31	3,18	0,66	0,06	3,72	3,56	0,75	0,02
0 plates	3,49	3,29	1,04	0,05	3,76	3,65	0,73	0,02
	Horizontal – Bearing 4				Axial – Bearing 4			
8 plates	1,05	0,90	0,29	0,25	5,99	5,19	2,58	0,20
7 plates	1,03	0,89	0,30	0,27	6,00	5,09	2,99	0,24
6 plates	1,04	0,89	0,32	0,27	5,63	4,72	3,03	0,19
5 plates	1,04	0,88	0,31	0,26	5,57	4,59	2,81	0,18
4 plates	1,03	0,90	0,33	0,27	6,02	4,81	3,21	0,26
3 plates	1,02	0,89	0,29	0,26	6,30	4,79	3,16	0,18
2 plates	1,04	0,90	0,29	0,26	6,26	4,90	3,44	0,25
1 plates	1,06	0,90	0,31	0,29	6,36	5,47	2,82	0,23
0 plates	1,04	0,90	0,29	0,28	6,94	5,39	4,14	0,31

Following the vibration measurements, higher amplitudes of relative vibrations were recorded on the 2-3 bearing, and on the bearing 4 the vibration values are small. These amplitudes have been recorded at all measured operating regimes, resulting in the machine's functional rating. **Usable** - *Global Relative Vibration Level Bulletin No. 1* [7]

Diagnosis of relative vibration indicates a slight loading of the bearing 2-3 which may lead to the de-shaft of the shafts in the vertical direction: *Appendix 1 - Figure A.9./A10. Orbit 2-3 bearing 4.*

From records of absolute vibration movement, the machine qualifies as **Good** for all measurement modes: *Global Absolute Movement Level Measurement Bulletin no. 3* [7]

Diagnosis of absolute vibrations, i.e. vibration velocity amplitudes, fits the machine to the 14MW and 20MW rating **Under supervision:** *Absolute Speed Global Bulletin Measurement Bulletin no. 2.* [7]

The highest amplitudes of vibration velocity were recorded on the bearing 4 in the axial direction (*Table 3*). From the information provided by the beneficiary, it results that the bearing 4 resonates at the speed of 3000 rpm - 50 Hz. For this purpose, a series of global vibration measurements and spectral components 1x - 50 Hz / 2x - 100 Hz / 3x - 150 Hz were made at the bearing 4, on which up to 8 metal plates were columned at the upper part. From the measurements made it follows that the smallest vibrations were recorded on the 5-plate bearing, resulting in a total value of 5.57 mm / s, the component 1x of 4.59 mm / s, the 2x component of 2.81 mm / s , the 3x component of 0.18 mm / s. *Appendix 1 - Figures A.11.A12.A13.*

Frequency Spectrum Bearing 4 - A / O / V - Measuring mode: 5 plates on bearing 4. This value of 5.57 mm / s exceeds the value of 4.5 mm / s as prescribed by the standard, which still qualifies the machine as admitted under supervision. *Appendix 1 - Figure A.15. Turbo aggregate Vibration Parameters - Measurement Mode: 5 plates on the bearing 4.*

The frequency spectra recorded on the bearing 4 indicate a possible misalignment as a defect which can be amplified by the bearing frequency 4 of the bearing.

The recorded vibration measurements indicate that the speed values on the base are higher than those on the bearing on the same measuring direction - vertically, which means that the vibrations can be transmitted to the bearing by the base. *Appendix 1 - Figure A.14. Frequency Spectrum Bearing 4 - V Plate - Measuring Mode: 5 Plates on bearing 4.*

5. CONCLUSIONS AND RECOMMENDATIONS

For a correct machine diagnosis it is recommended to perform additional measurements in different working modes such as:

- When rising from 0 rpm to rated speed and super attitude to determine the position of the center of the spindle in the bearing and the resonance frequency of the bearing 4. In this case, the relative and absolute global vibration is measured, the relative displacement of the spindle, the component 1x, 2x simultaneously phase measurement (Run up).

- Vibration measurement at idle idle speed at rated speed, excited nose and maximum load. Vibration analysis at unplanned idle mode.

- Measuring transmissibility of triaxial vibrations from the bearing 4 to the base plate / base - concrete foundation - the generator casing.

The first two types of measurements were not possible due to the unavailability of the machine. If the increased speed vibration is due to the resonance frequency of the bearing 4, it can be reduced by additional masses on the bearing.

REFERENCES

[1] Ionel Rusa, Cornel Marin, Marius Baidoc. "New Measurements Results Achieve for Proactive Maintenace with Vibro-Expert Diagnosis System", Scientific Bulletin of Valahia University - Materials and Mechanics, 2017.

[2] * * * Mentenanța utilajelor dinamice vol . 1 – Mobil Industrial AG – Pitești (2011)

[3] Torben R. Licht , Vibration Calibration Technique and basics of Vibration Measurement -– Singapore 2011.

[4] Ionel Rusa, Cornel Marin, Marius Baidoc, " Case Study Regarding Measurements Implemented with the Repair Entry a Hydrogregate Campela with Vibro Expert Diagnosis System", Springer Nature, 2018

[5] Ionel Rusa, Cornel Marin, Marius Baidoc " Case Study Regarding Measurements Implemented with the Repair Entry a Hydrogregate Campela with Vibro Expert Diagnosis System" Proceedings of the International Conference of Mechatronics and Cyber-MixMechatronics - 2017", Springer Nature, 2018

[6] Bill Powel, Tony Burnet Automated machinery maintenance.

[7] S.C. VIBRO SYSTEM S.R.L. www.vibrosystem.ro – BULETINE DE MĂSURARE A NIVELULUI GLOBAL DE VIBRAȚII RELATIVE NR. 1 ; NR. 2 şi NR. 3

[8] S.C. VIBRO SYSTEM S.R.L. www.vibrosystem.ro – Raport tehnic privind măsurătorile de vibrații efectuate cu sistemul de diagnoză expert vibro la turboagregatul TA 4 – CET II LUKOIL ENERGY&GAS S.R.L, 2017

[9] ** * ISO 7919-1: 1996 - Vibrații mecanice ale maşinilor. rotativi şi riteriile de evaluare. Partea 1: Prescripții generale.

[10] ** * ISO 7919-3: 1996, Vibrații mecanice. Evaluarea vibrațiilor maşinilor prin măsurători ale arborelui rotativ. Partea 3: Masini industriale cuplate.

[11] ** * ISO 10817-1 : 1998, Sisteme de măsurare a vibrațiilor relative a arborilor rotativi. Partea 1: Detectarea vibrațiilor absolute şi relative radiale.

[12] ** * ISO 10816-1 : 1995, Vibrații mecanice. Evaluarea vibrațiilor maşinilor prin măsurători pe părțile non-rotative. Partea 1: Prescripții generale

[13] ** * ISO 10816-3 – 2009, Vibrații mecanice. Evaluarea vibrațiilor maşinilor prin măsurători pe părțile non-rotative. Partea 3: Maşini industriale cu puterea nominala peste 15 kW şi turația între 120 rpm şi 15000 rpm măsurate in situ.

[14] ** * SR ISO 5348 – 1998, Vibrații şi şocuri mecanice. Fixarea mecanică a accelerometrelor

[16] ISO 10817-1 : 1998, Sisteme de măsurare a vibrațiilor relative a arborilor rotativi. Partea 1: Detectarea vibrațiilor absolute şi relative radiale.

[17] ISO 10816-1: 1995 Vibrații mecanice. Evaluarea vibrațiilor maşinilor prin măsurători pe părțile non-rotative. Partea 1: Prescripții generale.

[18] ISO 10816-5 - 2000 , Vibrații mecanice. Evaluarea vibrațiilor maşinilor prin măsurători pe părțile non-rotative. Partea 1: Prescripții generale. Partea 5: Hidroagregate şi pompe.

APPENDIX

Figure A.0. Turbo aggregate Vibration Parameters - Measurement Mode: 5 plates on the bearing 4

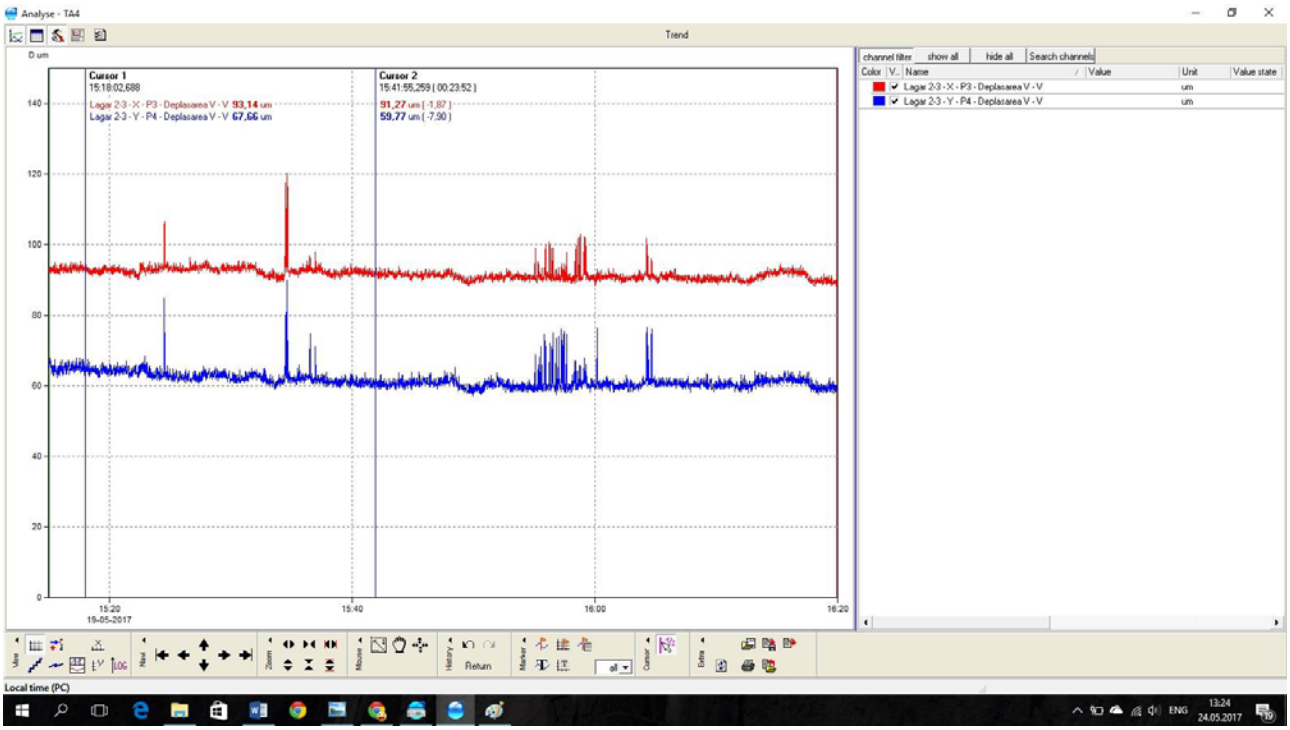

Figure A.1. Trend vibration parameters relative to bearing 2-3. Measuring mode: 8 ... 0 plates on bearing 4, cursor 1 - 8 plates / cursor 2 - 5 plates

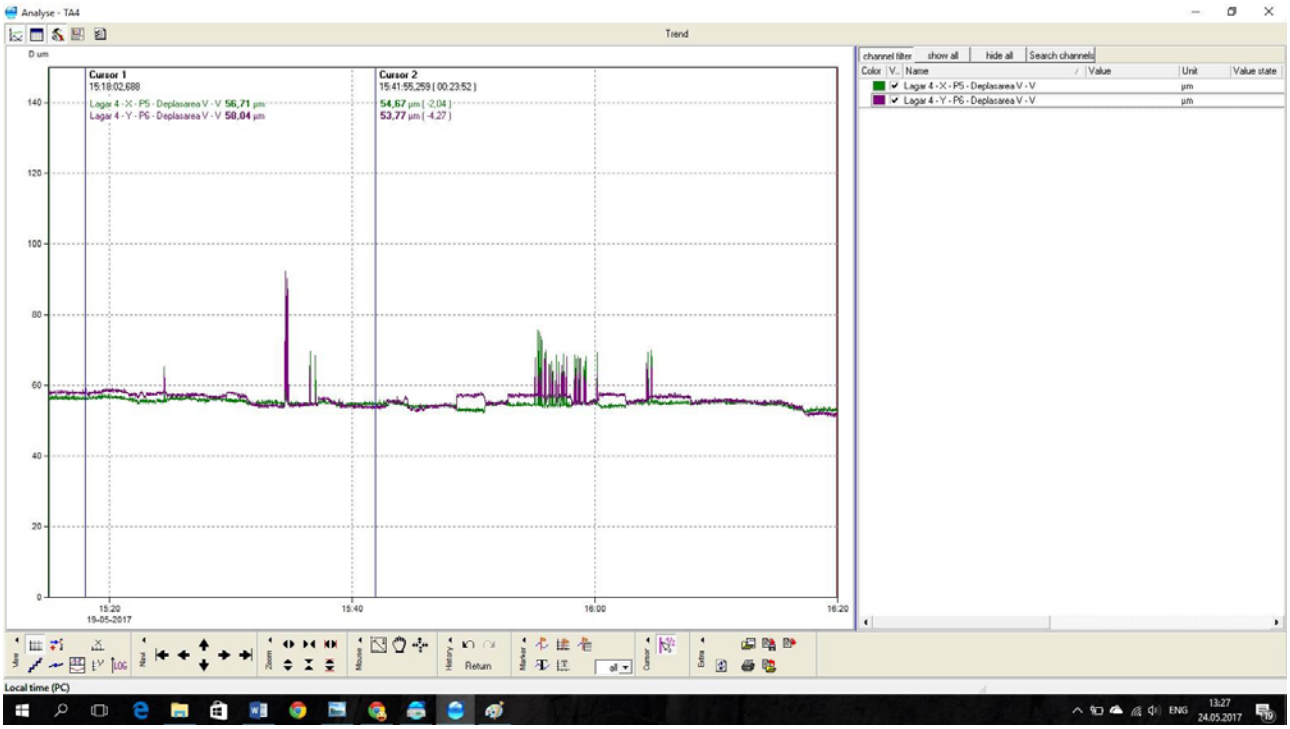

Figure A.2 Trend vibration parameters relative to bearing 4. Measuring mode: 8 ... 0 plates on bearing 4, cursor 1 - 8 plates / cursor 2 - 5 plates

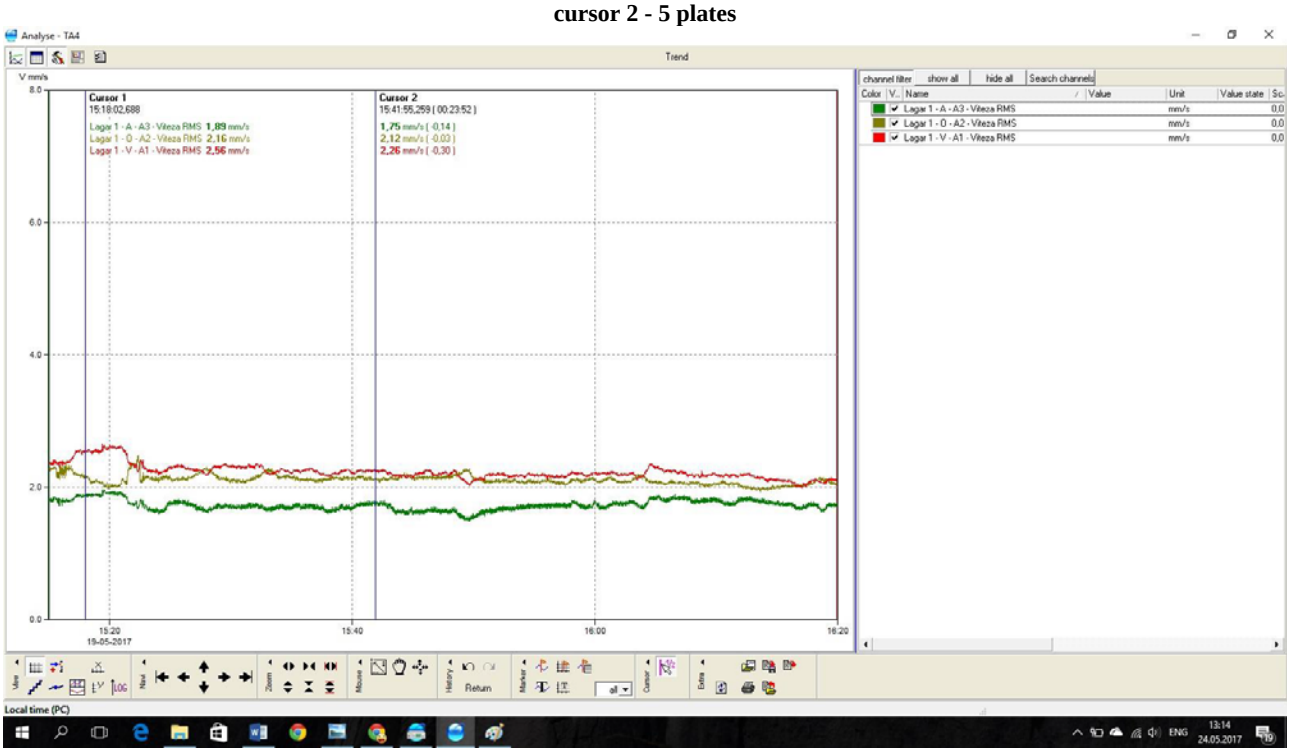

Figure A.3 Trend vibration parameters absolute to bearing 1. Measuring mode: 8 ... 0 plates on bearing 4, cursor 1 - 8 plates / cursor 2 - 2 plates

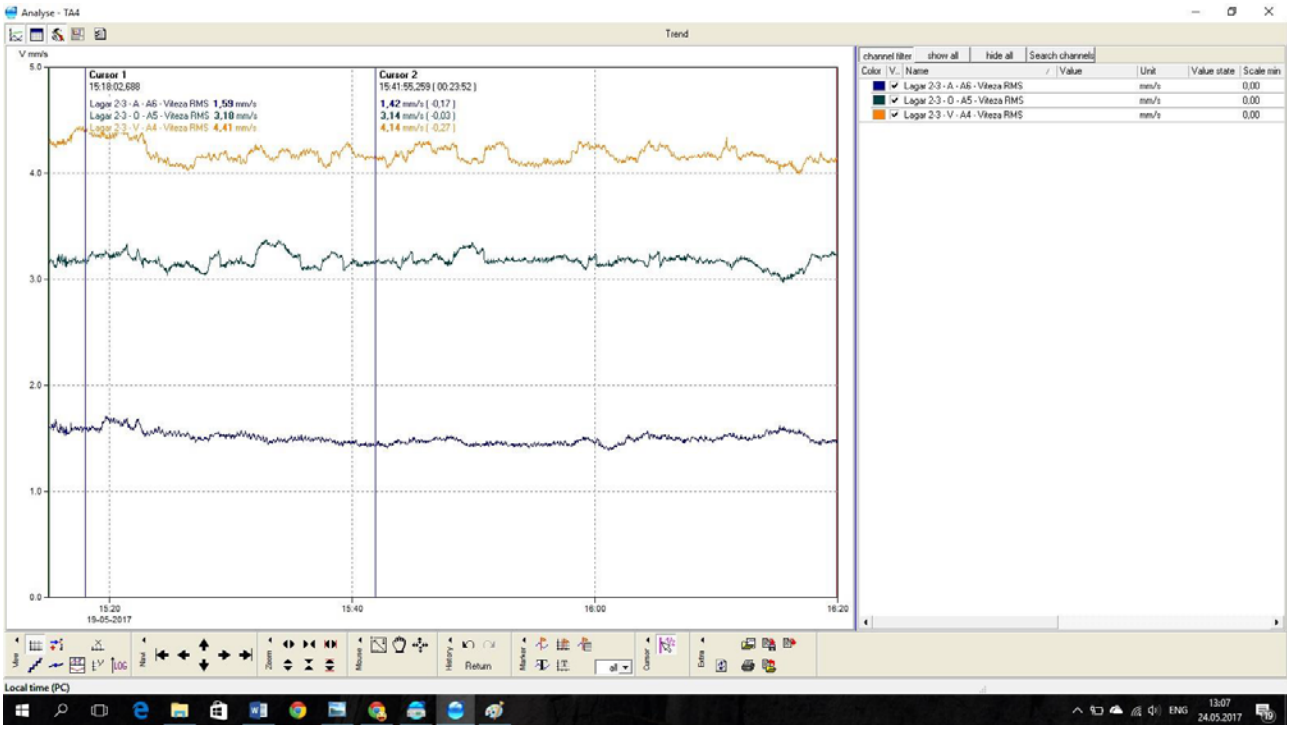

Figure A.4 Trend vibration parameters absolute to bearing 2-3. Measuring mode: 8 ... 0 plates on bearing 4, cursor 1 - 8 plates / cursor 2 - 2 plates

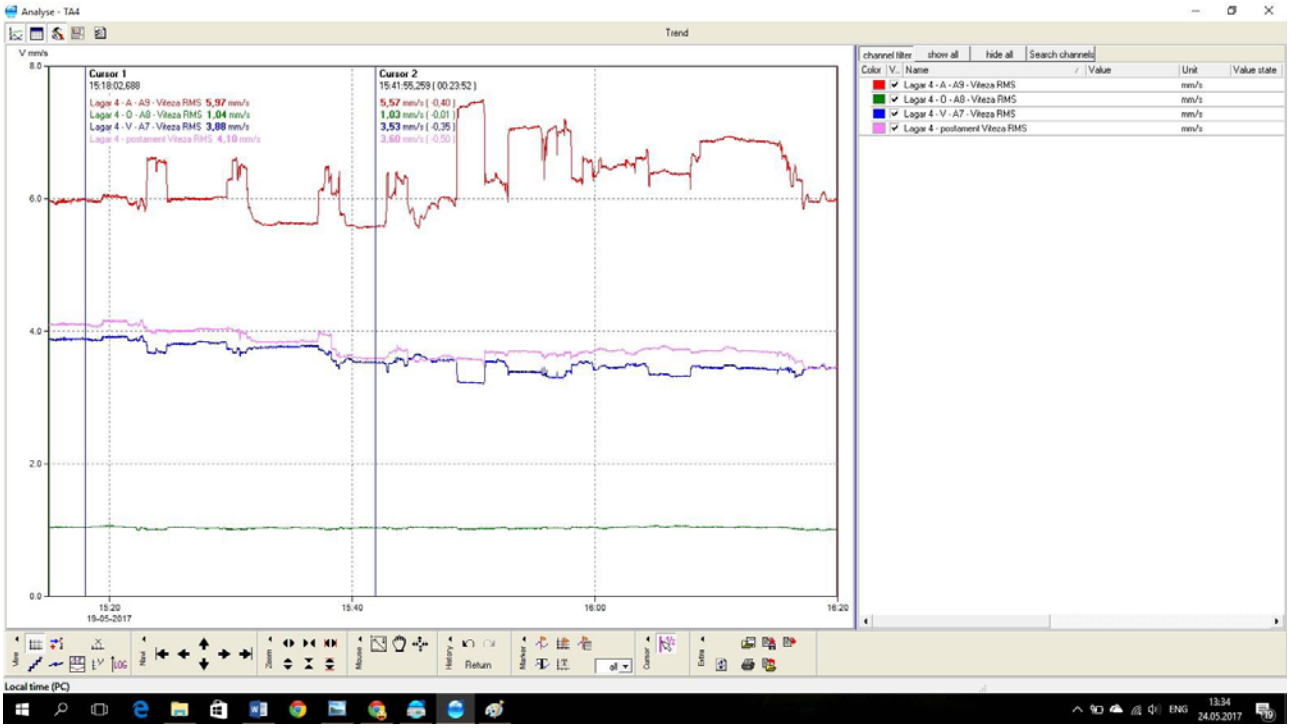

Figure A.5. Trend absolute speed bearing 4 and base. Measuring mode: 8 ... 0 Plates on bearing 4, Cursor 1 - 8 Plates / Cursor 2 - Plates

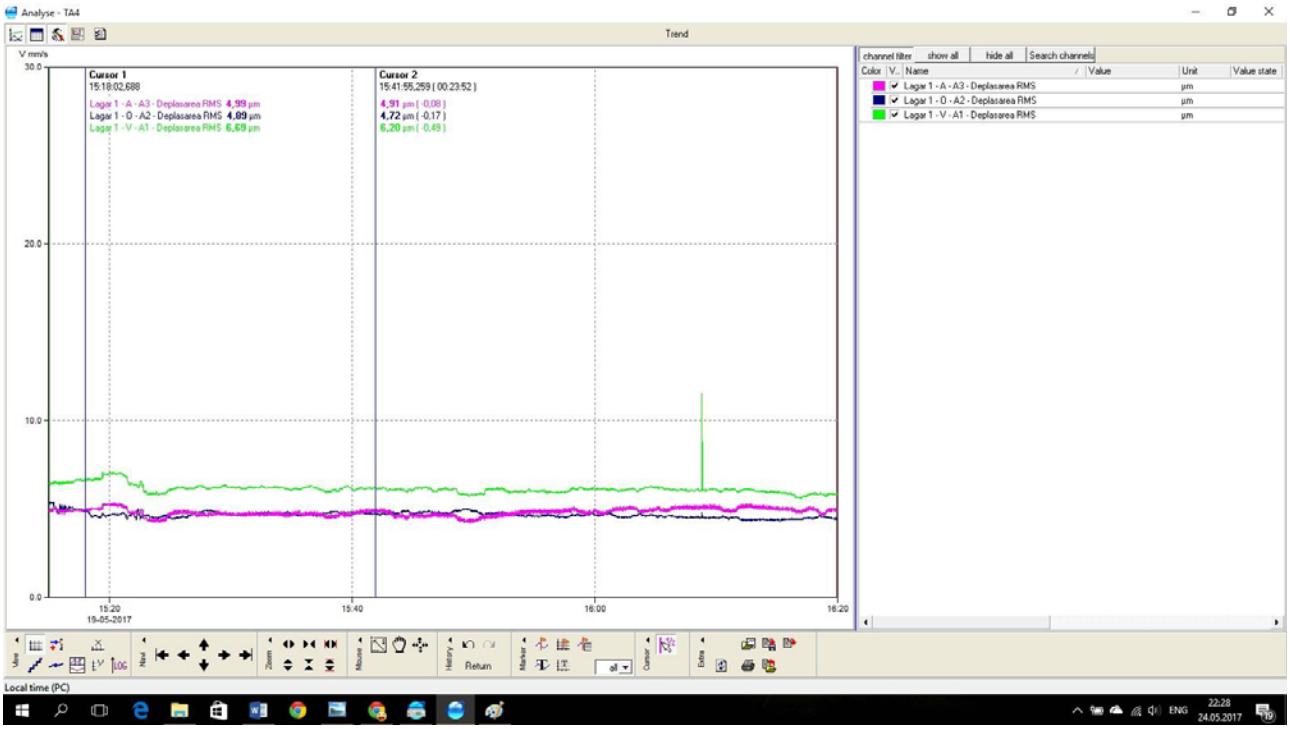

Figure A.6. Trend absolute speed bearing 1 and base. Measuring mode: 8 ... 0 Plates on bearing 4, Cursor 1 - 8 Plates / Cursor 2 - Plates

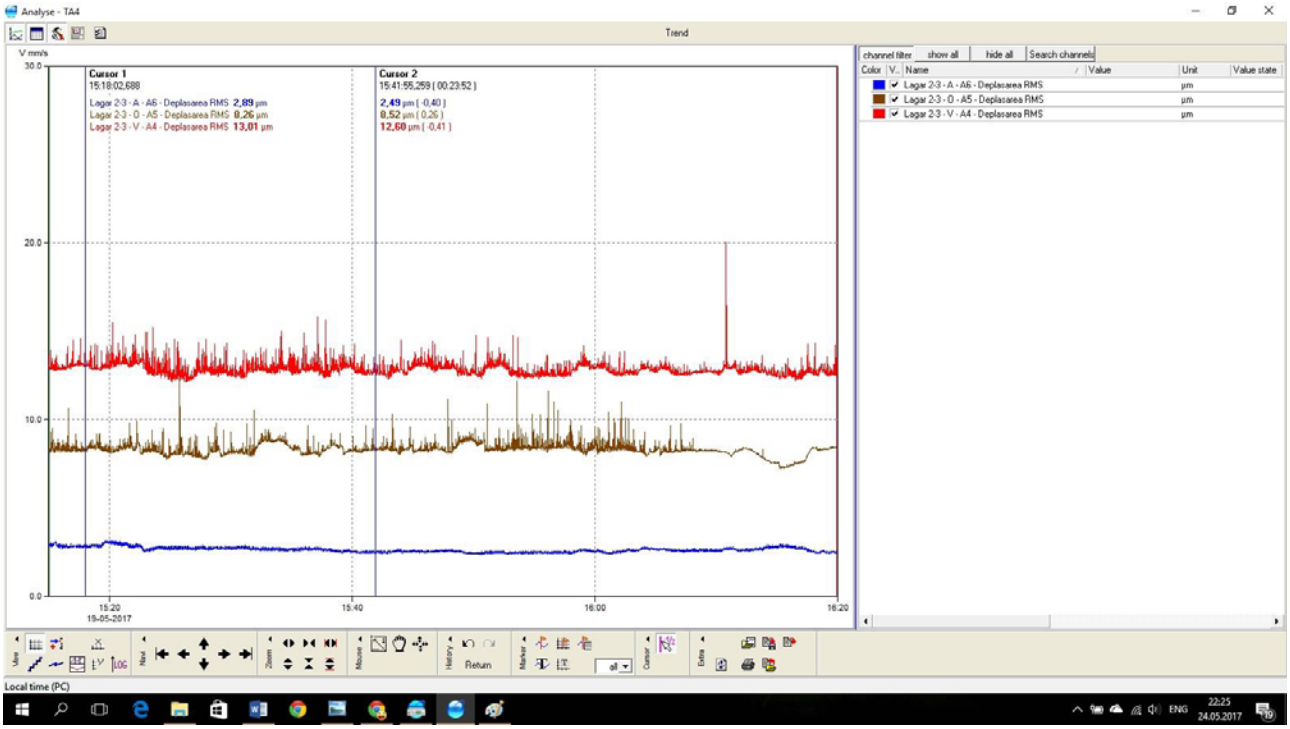

Figure A.7. Trend absolute speed bearing 2-3 and base. Measuring mode: 8 ... 0 Plates on bearing 4, Cursor 1 - 8 Plates / Cursor 2 – Plates

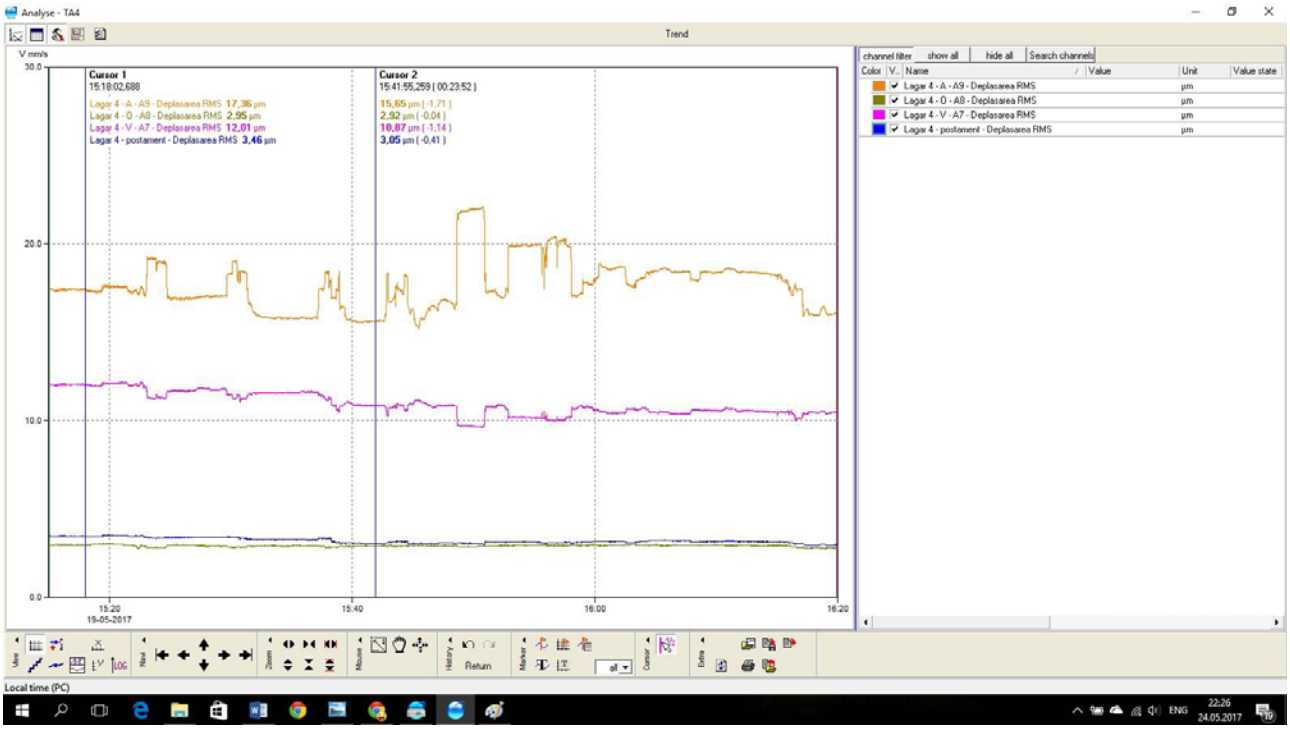

Figure A.8. Trend absolute speed bearing 4 and base. Measuring mode: 8 ... 0 Plates on bearing 4, Cursor 1 - 8 Plates / Cursor 2 – Plates

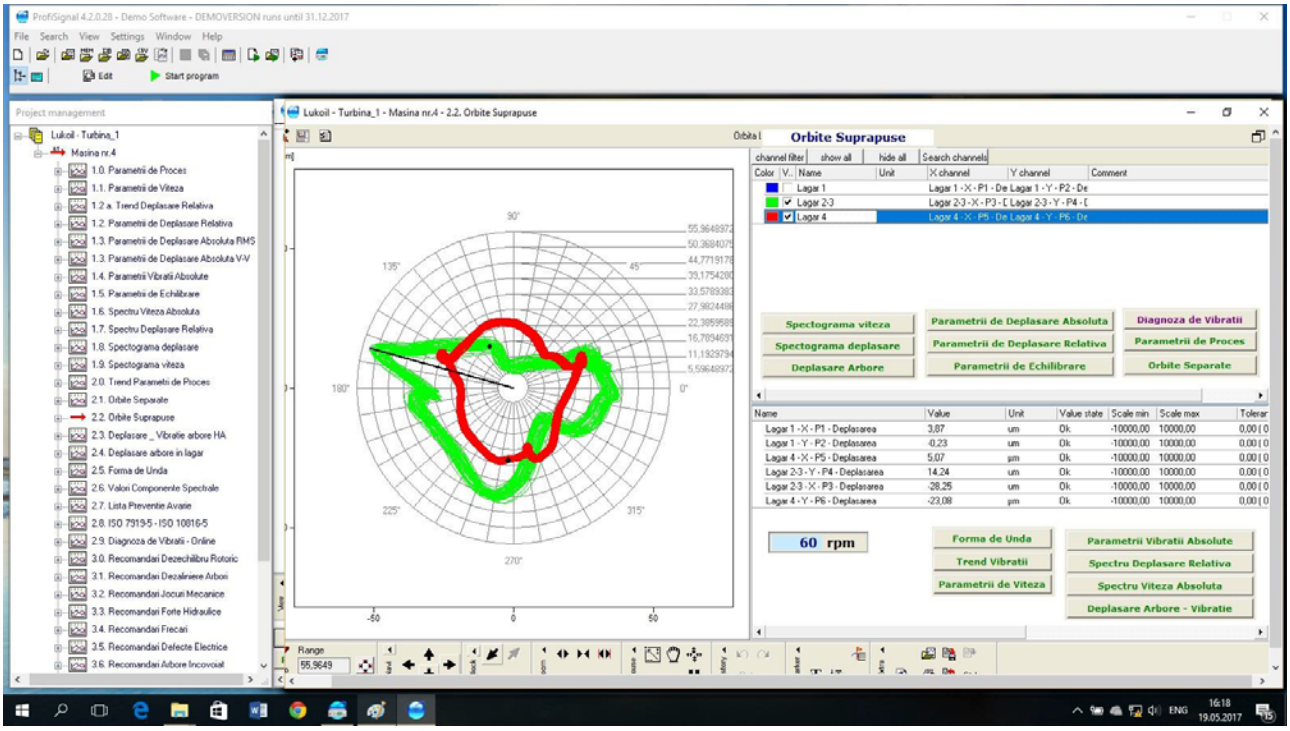

Figure A.9. Orbital movement bearing 2-3 and bearing 4. Measuring regime: 5 plates on the camp 4

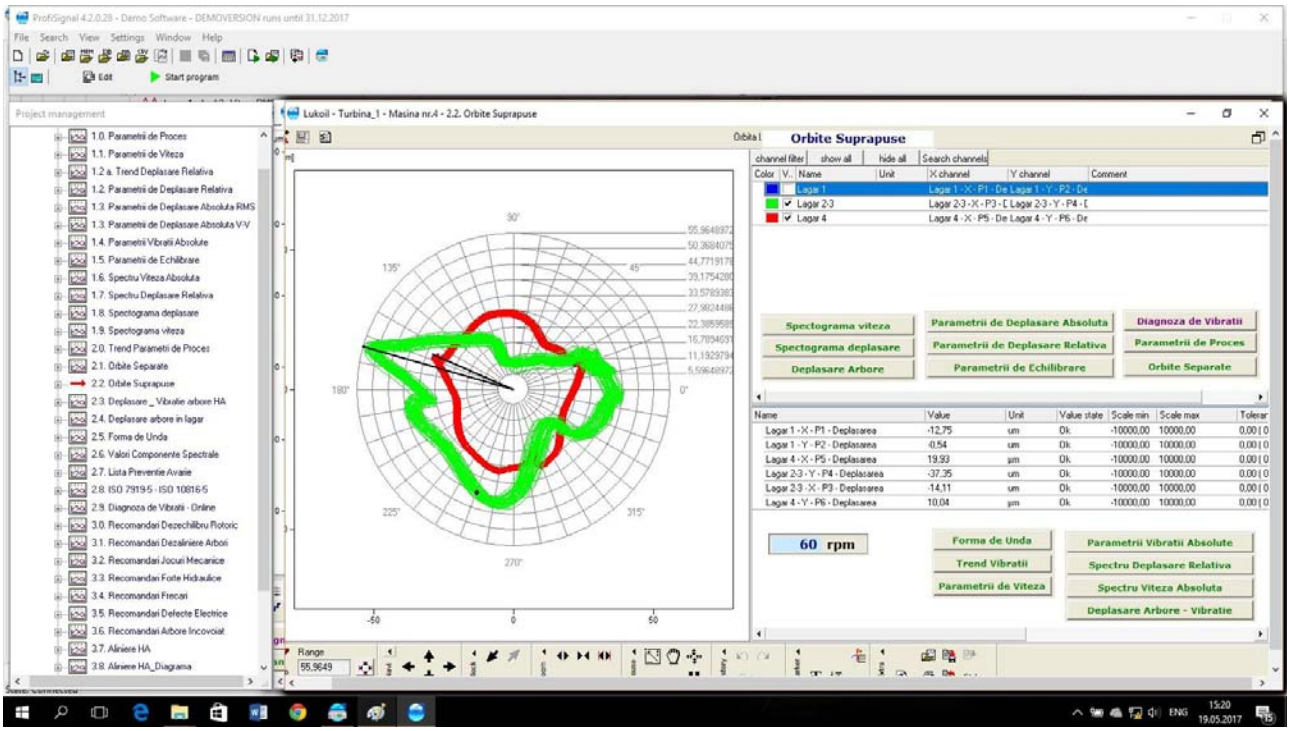

Figure A.10. Orbital movement bearing 2-3 and bearing 4. Measuring regime: 8 plates on the camp 4

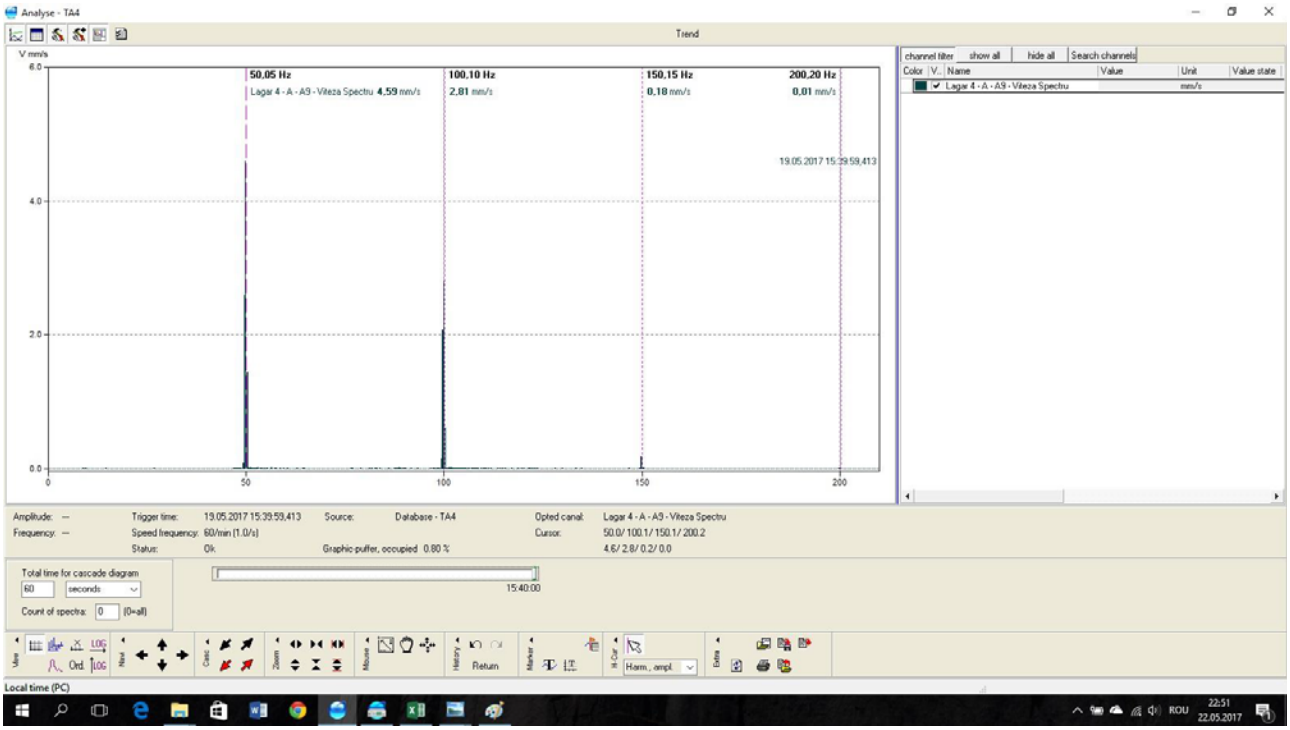

Figure A.11. Frequency Spectrum Bearing 4 - Axial - Measuring mode: 5 plates on bearing 4

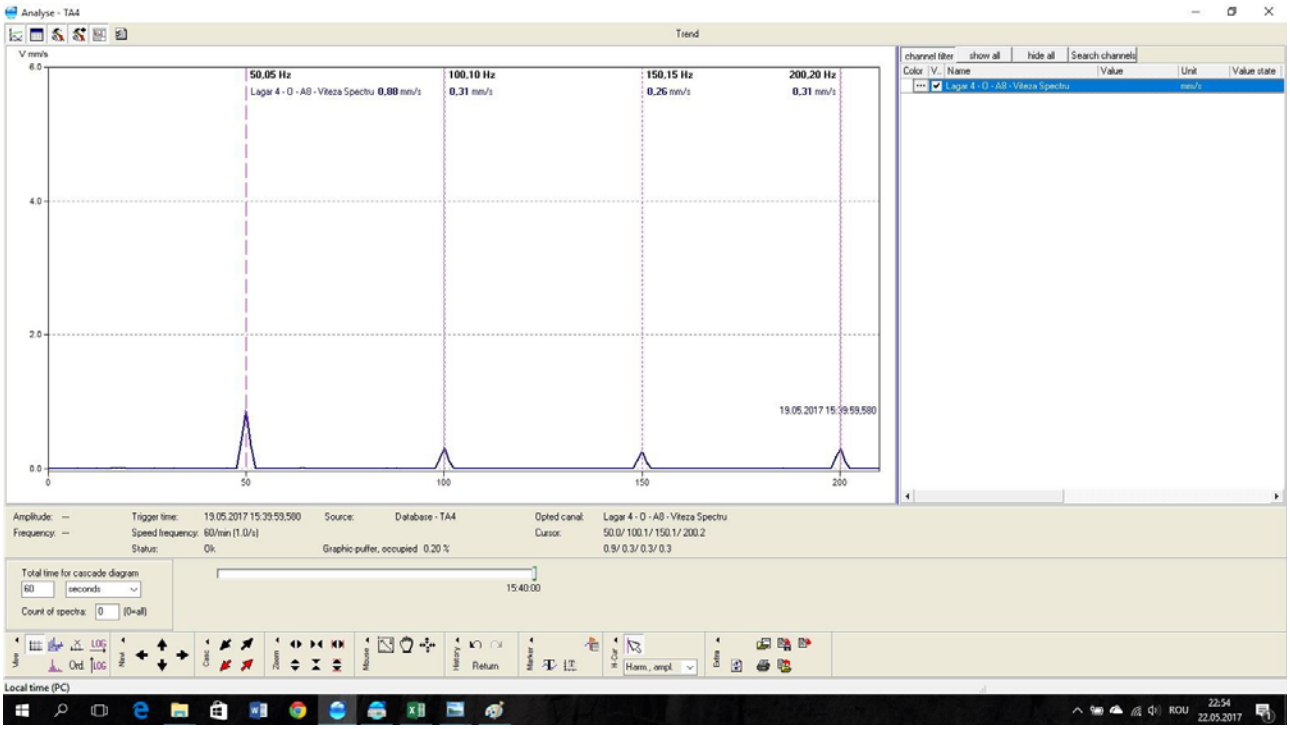

Figure A.12. Frequency Spectrum Bearing 4 - Horizontal - Measuring mode: 5 plates on bearing 4

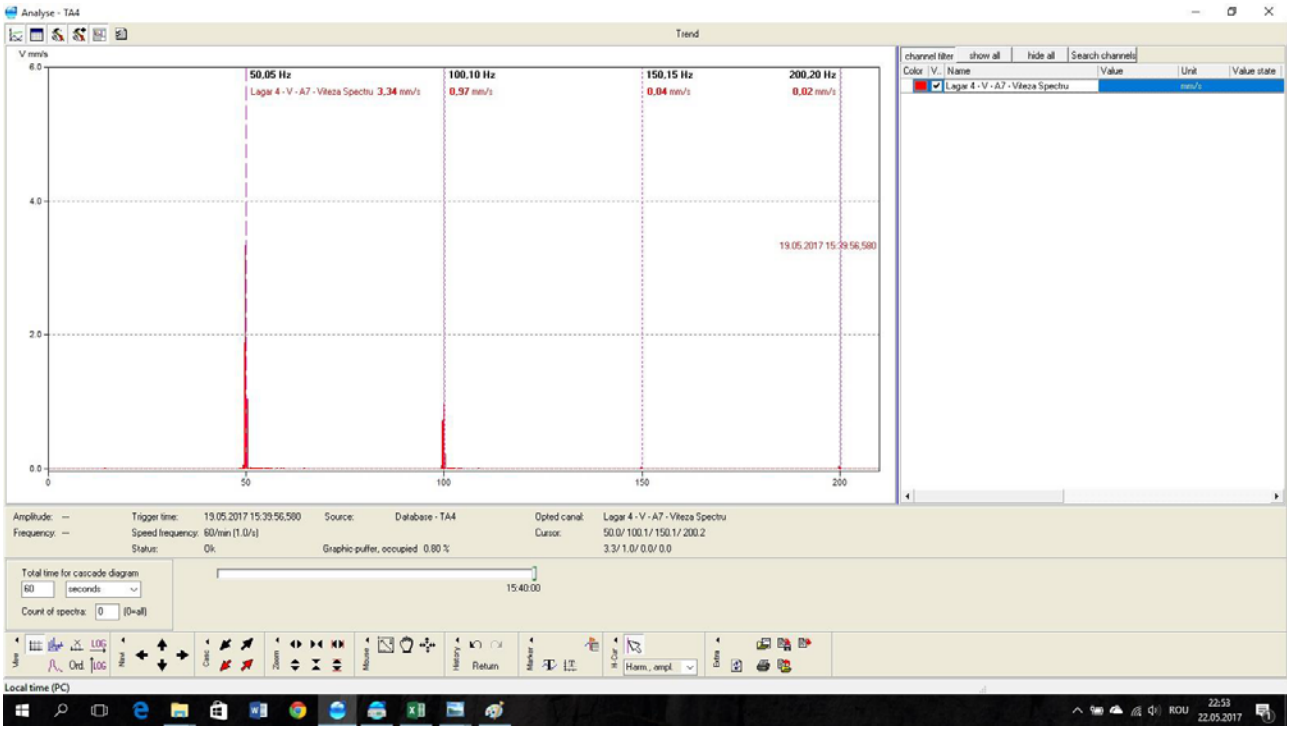

Figure A.13. Frequency Spectrum Bearing 4 - Vertical - Measuring mode: 5 plates on bearing 4

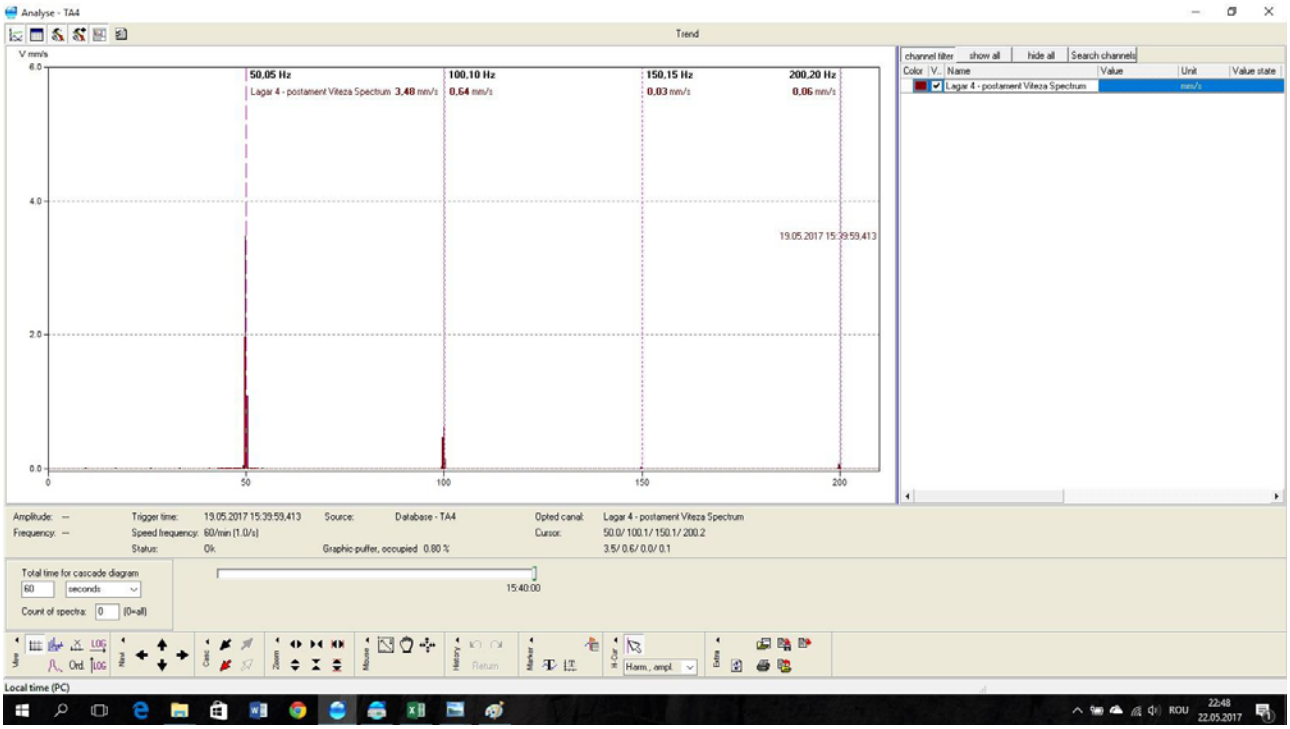

Figure A.14. Frequency Spectrum Bearing 4 – Vertical Postament - Measuring mode: 5 plates on bearing 4

DE GRUYTER OPEN

The Scientific Bulletin of VALAHIA University
MATERIALS and MECHANICS –Vol. 16, No. 14

DOI 10.1515/bsmm-2018-0008

INTELLIGENT CYBER-MIXMECHATRONIC MICRO-SYSTEM FOR MONITORING AND CONTROLLING THE SECURITY AND SURVEILLANCE ROBOTS

Dorin ANGELESCU, Gheorghe Ion GHEORGHE

University Valahia Târgovişte - Doctoral School of Mechanical Engineering, Târgovişte, Romania

E-mail: dorin.angelescu@incdmtm.ro

Abstract. *As a result of the scientific concerns of the Doctoral School of Mechanical Engineering and Mechatronics at Valahia Târgovişte University in the field of robotics dedicated to security and surveillance, the scientific work "Intelligent Cyber-Mixmechatronic Micro-System for Monitoring and Controlling the Security and Surveillance Robots" is in the testing and experimentation phase, within the doctoral (industrial) thesis "Studies, research and contributions regarding the realization of a smart mecatronic robot for security and surveillance applications". The scientific work results in a highly efficient cyber-mixmecatronic system, unique in Romania, which will be used to control the mechatronic security and surveillance robot, respectively the propulsion and control of its displacement. The robot is controlled through Artificial Intelligence, using the Internet of Things (IoT), which is why the Intelligent Motion Control system must be optimized both in terms of response speeds and energy. At the same time, due to the varied and possibly unstable conditions of the displacement field, the system must meet stringent criteria of reliability, resilience, weather, stability and redundant solutions for on-site repair of potential failures during missions. The cyber-mixmecatronic system designed to move the robot must carry it safely at the mission site so that it can then return it back to the Command and Control Center. In the paper will be presented the original solution, applicable with minimum of specific modifications (according to the chassis used), to any type of robot requiring both operator-controlled or autoguid control. Thus, a complex project will be realized combining into a unitary Mechatronics, Integronics, Cyber-Mixmechatronics, Artificial Intelligence and Information Technology.*

Keywords: *Cyber-Mixmechatronic System, Artificial Intelligence, Smart Movement Control, Intelligent Measurement Technique, Mechatronic Robots*

1. OVERVIEW - SAFETY AND SURVEILLANCE INTELLIGENCE

Initially, the idea of a robot was tributary to a form morphologically similar to human, with the main purpose of replacing human effort into physical and intellectual work. Maybe inaccurately, this has remained valid until today, but the term itself is extrapolating to any system of some complexity that helps or replaces the human effort.

The humanoid form has been transferred to a separate cluster of robots called generic androids, leaving room for the robot term even in our daily kitchens. In our days we name robot, most of the intelligent mecatronics sistems „working” for us, despite the fact that it can be inaccurate, but the evolution of mechatronics has generated and continues to generate such a wide range of robots that it is difficult to classify and order the term.

Simultaneously with the impressive technological advancement of the last decade, it was natural to have a new type of robot, designed to oversee and ensure the safety of the human being, in fact, an indirect substitute for man and his effort when working in dangerous conditions. The Security and Surveillance Robot (which will be referred to as SSR) is a natural occurrence in the context of replacing direct human intervention where it’s life is endangered. So we return to the same initial hypostasis where SSR, regardless of its structural morphological structure, must be like man. More specifically, a series of specific human actions can be executed.

So we could define as necessary and minimally enough for the proper functioning of an SSR, the following features:

- Real time retrieval and processing (in some form, but coherent) information from the immediate environment
- Controlled movement into the environment
- Existence of decisional control
- Opportunities to interact with the environment by executing specific actions
- Sending or storing data related to the performed activity

An SSR must be able to replace the actual presence of man where, for various reasons (hazardous, toxic, radiation, explosive, violence, etc.) life can be endangered. The robot replaces man, but at the same time he must ensure his decisional presence. Security and surveillance situations are situations that can be

extremely complex, so an Artificial Intelligence able to take decisions is not yet indicated. Thus, except for simplistic surveillance and security situations, human intelligence is still preferred in the context of its decision makers. Such a robot is forwarding all information to the operator, as accurately as possible, ensuring the safely of the human operator placed somewhere far ahead in front of the command and control point. It is thus extremely important how the robot transmits as accurately as possible information and executes the operator's orders as accurately as possible. Thus, not only the accuracy of the transmitted data is important, but also the transfer speed between the robot and the operator becomes at least as important. In turn, the accuracy and speed contributes implicitly to the correctness of the actions and operations executed by the robot.

Figure 1. SSR robot and command console (Talon - produced by Foster Miller*)*

2. STRUCTURAL / FUNCTIONAL ANALYSIS AND ORIGINAL SOLUTIONS FOR THE CONTROL AND MONTORING OF SSRROBOTS

The Robot - a still imperfect copy of living beings - The robot in its various forms, at this moment in the world, is nothing more than an attempt to recreate an artificial being similar to a living one.

Being therefore a more faithful extension of the human operator we can generalize and say that an SSR robot becomes tributary to a functional structure specific to life, acting as a living being capable of surviving and exploring the surrounding environment. For this, a robot must have in his structure some basic parts:

- Body (robot chassis) - a structure capable of protecting its own vital organs
- Feet (wheels, tracks, legs) - to ensure mobility.
- Brain (computational controllers and microsystems) - needed to process received information.
- Sensing organs (sensors) - necessary for the effective reception of environmental information
- Prehensile extremity arms (articulated arm, actuators) - to interact with the environment.
- Communication system (WiFi, GPS, Radio) - to transmit and receive information to operators or other systems.
- Energy (Accumulators) - an individual energy system that will provide the energy needed for all actions.

Far from being exhaustive, this structure will be used for a long time by robot designers and creators, not only in the field of security and surveillance, but also in other areas and applications from home appliances to cosmic space. The following subchapters will respect the above structure.

Chassis and wheels for SSR - In the case of a classic SSR robot, the chassis has to be studied in the considering, first of all its own balance equilibrium (including under stress conditions) and then the best possible driveability. Practically the mobility solution must be chosen first. Movement systems may be used in this regard as follows:

- Moving systems using articulated legs
- Systems using air portance for mobility
- Drive systems using wheels and wheel simulators
- Travel systems using caterpillars or equivalences
- Drive systems using combinations of caterpillars and wheels

The SSR robot must, despite relatively hight mechanical power capabilities, have the lowest power consumption. And the consumption of power must be optimized mainly in the traction system because it is the main consumer.

Taking into account systems using articulated legs as the first moving solution, we will find systems based mostly on a human structure. Although it is a good solution in terms of the possibilities of overpassing the obstacles, we can not neglect the complexity of the mechanical elements that belong to such structures, generating great difficulty for maintaining a firm balance and good stability.

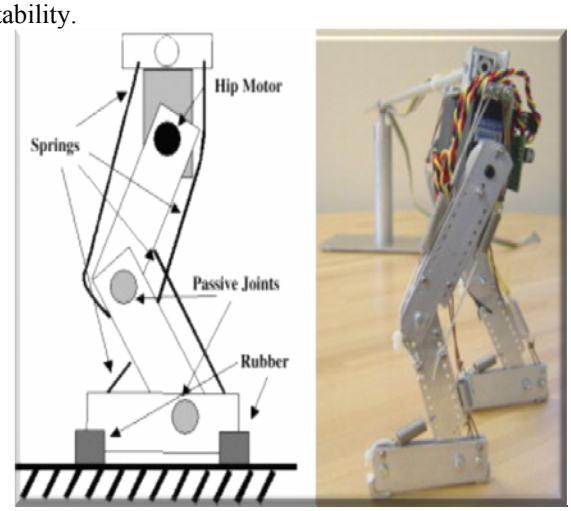

Figure 2. Simple solution of the mecatronic system reproducing the human foot

Such solutions exist only in advanced countries at the stage of research and are still unprofitable solutions both financially, economically and energetically.

Flying systems using wings or propellers are used on airborne robots. They are generically named, drones. Since the paper aims to study and build a terrestrial SSR robot, we will not go into the details of the drones case.

However, it should be noted that this group also includes terrestrial robots using the air cushion principle. Called

and hovercrafts, these displacement systems have the great advantage of being able to move both on land and water, but can not overcome obstacles with dimensions similar to the air cushion thickness.

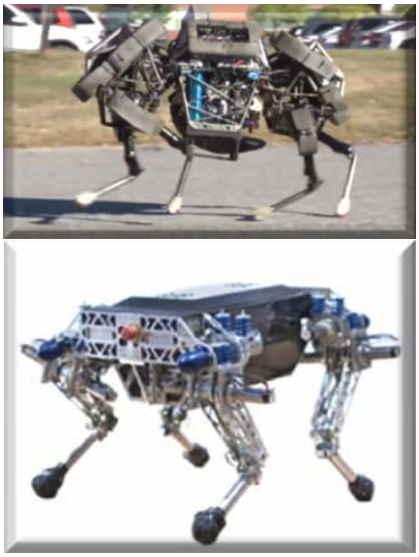

Figure 3. Articulated legged robots in the research phase (from left to right, WildCat - Boston Dynamics and StarIETH - The Institute of Robotics and Intelligent Systems in Zurich)

An air cushioned propulsion system has a form of displacement with histerzis that can not brake suddenly so that very precise placements and movements can not be achieved. For this reason and also because of substantial energy consumption, these systems can not be considered optimal for the SSR robot.Although most mechanism are and have been inspired from existing biological elements, we can see that there are no joints in nature that develop complete rotations, a model that could have been the basis for wheel innovation. And yet this model is present in our everyday life. Biped human walking can be approximated by a circular arc-shaped rotation having the size of the step itself (Figure 4) and s length respectively.

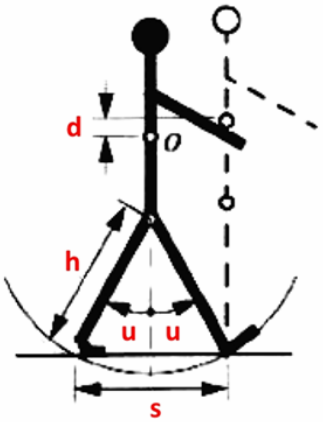

Figure 4. Biped walking describing a circle arch of h-length equal to foot length (Roland Siegwart, Illah Reza Nourbakhsh, Davide Scaramuzza, 2011)

The shape of the arc determined by the angle of a step (2u) approaches a circle - of radius h (foot length).
Generally, as mentioned above, leg movement requires many degrees of freedom and therefore a mechanic solution much more complex than the wheel. On the other hand, another extremely difficult component to compensate for is the displacement of the center of gravity (d) with the idea of maintaining a stable balance of therobot.

Wheels are not only the most used robotic displacement mechanism but also the most commonly used in most human vehicles. This is due to both the extraordinary performance (as shown in Figure 5), but especially to the very simple implementation and reliability.

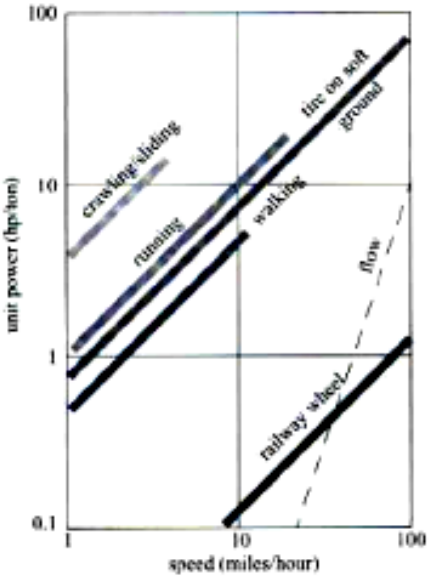

Figure 5. The specific power needed to reach speed for the most commonly used moving systems (Roland Siegwart, Illah Reza Nourbakhsh, Davide Scaramuzza, 2011)

It is more interesting that this ancestral invention, the wheel, can be found today in a multitude of shapes, sizes and types, prepared to overcome the environmental conditions that are unfavorable to it. Thus, we have assumed that a 6-wheel structure is ideal, despite the necessity of synchronicity (they will practically function in the "caterpillar" system, 3 and 3), having independent control on each wheel. The control of each wheel will ensure the viability of the displacement even in the worst critical case (maximum possible / depending on the location of the defective wheels) in which 4 of the 6 wheels have failed. Even in this context, the defective wheels will be decoupled from the loads, with the driving capabilities still remaining on the still functional two remaining wheels. Even if the chassis suffers significant damage, the robot will be able to perform simple operations and / or the return function at the command and control point. The wheel solution is also useful in terms of the possibility of mounting independent suspensions for each wheel with a stroke of about 45-50 degrees in the plane perpendicular to the displacement plane and containing the imaginary axis of

a pair of wheels. This can maintain a very good horizontality of the robot platform and will provide both stability andless positional variations in the virtual helmet of the operator who drives it.

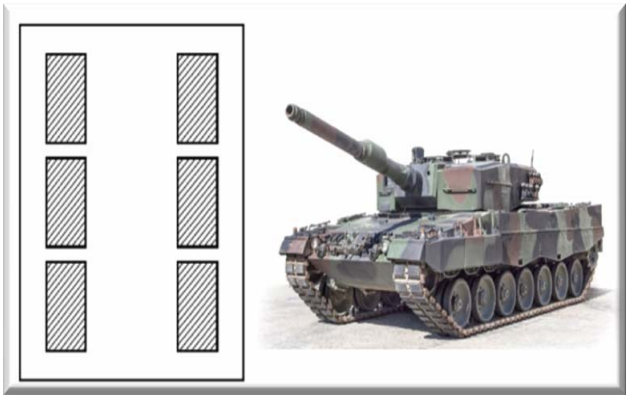

Figure 6. Six-wheeled (catterpilarequivalent) and twin-wheel drive system with independent control of 3-wheel groups

Practically for an SSR robot, we need a structure similar to Figure 6 because we want it to be a solid structure, able to move on rough terrain, capable of reaching relatively high travel speeds (maximum speed of about 10km / hour on smooth ground), but at the same time being able to be operated at low speed, having various turn posibilities. The system must be as simple as possible from mechanical point of view and have the minimum of moving parts to increase its fiability and reliability in missions. At the same time, the chassis system should be as cheap as possible as an action / price ratio, as the possibility of a totally destructive factor during the mission, which would lead to irreparable damage to the robot (explosions, sabotage, etc.) is taken into account. Consequently, a structure, as mentioned above, was approached similarly to Figure 6. Initially, we moved from a DAGU-type structure resized to larger dimensions, including the carrying of heavy loads of about 100kg (it has been taken into account the posibilityof the transport of at least one person from the place of mission to the point of operation and control of the mission in the event of an emergency).

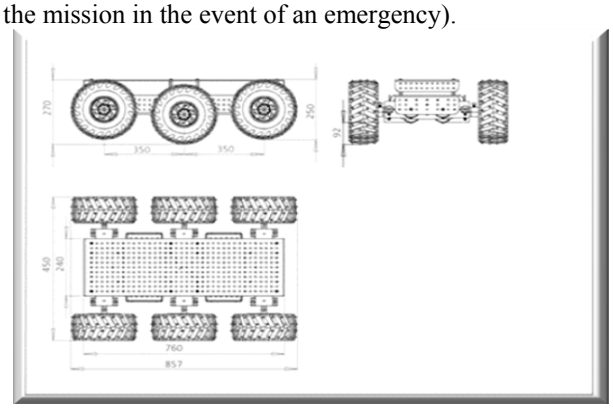

Figure 7. The initial structure with roller bearings and direct drive electric motors located under the chassis in the suspension element

A 6-wheel structure with a diameter of 250 mm, each mounted directly on the drive shaft of the direct drive motor. The motors are brush electric motors and a single control winding. The engines are embedded in articulated cages, which are the chassis suspension itself with arc-shaped elements. The body of the chassis consists of "U" - type elements in the two-dimensional plate (one "U" represents the top of the chassis and the other "U" dimension are the modules for each suspension cell). But this solution it is reduceing the chassis ground clearance to 92 mm, and probably it will be lowered due to the need to install a "shield" surface that is needed to protect the electric motors. The placement of such remote electric motors has led to the conclusion that the solution is still not the most appropriate either because all six engines are exposed to the blows that can occur under the chassis while driving.Also in order to synchronize the electric motors it was necessary to mount on each wheel an incremental speed transducer which would mechanically complicate the wheel.

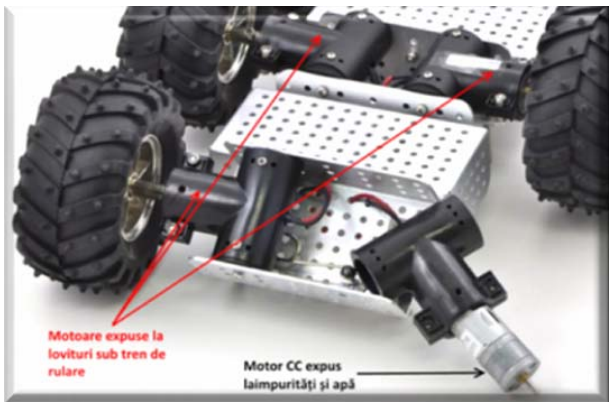

Figure 8.The Dagu Chassis does not protect the engines against impurities, water and strokes under the chasis

Another problem is generated by the fact that this type of electric motors are not dust or watter resistant. To overcome these shortcomings, studies have been have been made having the scope of changing the electric motors that had to develop somewhat more power but especially to be synchronized as accurately as possible and to be better protected. We have come to the conclusion that, despite the difficulty of command and control, new generation BLDC motors (brushless DC motors) meet these requirements. Not only do they contain Hall-like sensors dedicated to precise speed control but take up less space than conventional ones while delivering much better performance and reliability. Ultimately, the most important feature of an engine of this type is the possibility of its execution right inside the wheel. Moreover, such an engine inside a wheel is already in the IP64 protection class, ensuring both dust and water protection. The axle of the wheel is fixed and therefore the connecting wires (both power and control) do not require rotary contacts. And last but not least, this engine is brushless, which also ensures a much greater

reliability in the context of high longevity. Advantages and disadvantages, because that new engine is made with other domanins than robotic applications (automotive) and has not yet been designed with inter-active controllers in remote control and bidirectional software control possibilities. The reason we were forced to interface existing engine wheels with new, original ways that involved staggered research, execution and testing.

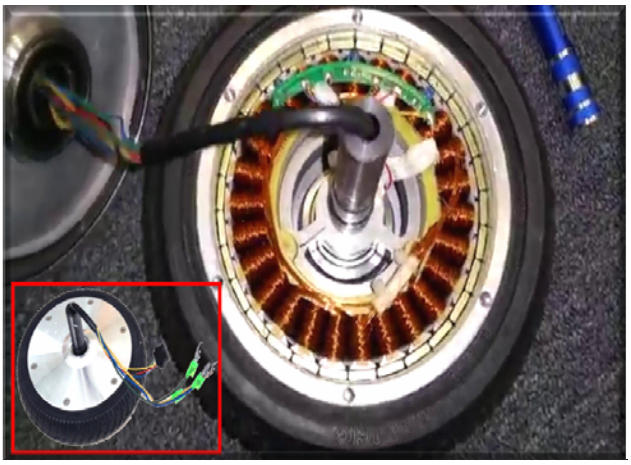

Figure 9. Brushless three-phase DC motor, integrated insidethe wheel, a cutting-edge innovation in mechatronics

Thus, such a structure can be driven by a motion chart of the type shown in Figure 10, with the indication that only movements without effective sliding / skidding between the wheels and the displacement surface have been shown.

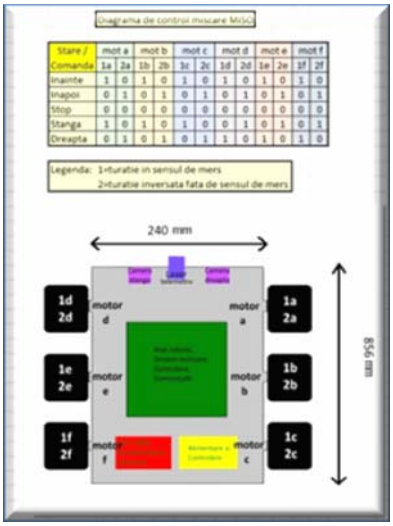

Figure 10. Brushless three-phase DC motor, integrated insidethe wheel, a cutting-edge innovation in mechatronics

In the final tests, the utility of the sliding / skidding will also be evaluated, the controllers having all the possibilities provided in the command and control scheme. The recent emergence of these three-phase BLDC engines has a secondary effect in the internal and international market of dedicated controllers. This is implicitly due to the great powers developed by the engines. Such a wheel-integrated engine of the type used in the SSR robot has about 180 watts of power at a 36 volt supply voltage. There is only one type of controller (manufactured in several versions of power and voltage), which is made to be driven directly by electromechanical controls. Such a controller is the ZTECH E80030-B controller capable of controlling motors with power up to 450W and supply voltages of 36V or 48V.

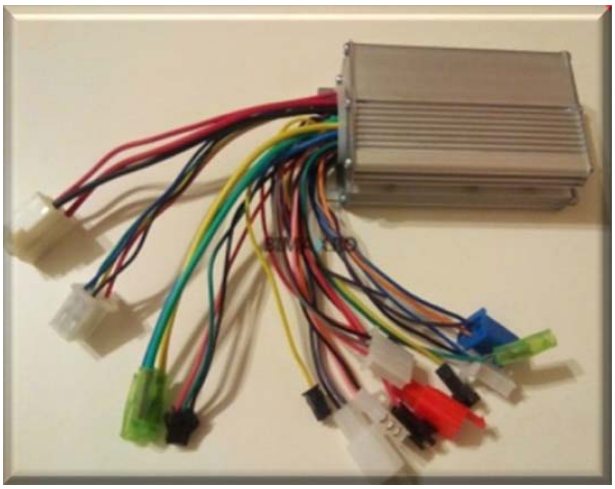

Figure 11. Brushless three-phase DC motor, integrated insidethe wheel, a cutting-edge innovation in mechatronics

We were in the situation where we had a controller compatiblewith the engine, but totally incompatible with the two micro-systems planned to work on the robot (Arduino and Raspberry Pi). Normally, the only solution was to design an interface between the computing microsystem and the ZTECH controller. So a controller that needs an interface to an Arduino microsystem was the solution found in this first phase, the generic intent being to try to control with this triad all the complete robot displacement system. The first problem was actually the acceleration and deceleration of the engine.

Thus, three controller control wires were identified from the 4 wires, respectively those that were useful for operating the motor effectively. Thus, in tests it was found that the black wire and the red wire give a stabilized voltage of 5V (black mass, red plus), and a green voltage requires a voltage trip from 0V to 4.8V, the motor speed being directly proportional to trip voltage (0V - engine off, 4,8V - maximum speed motor). The voltage trip is accompanied by a minimum current of about 20-30 mA. There is a problem because the Arduiono UNO R3 microsystem does not have outputs with digital analogue converter as it would be ideal for such a command. Consequently, an adaptation scheme like the one in Figure 13 was used. We used a PWM output where we actually used a pulse duration modulation function that was then digitally converted analogously to the T1 R1, C1, D1 group in continuous voltage trip. Finally, a 0-5V excursion finally was obtained at the exit.

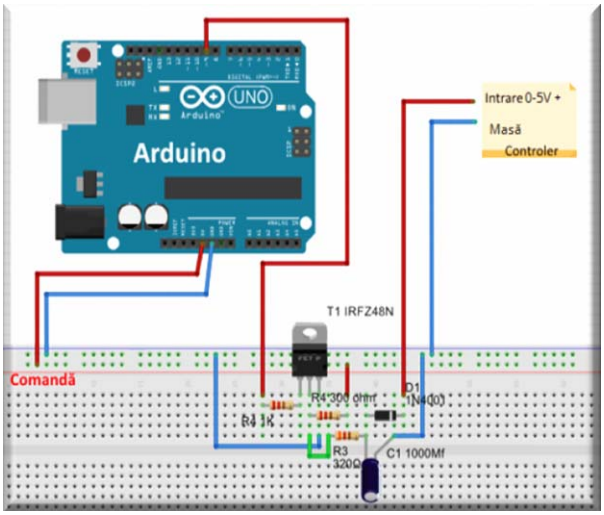

Figure 12. Arduino interfaced with the ZTECH 80030 controller

Two methods were used to control arduino acceleration. The first method consisted in the linear control of the engine's acceleration and deceleration and the second method in the step by step control of both acceleration and deceleration. For the first method we used a potentiometric divider on one of Arduino's analog inputs. A 100Kohm potentiometer was used on Arduino's pin 3 and the output from the PWM 9 pin that attacked the T1 transistor.

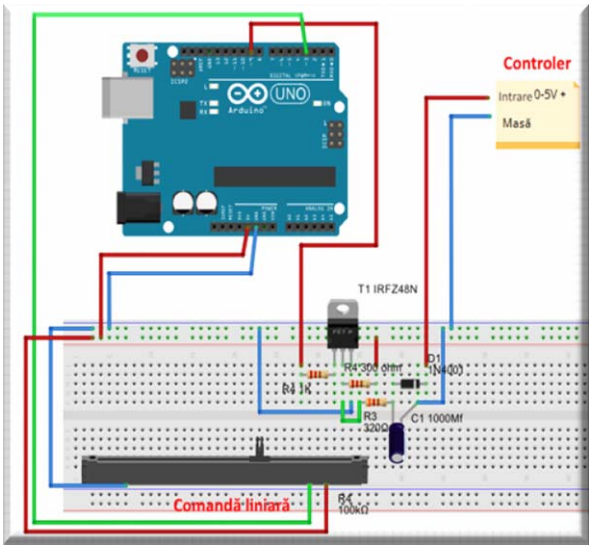

Figure 13. Linear motor speed control with a resistive potentiometric divider

Operating software code using a linear resistive divider:

```
/* Pin Value (0-255) = 255 * (AnalogVolts / 5);
//presupunem intrarea max = 5V, ce se face in
incremente de 255 */
int pwmPin = 9; /* pin iesire de tip PWM*/
int inPin = 3; /* tensiune de comanda conectata la pinul
analog 3, de exemplu un potentiometru 0-5V excursie*/
int val = 0; /* variable to store the read value*/
float volt = 0; /* variable to hold the voltage read*/
/* setPwmFrequency(9, 8);*/
/*TCCR1B = TCCR1B & 0b11111000 | 0x02; seteaza
frecventa mai sus*/
void setup(){
  TCCR1B = TCCR1B & 0b11111000 | 0x02;
pinMode(pwmPin, OUTPUT); /* setam Pinul PWM ca
pin de iesire*/
}
void loop()
{
 /*  citeste valoarea pe pinul de intrare de la
potentiometru*/
/* val = analogRead(inPin);*/
/* manual pentru comenzi val=200 minim si val=100
maxim viteza*/
val = 190;
volt =(5.0 * val) / 1023;
val = 255 * (volt / 5);
analogWrite(pwmPin, val);
}
```

Thus, linear outputs of the output voltage were obtained, which allowed to determine the exact operating range values used by the controller. This was between the minimum threshold of 1.2V (control voltage that starts the engine at its lowest speed) and 3.8V (voltage at which, regardless of its increase to 5V, the engine speed is at maximum limitation by the controller). It is important to know the correct values, especially since the interfacing has succeeded and the next step was to execute a step by step control mode for it.

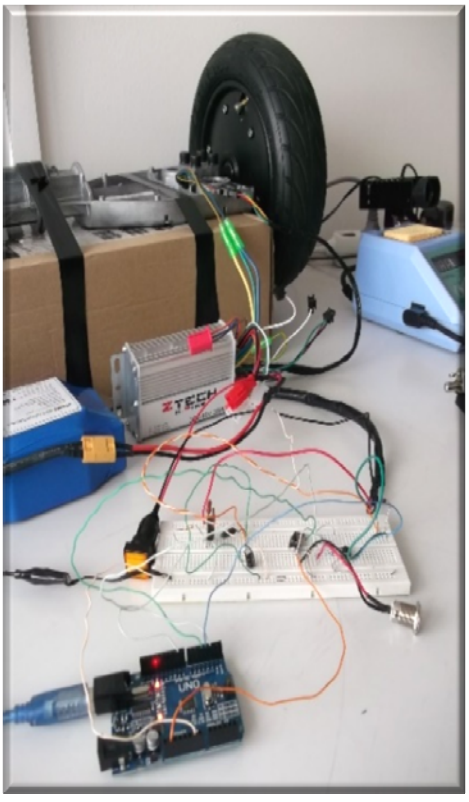

Figure 14. The interface on test bench

The next step was to drive the acceleration and decelerationin discrete steps. This is because we considered it the safest and most consistent way to control the engines. For this purpose the potentiometric control divider has been replaced by two microswitch buttons, one to accelerate and the other to decelerate the engine. A third button has been added, whose role is the "contact key" of the system, enabling it to stop or actually start rotating under whatever conditions the chassis would be (displacement, sationary, mechanical work with the mobile arm, etc.) and independently of other commands coming in other ways. It will also be used later in the software for brake and wheel disabling software control. Of course, these buttons will be replaced in the final model with software impulses, the transformation being now easy and obviously functional.

It is also the reason why we considered the most advantageous for this robot, a discreet speed control, providing a most precise controll.

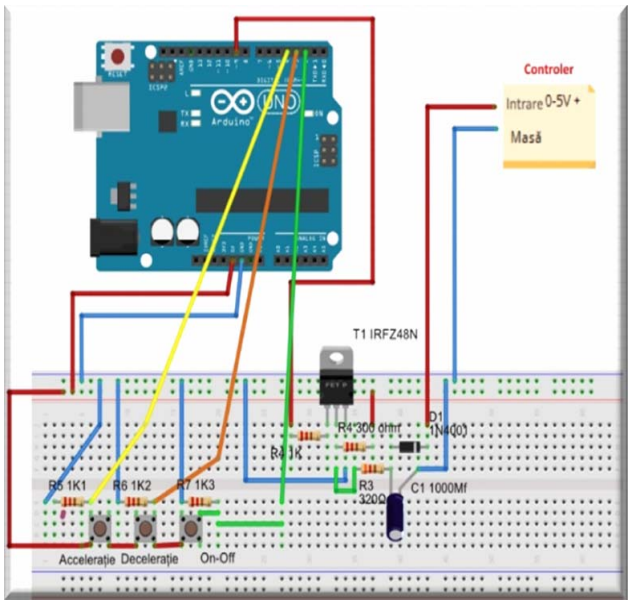

Figure 15. Stage acceleration and deceleration with microswitches (including start-stop function)

Software code for acceleration and deceleration control with on / off button using microswitches:

```
/* Pin Value (0-255) = 255 * (VoltiAnalogig / 5); //presupunem intrarea max = 5V, ce se face in incremente de 255 */
int pwmPin = 9; /* pin iesire de tip PWM pentru comanda turatie*/
int inPin = 3; /* tensiune de comanda conectata la pinul analog 3, de exemplu un potentiometru 0-5V excursie*/
int val = 0; /* variabla de comanda turatie*/
int vali = 190; /* variabla anexa pentru modificare variabilei val*/
int start = 0; /* variabla de comutare ON OFF pe acelasi buton*/
float volt = 0; /* variable to hold the voltage read*/
/* setPwmFrequency(9, 8);*/
/*TCCR1B = TCCR1B & 0b11111000 | 0x02; seteaza frecventa mai sus*/
const int buttonPin = 2; /* intrarea 2 digitala unde este plasat butonul on off*/
const int buttonPinV = 4; /* intrarea 4 digitala unde este plasat butonul crestere viteza*/
const int buttonPinW = 3; /* intrarea 3 digitala unde este plasat butonul descrestere viteza*/
int buttonStare = 0; /* variabila de stare a butonului on off*/
int buttonStareV = 0; /* variabila de stare a butonului crestere viteza*/
int buttonStareW = 0; /* variabila de stare a butonului descrestere viteza*/
void setup(){
  /* schimb ceasul modulatiei de iesire la 3906 Hz */
  TCCR1B = TCCR1B & 0b11111000 | 0x02;
pinMode(pwmPin, OUTPUT); /* setam Pinul PWM ca pin de iesire*/
pinMode(buttonPin, INPUT); /*initializam ca Pin Intrare pentru ON OFF*/
pinMode(buttonPinV, INPUT); /*initializam ca Pin Intrare crestere viteza*/
pinMode(buttonPinW, INPUT); /*initializam ca Pin Intrare descrestere viteza*/
}
void loop()
{
/* val = analogRead(inPin); citeste valoarea pe pinul de intrare de la potentiometru - redirectionat pe pasi*/
/* manual pentru comenzi val=200 minim si val=100 maxim viteza*/
 buttonStare = digitalRead(buttonPin); /*citeste butonul ON OFF*/
 buttonStareV = digitalRead(buttonPinV); /*citeste butonul crestere viteza*/
 buttonStareW = digitalRead(buttonPinW); /*citeste butonul descrestere viteza*/
/* un singur buton de on/off sevential */
if (buttonStare == HIGH){
  delay(400);
            switch (start){
              case 0:
              start = 1;
              break;
              case 1:
              start = 0;
              break;
            }
             }
/* cresterea vitezei in 9 pasi*/
if (buttonStareV == HIGH) {
             vali = vali - 10;
            if (vali <= 100) {
              vali = 190;
            }
             delay(400);
            }
/* descresterea vitezei in 9 pasi*/
if (buttonStareW == HIGH) {
```

```
            vali = vali + 10;
           if (vali >= 190) {
            vali = 190;
           }
            delay(400);
           }
/* comanda efectiva a motorului */
       if (start == 0) {
              // opreste motor:
              val = 255;
              vali = 190;
              analogWrite(pwmPin, val);
             /*   delay(2000); /*doar pentru probe , cu
2000 opreste cam 2-3 secunde cu ceasul marit la 3906
Hz !*/
                          } else {
                               // motor pornit:
                                /*val = 190;  -- necesara ca
initializare pentru potentiometru!*/
                                 volt = (5.0 * vali) / 1023;
                                 val = 255 * (volt / 5);
                                 analogWrite(pwmPin, val);
                               }
}
```

Several attempts of optimum steps have been made (however we may increase/decreassteps as much as desired) and for the time being, we have remained on 9 adjustment steps for both acceleration and deceleration.

As we can see from the software, we used a state change function so from the same button we can cyclically start and stop the engine regardless of its speed.

3. CONCLUSIONS

Although we can not yet conclude in the true sense of the word, given that the equipment is still in testing phase, we can still make some pre-conclusions. Thus we can say that the system itself, the modules used and the basic ideas of the project are correct and functional.

We can say that the equipment can not only be endorsed in the proposed parameters but also meets the requirements of the proposed SSR robot despite the ongoing difficulties due to the use of very new and modern systems that have just emerged in the field of robotics and mechatronics. So it was possible to move on to the next step, namely the development of brake and reversing functions of BLDC motor wheels.

REFERENCES:

[1] Eben Upton and Gareth Halfacree, Raspberry Pi User Guide 2nd Edition, John Wiley & Sons Ltd., The Atrium, Southern Gate, Chichester, West Sussex, PO19 8SQ, United Kingdom, 2014.

[2] Matt Richardson and Shawn Wallace, Getting Started with Raspberry Pi. Published by O'Reilly Media, Inc., 1005 Gravenstein Highway North, Sebastopol, CA 95472, United States of America, 2013.

[3] Cay Horstmann and Rance D. Necaise, Python for Everyone, John Wiley & Sons Ltd., The Atrium, Southern Gate, Chichester, West Sussex, PO19 8SQ, United Kingdom, 2014.

[4] Gheorghe Ion GHEORGHE, Anghel CONSTANTIN, Sergiu DUMITRU, Microingineria Mems & Nems Inteligente, Editura CEFIN, Bucureşti, Romania, 2013

[5] Gheorghe Ion GHEORGHE, Adaptronica Sistemelor Inteligente, Editura AGIR, Bucureşti, Romania, 2014

[6] Y.Daniel Liang, Introduction to Java Programming 8-th edition, Pearson Higher Education. Upper Saddle River, New Jersey, 07458, 2011.

[7] Roland Siegwart, Illah Reza Nourbakhsh, Davide Scaramuzza, Introduction to Autonomous Mobile Robots, Massachusetts Institute of Technology, MIT Press, 2011.

DE GRUYTER OPEN

The Scientific Bulletin of VALAHIA University
MATERIALS and MECHANICS –Vol. 16, No. 14

DOI 10.1515/bsmm-2018-0009

CONCEPT AND ARMONIC ANALYSIS USED FOR PROCESSING DATA SAMPLED BY MECATRONIC DEVICES IN SMART MEASUREMENT PROCESSES

Stanciu Dănuţ Iulian[1,2], Gheorghe GHEORGHE[1,2], Daniela CIOBOATA[2], Aurel ABALARU[2]

[1] Valahia University Targoviste - Doctoral School of Mechanical Engineering, Targoviste, Romania
[2] National Institute for Research Development in Mechatronics and Measurement Technique, Bucharest
6-8 Pantelimon Road, District 2, Bucharest, Romania

E-mail: danutstanciu@yahoo.com

Abstract. *Harmonic analysis is a mathematical method that performs the determination (approximation) of continuous functions by the sum of ideal sinusoids. By selecting these sinusoids in a judicious way, in defining the methods of smart measurement of a part, it is possible to separate the geometrical elements of a part into geometric elements of the shape (circularity, eccentricity, etc.) of the geometric elements corresponding to the state surfaces. This article, using the research carried out under the doctoral thesis "COMPLEX STUDIES, RESEARCH AND EXPERIMENTATION OF PRECISION MECHANICAL GEARING TRANSMISSIONS USING HIGH PRECISION HARMONICS METHODS ", aims to perform an original work and thus to present and analyze the main methods of processing the data gathered in the process measurement of the parts made and used in mechatronic equipment by resorting to harmonic analysis.*

Keywords: *Harmonic, Fourier analysis, Shape deviations, Roughness, Real-time analysis*

1. INTRODUCTION

Harmonic analysis, done usually with the help of the Fourier Transform, is a mathematical tool that shows that any continuous function can be represented by a sum of sinusoidal functions.
Fourier transform is defined by:

$$F(s) \equiv \int_{-\infty}^{\infty} f(x) e^{-2\pi i s x} d(x)$$

also known as "Direct Fourier Transform" and

$$f(x) \equiv \int_{-\infty}^{\infty} F(s) e^{2\pi i s x} d(s),$$

also known as "Inverse Fourier Transform".

In reality, when the measurement process takes place, we are dealing with signals that are sampled discreetly, usually at constant intervals, and of finite or periodic duration. For such data, only a finite number of sinusoids is required, and Discrete Fourier Transform is consequently required (DFT - Discreet Fourier Transformation).

For discrete data sets (such are those obtained in the measurement process), the discrete Fourier transform of N data points sampled uniformly x_j (where j = 0,...,N-1) is given by the following formula:

$$x_k = \sum_{j=0}^{N-1} x_j e^{-2\pi i j K / N}$$

and the inverse Fourier transform is given by the following formula:

$$x_j = \frac{1}{N} \sum_{k=0}^{N-1} x_k e^{2\pi i j k / N}$$

The DFT result of an input time series in N points is a frequency spectrum in N points, whose frequency is k, with k ranging from 0 to (N/2-1), from component 0, known as the continuous component, to that of the highest frequency whose value is N / 2. Each value of k represents the number of sinusoids present in each series. If the amplitude and the phase of each component are denoted by A_k (amplitude) and Φ_k, then each of the component sinusoids can be described by the equation below:

$$x_k = A_k e^{i\Phi_k}$$

For sets of data sampled under the measurement process, the result of the Direct Fourier Transform, the real value of the spectrum is represented by the even components, and the complex value is given by the odd components of the transform.
Direct Fourier Transform is a complex mathematical algorithm that requires a large amount of computation (N2 operations). To increase the execution speed James W. Cooley and John W. Tukey ("An algorithm for the machine calculation of complex Fourier series," Math. Comput. 19, 297–301-1965) created an algorithm, adapted to the computer, which increases the speed of

data processing so that only a number of operations equal to N log2(N) operations is needed; this algorithm is also known as FFT - Fast Fourier Transformation, the only requirement of the algorithm is that the number of sampled points is a power of 2 (2,4,8,...1024,...)
The mode of operation of the FFT algorithm is given in the following figures (Fig. 1, Fig. 2):

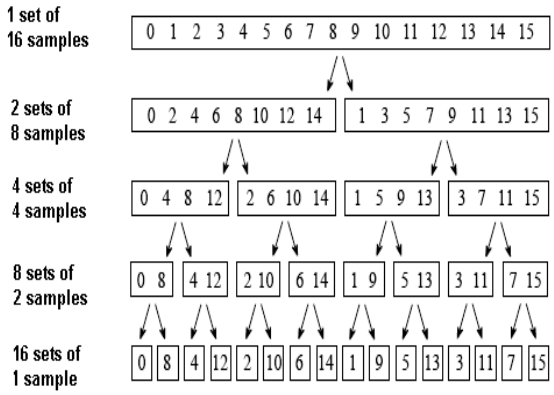

Figure 1. The manner of decomposing sets of points under Fast Fourier Transform

A dataset of N samples is decomposed into N datasets each of one sample. Each phase uses a cross-decomposition that separates the even components from the odd ones.

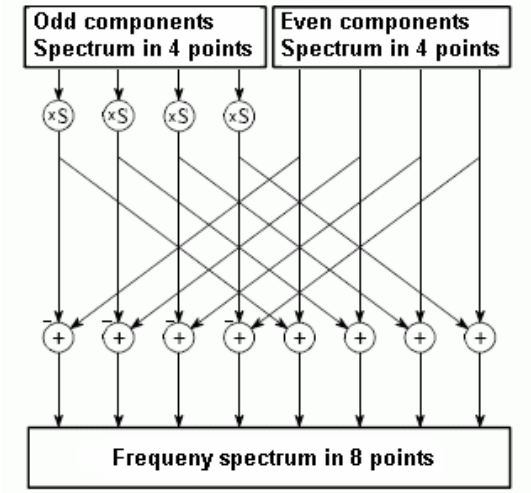

Figure 2. An example of the manner of obtaining the spectrum for an 8-point sample

The methods shown in Figures 1 and 2 ease the making of high performance software by implementing algorithms that work in parallel and that can further exploit the performance of modern processors by simultaneously using all the kernels of the processor, or by making it possible to use existing processors in graphics cards (graphics cards can room up to 256 processors that work in parallel).
In the case of data sets processed under the measurement process, the time variable is replaced by a variation of an angle or of a displacement (for example, for revolution parts the time unit is replaced by a rotation). For ease of presentation, the term "frequency" is used throughout the paper, but it is defined as frequency over a movement or rotation.
In essence, data processing used for dimensional measurements consists of acquiring data at equal distances and applying Fourier transform to them. In order to be able to apply Fast Fourier Transform (FFT), the number of acquisition points need to be powers of 2 (2, 4, 8, 16, 1024, 4096, etc.). Following the application of the Fourier transform, the spectrum of frequencies is obtained.
An example of the manner in which a random waveform can be composed and decomposed is given in Fig. 3, where we can see that we can obtain the basic curve as the sum of the sinusoid components (the frequency, the phase and the amplitude of the sinusoids are obtained by means of the Fourier Transform)

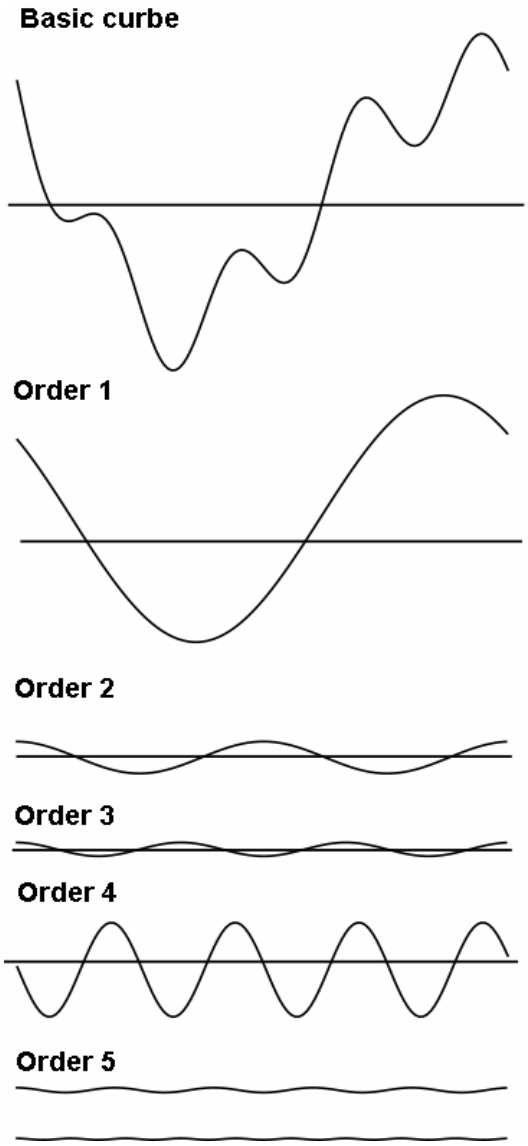

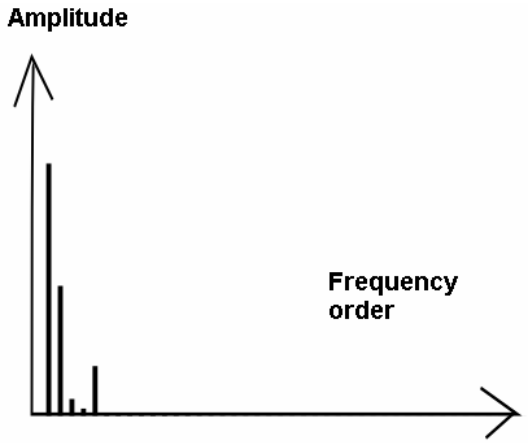

Figure 3. An example of composing and decomposing a real curve using Fourier transform

For the measurement of a revolution part placed eccentrically (Fig. 4), with defects of shape and surface, we have a spectrum shown in Fig. 5

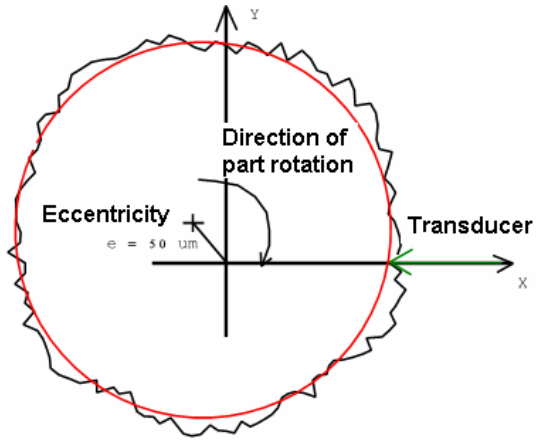

Figure 4. The polar chart of measuring a revolution part

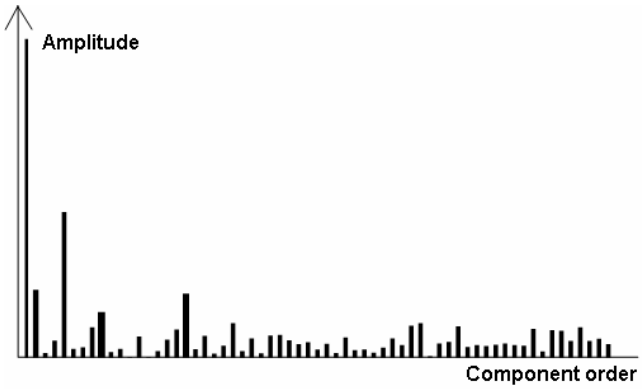

Figure 5. Frequency spectrum obtained by Rapid Fourier Transform

In the case of a revolution part, the frequencies are actually the number of undulations present at the surface of the part; thus the component of order 1 represents the eccentricity, the component of order 2 represents the ovality, and so on. In the case of the part shown in Fig. 4, the linear presentation of the data sampled by the transducer in the figure is the following: (Fig.6)

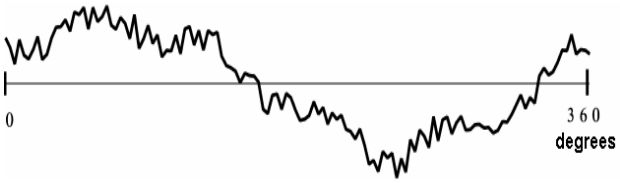

Figure 6. Linear representation of the values sampled from the the revolution part

In order to obtain the eccentricity of the part out of the frequency spectrum, we eliminate all components aside from the component of order 1 and then we apply the inverse Fourier Transform. The results of this processing are shown in Fig. 7, and the found value of eccentricity is of 49.964 µm and is very close to the theoretical one, of 50 µm.

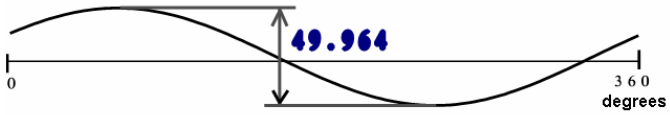

Figure 7. The eccentricity of the part obtained by means of the harmonic processing method

In order to obtain the shape components of the part (the eccentricity is assumed to be a result of the part being assembled, thus it is a mutual position deviation), we eliminate the components of order 0 (continuous value or mean value), those of order 1 (eccentricity) and those of orders with value greater than 18 (this limit value is determined experimentally and is greatly influenced by the type of part and by the processing mode). By applying the inverse Fourier transform, a plot of the shape deviations of the part is obtained (Fig.8). On this dataset, the maximum and minimum and the total maximum deviation are obtained.

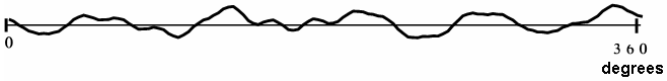

Figure 8. The shape deviation of the part presented in Figure 4

In order to obtain the higher order information, which represents the surface roughness, all components of the order of less than or equal to 18 are eliminated and then the Inverse Fourier transform is applied; we will obtain the surface state diagram on which (for example) the roughness-specific parameters can be identified. (Fig. 9)

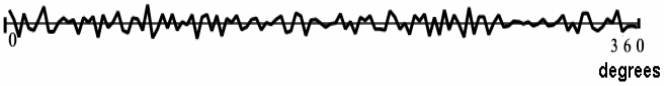

Figure 9. The roughness diagram obtained by means of the harmonic processing method

At INCDMTM – Bucharest was designed and built a device for measuring shape deviations of revolution parts in whose making were applied also processing methods using the Fourier transform presented above.

Figure 10. Device for measuring shape deviations of circular parts also using data processing methods based on Fourier transform

This device uses a gasostatic bearing on which a universal bearing is mounted, which in turn grabs the part. Since the part can not be perfectly be grabbed and centred with the centre of rotation, the Fourier transform is used to eliminate the clamping eccentricity, after which the sampled data is processed by usual methods (smallest squares, maximum, minimum, deviation).

Applications of Fourier Transform in the Analysis of Toothed Wheels

For gear analysis, using the testing based on both sides engagement and using Fourier analysis, a series of toothed wheel parameters can be obtained quickly. The scheme of this device is shown in Figure 11.

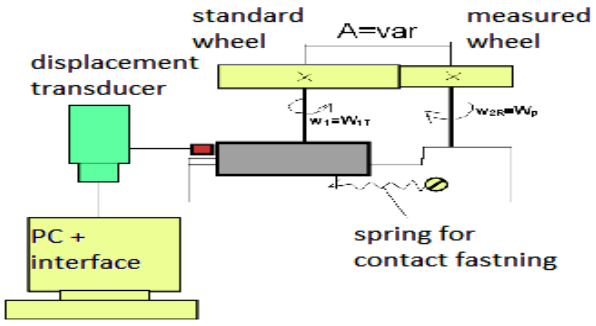

Figure 11. The scheme of toothed wheel testing based on both sides engagement

After data sampling, a data diagram of the following form is obtained (fig. 12):

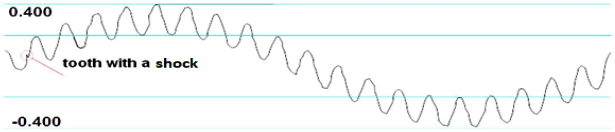

Figure 12. The diagram of data sampled from forced engagement of toothed wheels

By extracting the component of order 1, we obtain the variation of the distance between the axes (fig. 13):

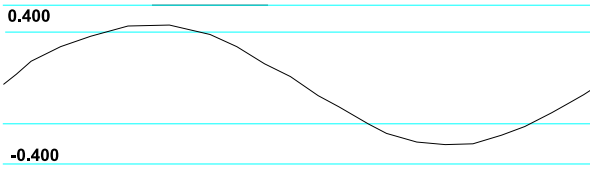

Figure 13. The diagram of the variation of the distance between the axes

By extracting the components from the range of undulations 2 to 50, the tooth engagement diagram is obtained, unaltered by the variation of the distance between the axes (Figure 14).

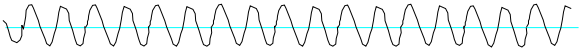

Figure 14. The the tooth engagement diagram is obtained, unaltered by the variation of the distance between the axes

On this diagram, further processing can be performed to extract deviations such as step deviation, teeth profile deviations and so on.

CONCLUSIONS

The method of processing by applying the Fourier transform to complex, digital computerized measurements is a fast, reliable and accurate method that allows for increased productivity of measurement and control processes, increases measurement accuracy without an excessive increase in mechanical execution precision, and helps to increase the level of automation of measurement processes.

REFERENCES

[1] Introduction to the Fourier transform - Web page - http://www.thefouriertransform.com/#introduction.

[2] Fourier Transforms - Web page - http://www.cv.nrao.edu/course/astr534/FourierTransforms.html.

[3] Fourier Transform - Web page - https://en.wikipedia.org/wiki/Fourier_transform

[4] Minciu Constantin – Precizia si controlul angrenajelor, Editura tehnică, 1984, Romania.

[5] Botez E., Minciu C. Mecanismul fictiv şi precizia dinamică a lanţului cinematic de rulare, Editura tehnică, 1984, Romania.

[6] Duca Z., Teoria sculelor aşchietoare, Editura tehnică, 1984, Romania

[7] Sauer ş.a., Angrenaje, Volumes 1 and 2, Editura tehnică, 1984, Romania.

DE GRUYTER OPEN

The Scientific Bulletin of VALAHIA University
MATERIALS and MECHANICS –Vol. 16, No. 14

DOI 10.1515/bsmm-2018-0010

DISPLACEMENT STATES FOR ISOTROPIC PLATES

Carmen POPA[1], Violeta ANGHELINA[1], Octavian MUNTEANU[2]

[1] Valahia University Targoviste, Romania, [2] KPD Construction Software, Halen, Belgium

E-mail: carmenpopa2001@yahoo.com

Abstract. *In this paper the deformation state of a circular and isotropic plate is analyzed, using as methods of comparison the analytical, the finite element and the experimental element methods. In the finite element method, the plate is analyzed by several programmes, as well as assembled with the respective container.*

Keywords: *Plate, Analitical method, Finite element method, Experimental method*

1. INTRODUCTION

The circular plates are met in diverse engineering constructions. They are used like circular plates for the foundations of some machines, at the coupling of the pipes and others.

The researches for establish the states of deformations and stresses can be grouped in: mathematical methods of calculation [1-3]; numerical methods [4-6]; experimental methods [7 -11].

2. ANALITICAL METHOD

We consider a recipient with a fixed circular plate. The plate has the following dimensions: diameter ϕ = 650 mm and thickness h = 10 mm, like in Figure 1.

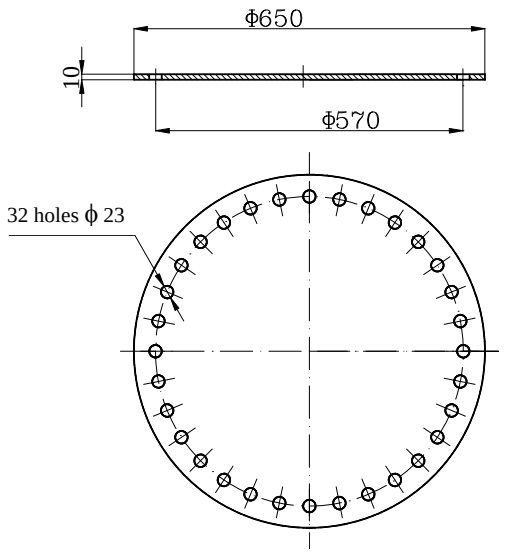

Figure 1. The geometrical characteristics of the plate

The ensemble is loaded with a uniform distributed charge p = 0,2 MPa. Because the load is axial-symmetrically, the median plane of the plate will be deformed axial- symmetrically, too.

The bending parameters of plate depend of its thickness, as against the others dimensions of the plate.
If the displacement "w" of a plate is short, as against its thickness, we can allow these hypotheses:
- the median surface of the plate doesn't permit extensions. This plane remains a neutral plane in the due time of the bending of the plane;
- the points of the plate, which are on a normal straight line, remain on a normal straight line at the median surface of the deformed plate;
- the normal stresses after the normal direction of the median surface of the plate can be neglected;
From the differential equation for the axial-symmetrical bending of the circular plates, which are solicited transversal [1], it results:

$$\frac{d^3w}{dr^3}+\frac{1}{r}\frac{d^2w}{dr^2}-\frac{1}{r^2}\frac{dw}{dr}=\frac{T}{D} \tag{1}$$

We obtain the displacements:

$$w=\frac{p\cdot r^4}{64D}-C_1\cdot\frac{r^2}{4}-C_2\cdot \ln r+C_3 \tag{2}$$

In these relations:
w represents the deflection; T – the shearing force; φ - the slope angle; r - the current radius; C_1, C_2, C_3 - the integrating constants; D – the bending rigidity of the plate, which has the expression:

$$D=\frac{E\cdot h^3}{12\cdot\left(1-\nu^2\right)}, \tag{3}$$

where: E is the modulus of longitudinal elasticity of the plate material; ν - the coefficient of the transversal contraction (the Young ′s coefficient).

The maximal deflection is in the centre of the plate, at $r = 0$.

$$w_{max} = \frac{p \cdot R^4}{64 \cdot D} \quad (4)$$

In the studied case: w =1,102 mm.

3. FINITE ELEMENTS METHOD

In Figure 2 is analyzed the plate which has the geometrical characteristics from Figure 1, solicited at the same pressure, using COSMOSWORKS program. We can observe that the resulted displacement value declines.

In Table 1 are presented the values of the resulted displacements for the plane plate and in the Figure 2 the graphic which is obtained in COSMOSWORKS program.

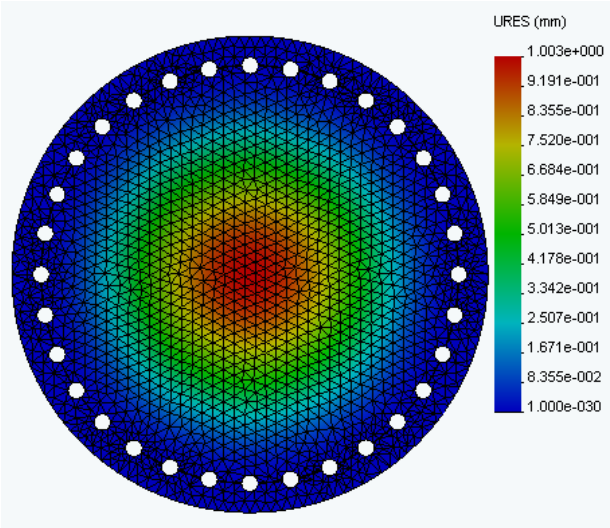

Figure 2. Resulted displacements for the plane plate, obtained in COSMOSWORKS program

Table 1. Resulted displacements in the plate, following a plane passing through the centers of two diametrically opposed holes

R[mm]	0	124	175	225	285
w[mm]	1,003	0,641	0,328	0,115	0

Using the ANSYS program, for the plate of the same size, subjected to the same pressure of 0,2 MPa, the vertical displacements from Figure 4 are obtained. The board is meshed into *solid* elements. A quarter of the plate is analyzed, requiring symmetry conditions and binding to the rest of the plate. It can be seen that the values of the vertical displacements with the two programs are also very close.

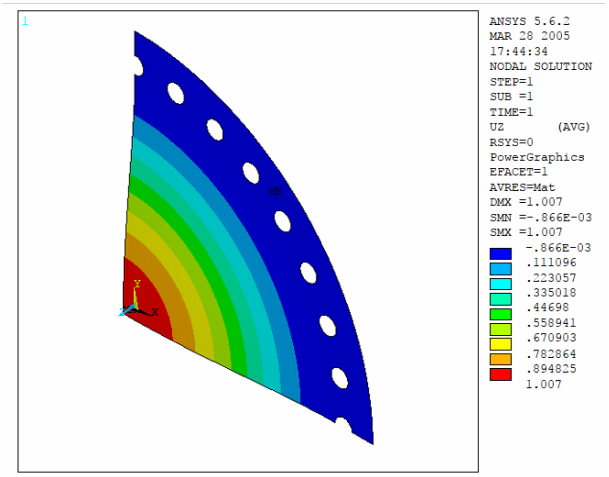

Figure 3. Vertical displacements for the plane plate, obtained in *ANSYS* program

Performing finite element analysis when assembling with the container, we can conclusion that the results obtained for both situations using Cosmos Finite Element Method are appropriated, so errors given of the methods are small.

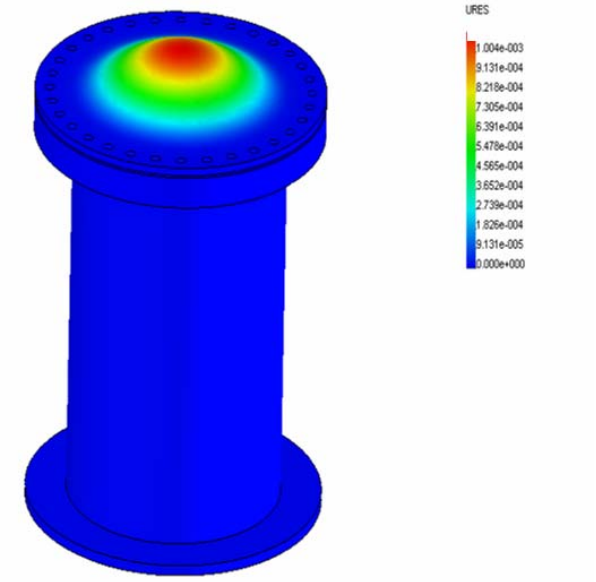

Figure 4. Resulted displacements for the plane plate, obtained in COSMOSWORKS program, when assembling with the container

4. EXPERIMENTAL METHOD

For the assembly of Figure 5, the experimental situation was used, namely the placement of four comparators at 100, 125, 175 and 225 mm distances from the center of the plate (Figure 6).

Figure 5. Experimental stall

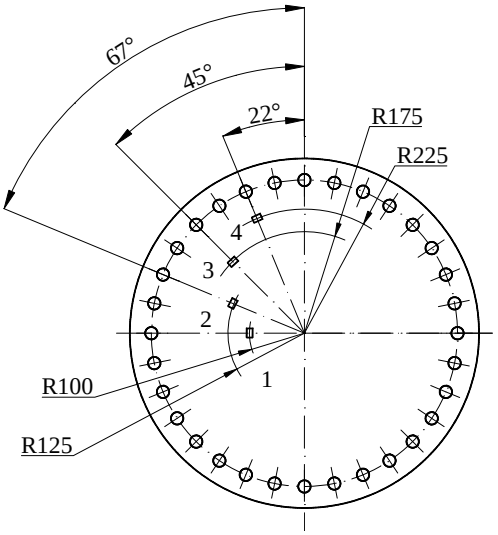

Figure 6. Location of the comparators

The values of the displacements indicated by the comparators were read, both when the pressure rise and the lowering. The processing of the experimental data is carried out using the Mathematica program, accepting a linear variation dependent on the test pressure, as shown in Figure 7.

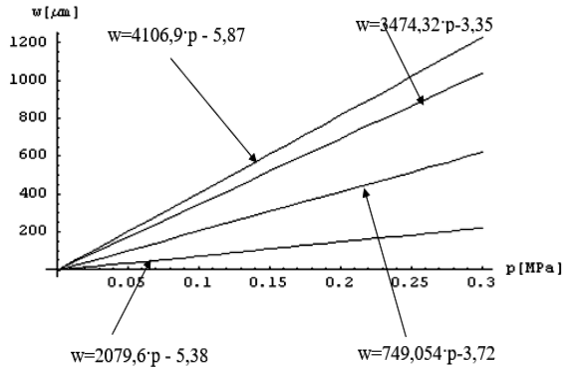

Figure 7. Straights that characterize the dependence of measured displacements with four comparators positioned at different distances from the center of the plate

The following analysis refers to the comparison of the results obtained theoretically - by the analytical method (MA) or the finite element method (MEF) - with the experimental ones (ME). In this regard, the values of the deformations produced at various points of the planar circular plates are taken into account.

The variation of the smooth plate displacements with the embossed contour, determined using the three methods (MA, MEF and ME), for the current plate radius and the pressure of 0,2 MPa, according to the data in Table 2 (using the displacement values calculated using approximation lines that do not go through the origin of the reference system axes; the differences between the displacements values are insignificant) are shown in Figure 8.

Table 2. The displacements values $[\mu m]$, analytic calculated (MA), by Finite Element Method (MEF), and experimentally determined (ME)

p [MPa]	r [mm]	$w\,[\mu m]$		
		MA	MEF	ME
0,2	0	1088	1003	-
	125	710	640	692
	175	416	325	411
	225	154	115	146

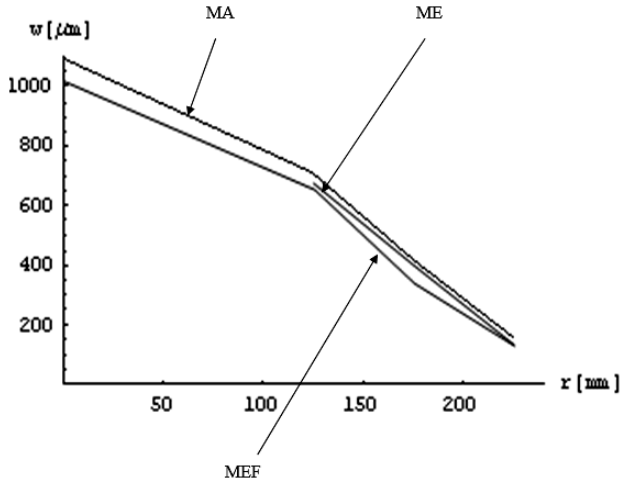

Figure 8. The variation of the plate displacements values, established using the three methods (MA, MEF, and ME)

5. CONCLUSIONS

The displacements values, analytical calculated(MA), by Finite Element Method (MEF) and experimentally established (ME), have close values. Considering the experimental displacement as the reference value, the deviations of their values can be determined:

$$\Delta_1 = \frac{w_{ME} - w_{MA}}{w_{ME}}; \qquad (5)$$

$$\Delta_2 = \frac{w_{ME} - w_{MEF}}{w_{ME}}; \quad (6)$$

The deviations of the displacements values are shown in Table 3:

Table 3. Evaluation deviation of displacements values

p [MPa]	r [mm]	Δ_1 [%]	Δ_2 [%]
0,2	0	-	-
		-	-
	125	- 2,6	+ 7,5
		- 2,2	+ 7,9
	175	- 1,2	+ 20,9
		0,0	+ 21,9
	225	- 5,5	+ 21,2
		- 2,7	+ 23,3

REFERENCES

Books:

[1] Timoshenko S, Woinowsky-Krieger S, *Theory of plates and shells*, McGraw Hill Education, 2010

Journals:

[1] Vanam B, Rajyalakshmi M, Inala R, *Static analysis of an isotropic rectangular plate using finite element analysis (FEA)*, Journal of Mechanical Engineering Research, Vol. 4, 2012, pp. 148-162.

[2] Mekalke G, Kavade M, Deshpande S, Analysis *of a plate with a circular hole by FEM*, Journal of Mechanical and Civil Engineering, 2012, pp.25-30.

[3] Wang Y, Rongqiao X, Haojiang D, Threedimensional solution of axisymmetric bending of functionally graded circular plates, Elsevier Composite Structures 92, 2010, pp.1683–1693.

[4] Sukla B, *The FEM analysis on circular stiffened plates using ANSYS*, Bachelor of Technology diss., National Institute of Technology, Rourkela, 2009.

[5] Meghare T, Jadhav P, *A simple higher order theory for bending analysis of steel beams*, International Journal of Civil Engineering, volume 2, Issue 4, 2015, pp-31-38.

[6] Manzoor S, Vinay G, *A Study on Composite Steel Tubes*, International Journal of Civil Engineering, EFES, 2015.

[7] Gujar P, Ladhane K, *Bending Analysis of Simply Supported and Clamped Circular Plate*, International Journal of Civil Engineering, Volume 2, Issue 5, pp. 69-75, 2015.

[8] Popa Carmen, *Solicitation states at circular plates*, Modellingand optimization in the machines building field, Bacau, 2004, vol I, MOCM 10, pp. 263-268.

[9] Popa Carmen, *Displacement analyze for circular plates*, Al III-lea Simpozion International "Mecatronica, Microtehnologii si Materiale Noi", Targoviste, 2006.

[10] Cursaru D, Neagu M and Bogatu L 2013 Investigations on the Oxidation Stability of Biodiesel Synthesized from Different VegeTable Oils, Revista de chimie 64(4) pp 438-441.